WARWICK

Modelling the Magnetic Properties of Thin Metallic

Films using Monte-Carlo Simulation

by

Yongyut Laosiritaworn

Thesis

Submitted to the University of Warwick

for the degree of

Doctor of Philosophy

Department of Physics

July 2002

Contents

List of Figures

List of Tables

Acknowledgments

I would like to sincerely thank Prof. Julie Staunton for her excellent supervision throughout the period of my study. Without her, this thesis cannot be accomplished. I would also like to thank DPST who have been supported me my study since I began a university-student life. Next, my thanks go to friends. Some of the very important friends are Razee and Vijay. Finally, I would like to thank my father, my brother, my sisters and Wimalin who always stay nearby and encourage me whenever I need.

Declarations

This thesis is submitted to the University of Warwick as my application towards the degree of Doctor of Philosophy. All details of the research carried out in the Department of Physics between October 1998 and July 2002. The content of this thesis is my own work under the supervision of Prof. J.B. Staunton at the University of Warwick. No part of the thesis has been submitted for a degree anywhere.

Abstract

In this thesis, Monte Carlo studies of the static critical behaviour of metallic magnetic thin-films are presented. The studies make use of a finite size scaling method designed for anisotropic shaped structures. This finite size scaling method is based on an assumption that a single correlation length is required to describe a thin-film close to its critical temperature and has lead to the derivation of formulae from which thin-film critical temperatures and exponents can be extracted. Monte Carlo simulations for Ising thin-films are carried out in order to verify the validity of the assumption and hence the formulae. Various algorithms and seed numbers for a random number generator are tested to minimise statistical errors. These studies also show the evolution from $2D$ to $3D$-like behaviours as the films' thicknesses are increased. Critical temperatures and exponents are investigated for simple cubic (SC), body centred cubic (BCC) and face centred cubic (FCC) thin-films. Our Ising $2D$ and $3D$ results are also shown to give good agreement with previous Monte Carlo work.

We then move on to study in a more realistic model of a magnetic thin-film in which the 'exchange parameters' and anisotropic constants are extracted from 'first principles' electronic structure calculations, and used in Monte Carlo simulations of a classical Heisenberg model. We model thin-films of Fe grown on a W(001) substrate which have been subjected to extensive experimental investigation. In line with the

Mermin-Wagner theorem, we find a slow convergence for the magnetisation with the system size L in $2D$ which is consistent with expected absence of finite magnetisation in the finite temperatures in the thermodynamic limit. From the thin-film results in finite size systems, the magnetisation in the surface layers is weaker than those in the inner layers and a similar trend is found for the susceptibility. Slow magnetisation convergence with size is also observed for all thin-films (thickness varying from 2 to 8 layers). Because of this and the sensitivity to statistical errors, only critical temperatures and 'susceptibility critical exponents' can be extracted from the susceptibility functions. The results again show a crossover from $2D$ towards $3D$-like behaviour. The critical temperatures are lower than those calculated from mean-field approximations and are in good agreement with experimental values where available. The differences in results between isotropic and anisotropic systems in which the anisotropic constants are very small in comparison to 'exchange interactions' are not significant.

Chapter 1

Introduction

Monte Carlo simulation methods are used nowadays to solve a wide range of statistical problems (e.g. finance and risk forecasting [1, 2], traffic flow [3], nuclear reactor design [4], VLSI design [5], etc.). The common factor in these Monte Carlo methods is the use of series of random numbers to select states with the relevant probability density functions for the problems.

Although they are numerical methods and cannot give exact results as analytic methods can, they have been shown to give very accurate results in comparison to exact treatments e.g. the $2D$ Ising model. They have proved themselves to be of practical use in applications to statistical physics problems. They can be used to study some interesting problems where exact solutions are unknown; for example, the nature of magnetic phase transitions in $3D$ and in reduced dimensions (thin-films) which continue to attract much interest from both experimentalists and theorists and which are the subject of this thesis.

The interest in the magnetic phase transitions and their dependence on dimensionality has been boosted by the recognition of the technological and fundamental importance of magnetic metallic thin-films and multi-layers [6, 7]. At present it

seems that metallic magnetism is only quantitatively well explained for bulk and $2D$ systems at zero temperature. Magnetic behaviour at finite temperatures (e.g. above T_C) especially for layered systems is still not fully understood. Even with simulation model studies by Monte Carlo methods for example, there is an incomplete picture for magnetic thin-films, in particular how the magnetic properties change from being $2D$-like in the ultra-thin film limit to $3D$-like when the films are thick. Then, this leads to the purpose of this thesis. We study the magnetic properties of metallic thin-films to investigate their behaviour as a function of film thickness by means of Monte Carlo simulations especially in the critical region (near the phase transition) where less understanding is available. We start with a brief introduction of the implementation of Monte Carlo methods to thermal equilibrium statistical physics problems in chapter 2. This includes how to relate the fluctuation of the magnetisation to the susceptibility, how to calculate the average of observables using a small number of terms but with reasonable accuracy using importance sampling, how to estimate the equilibration point, how to calculate the statistical error, how to calculate the correlation time which affects the statistical error of the calculated observable, how to extend the Monte Carlo results to temperatures nearby the simulated temperature to save computer time (histogram method) and how to analyse Monte Carlo results to extract critical temperatures and exponents using finite size scaling and fourth order cumulant methods. The chapter also includes the introduction of a simple magnetic model, the Ising model, which is used for the simulations of thin-films described in chapter 3 as a preliminary study for the classical Heisenberg model investigation in chapter 5.

For thin-film simulations, we develop a method to analyse data based on a finite size method for anisotropic shaped systems. Ising thin-film simulations (chapter 3) are firstly undertaken because of the relative ease in applying the algorithms including the one computer memory bit requirement to store one spin. For the thin-film structures (simple cubic SC, body centred cubic BCC, and face centred cubic

FCC), we also reduce computation time by using a mapping function to store spins from three dimensional space into one dimensional array. We simulate the thin-film systems by using the methods described in chapter 2. Monte Carlo algorithms (e.g. Metropolis and Wolff algorithms) are tested for $2D$ square lattices to find an efficient algorithm for the study of the Ising model. Next, by using the fourth order cumulant and finite size scaling analysis described in chapter 2, the critical temperatures and exponents for the thin-films including and compared with those from $2D$ and bulk $3D$ systems are reported. Demonstration of magnetisation and susceptibility scaling functions are shown to support our results.

Traditionally, critical temperatures T_C extracted from Monte Carlo simulations are measured in a unit of an 'exchange parameter'. The usual process is done by setting all the first nearest neighbour interactions as well as the Boltzmann constant to 1 and other nearest neighbour interactions to be proportional to that of the first nearest neighbour. This may be convenient when we consider simple magnetic models. However, for quantitative modelling of real magnetic materials, we need to allow the exchange interactions to become more flexible as sometimes the exchange interaction is not only a function of distance. For example, in real thin-film systems which we aim to model in this thesis, the exchange interaction is also a function of layer indices. Moreover, for the purpose of comparison to some experiments, the exchange interaction should have a proper energy scale unit.

Thus, in chapter 4, we give some introduction to the calculation of the exchange parameters from a 'first principles' quantum mechanical electronic structure calculation method. We start with a brief review of the electron density functional method and its extension to finite temperatures with the Disordered Local Moment (DLM) picture. From this, it is possible to extract the critical temperatures from a mean-field approximation. Usually, however, the mean-field critical temperatures are too high in comparison to experimental values and other more sophisticated methods

are needed to improve this. Here we use Monte Carlo methods. The 'exchange parameters' for a classical Heisenberg hamiltonian for Monte Carlo simulations are extracted from the 'first principles' method. Moreover, because of the proper energy scale of the 'exchange parameter', the simulation produces critical temperatures in real units (K). At the end of the chapter, we also mention a way to estimate the magnetic anisotropic constants from the 'first principles' for the purpose of getting more realistic models of layered magnetic materials.

In chapter 5, with the Monte Carlo techniques for thin-film systems from chapter 3 and the parameters from chapter 4 (exchange parameters and anisotropic constants), we perform simulations for both isotropic and anisotropic classical Heisenberg models of Fe thin-films grown on W(001) substrates. As well as the experimental interest in these systems, a reason for choosing this material is that the 'exchange interaction' is short ranged. In our simulations, we compare the efficiency of the algorithms for the classical Heisenberg model. For the isotropic model, we consider the Metropolis, the bias Metropolis and the Wolff algorithms. For the anisotropic model, we compare the Metropolis and the Wolff algorithm in a modified version designed for our anisotropic model. We use the most efficient algorithm we have found in our simulations. Next, to compare with previous Monte Carlo works and to test our calculations, we perform the isotropic simulations for $2D$ square lattice and for bulk BCC structure. For the bulk structure, we find the analysis technique from chapter 2 works very well. However, for $2D$ systems, we do not succeed in applying the fourth order cumulant method owing to slow convergence with size of the magnetisation in finite systems. Instead we calculate the critical temperatures and 'susceptibility critical exponents' from susceptibility scaling functions. This technique is also applied to the analysis of thin-film results because of the slow convergence that also exists for such layered structures. The simulation results for both isotropic and and anisotropic models are compared and presented as a function of film thickness.

Finally, in chapter 6, we summarise the main findings of the thesis and judge the merit of the Monte Carlo method we have developed from its results. We also mention some further research which can be done to extend the current work of this thesis to other areas.

Chapter 2

Monte Carlo Simulations in Thermal Equilibrium Statistical Physics

2.1 Introduction

We begin this chapter with some basic statistical physics. We then explain some background for the simulations describing systems in equilibrium. After that, we introduce ways to analyse the data. Finally, we close this chapter by giving details on finite size scaling theory which tells us how to extract critical temperatures and exponents from our simulations.

2.2 Basic Statistical Physics

2.2.1 Partition Function

The expectation of a quantity Q for a system in equilibrium has the form

$$<Q> = \frac{1}{Z} \sum_{\mu} Q_{\mu} e^{-\beta E_{\mu}}, \tag{2.1}$$

where the partition function

$$Z = \sum_{\text{all states}} e^{-\beta H}, \tag{2.2}$$

where $\beta = (k_B T)^{-1}$ and H is the hamiltonian, is used to achieve various thermodynamical quantities. For example, the internal energy (the expectation of the energy) is

$$<E> = \frac{1}{Z} \sum_{\mu} E_{\mu} e^{-\beta E_{\mu}} = -\frac{\partial \ln Z}{\partial \beta}, \tag{2.3}$$

giving the specific heat

$$C = \frac{\partial U}{\partial T} = -k\beta^2 \frac{\partial U}{\partial \beta} = k\beta^2 \frac{\partial^2 \log Z}{\partial \beta^2}. \tag{2.4}$$

Moreover the free energy has the form

$$F = -k_B T \log Z. \tag{2.5}$$

From the free energy, the expectation of the magnetisation and the magnetic susceptibility can be obtained,

$$<M> = \frac{1}{Z} \sum_{\mu} M_{\mu} e^{-\beta E_{\mu}} = \frac{1}{\beta Z} \frac{\partial}{\partial B} \sum_{\mu} e^{-\beta E_{\mu}} = \frac{1}{\beta} \frac{\partial \log Z}{\partial B} = -\frac{\partial F}{\partial B}, \tag{2.6}$$

$$\chi \equiv \frac{\partial <M>}{\partial B} = -\frac{\partial^2 F}{\partial B^2}. \tag{2.7}$$

where B is an external magnetic field, a conjugate variable to the magnetisation $(H = -MB)$.

2.2.2 Fluctuations

In practice, the heat capacity C and magnetic susceptibility χ are formed by looking at fluctuations in the observable. For example, the mean square deviation of individual measurements of energy away from the average is

$$<(E- <E>)^2> = <E^2> - <E>^2, \qquad (2.8)$$

and

$$<E^2> = \frac{1}{Z}\sum_\mu E_\mu^2 e^{-\beta E_\mu} = \frac{1}{Z}\frac{\partial^2 Z}{\partial \beta^2}. \qquad (2.9)$$

Then from eq. (2.3) and eq. (2.8 - 2.9),

$$<E^2> - <E>^2= \frac{1}{Z}\frac{\partial^2 Z}{\partial \beta^2} - \left[\frac{1}{Z}\frac{\partial Z}{\partial \beta}\right]^2 = \frac{\partial^2 \log Z}{\partial \beta^2} = \frac{C}{k_B \beta^2}, \qquad (2.10)$$

which gives the expression for the specific heat as

$$C = k_B \beta^2 (<E^2> - <E>^2). \qquad (2.11)$$

Similarly, for the magnetic susceptibility, we obtain

$$<M^2> - <M>^2 = \frac{1}{\beta^2 Z}\frac{\partial^2 Z}{\partial B^2} - \left[\frac{1}{\beta Z}\frac{\partial Z}{\partial B}\right]^2 = \frac{1}{\beta}\frac{\partial <M>}{\partial B},$$
$$\chi = \beta(<M^2> - <M>^2). \qquad (2.12)$$

2.2.3 Phase Transition

In a magnetic material, the critical temperature T_C is a temperature which separates a disordered phase from an ordered phase. Above the critical temperature, the order parameter, the magnetisation M, is zero and it becomes finite when the system passes into the low temperature ordered phase, i.e. goes through a phase transition. At T_C the susceptibility also diverges in thermodynamic limit.

In studies of phase transitions such as paramagnetic-ferromagnetic transitions, it is of fundamental interest to examine the critical exponents (parameters used to

describe thermodynamic quantities near the critical temperature) which depend only on the symmetry of the order parameter and the dimension of the system. Thus, in this thesis, we will focus our studies upon the critical region of magnetic systems. We will do this by carrying computer simulations but describing these we firstly need to understand how the system changes as it approaches equilibrium.

2.3   Towards Thermal Equilibrium

In this section, the evolution of an initial state to a final state is presented. Then, the idea of making the average by using only states that play the main contribution is described.

2.3.1   Importance Sampling

The evolution of a state changing from an initial state μ to another state ν can be described by using the Master equation as

$$\frac{dw_\mu}{dt} = \sum_\nu [w_\nu(t)R(\nu \to \mu) - w_\mu(t)R(\mu \to \nu)]. \tag{2.13}$$

where respectively w_μ is the probability weight of a system in state μ at time t, and $R(\mu \to \nu)$ refers to the transition rate for the transition from state μ to state ν.

However, in thermal equilibrium, the probability weight $w_\mu(t)$ transforms to an equilibrium occupation probabilities as

$$p_\mu = \lim_{t \to \infty} w_\mu(t). \tag{2.14}$$

Moreover, for a system in thermal equilibrium with a reservoir at temperature T, this is equivalent to the Boltzmann distribution at temperature T [8],

$$p_\mu = \frac{1}{Z} e^{-\beta E_\mu}. \tag{2.15}$$

Then, we can now define the expectation value of Q by eq. (2.1) but this definition is practical only for small systems. For a larger system, we must choose some subset of the states to make the average instead. The best estimate of Q is given by

$$Q_{est} = \frac{\sum_{\mu=1}^{N} Q_{\mu} p_{\mu}^{-1} e^{-\beta E_{\mu}}}{\sum_{\mu=1}^{N} p_{\mu}^{-1} e^{-\beta E_{\mu}}}, \tag{2.16}$$

where Q_{est} is called the estimator of Q. When $N \to \infty$, $Q_{est} \to <Q>$. Thus the N states which we choose from the system need to make the important contribution in the sum of the estimator to get good estimate of $<Q>$ with small numbers of terms. This technique is called importance sampling.

In addition, we can also simplify the estimator if the subset of states are chosen with the Boltzmann probability $(p_{\mu} = Z^{-1} e^{-\beta E_{\mu}})$; so

$$Q_{est} = \frac{1}{N} \sum_{\mu=1}^{N} Q_{\mu}. \tag{2.17}$$

However, a Markov process is needed.

2.3.2 Markov processes

A Markov process is a mechanism which randomly generates a new state from an initial state. The probability of generating a new state μ by giving an old state ν is called the transition probability $P(\mu \to \nu)$. This probability depends only on the properties of the current state, not on any other states the system has been in. Moreover, in Markov processes, the transition probabilities $P(\mu \to \nu)$ satisfy the constraint $\sum_{\nu} P(\mu \to \nu) = 1$.

In Monte Carlo simulations, a Markov process is used to generate a Markov chain of states which appear with probabilities given by the Boltzmann distribution. However, in order to achieve this, the Markov process has to satisfy 2 conditions which are ergodicity and detailed balance.

10

Ergodicity

This condition is the requirement that it should be possible for the Markov process to reach any states of the system from any other states over a suitable time period. This is necessary so that the generating states have the correct Boltzmann probabilities. With this condition, some of the transition probabilities of the Markov process can be zero, but there must be at least one path of non-zero transition probabilities between any two states that are chosen.

Detailed balance

The condition of detailed balance is the microscopic reversibility which says that the probability of the system going from a state μ to state ν is the same as that of going from state ν to state μ i.e.

$$p_\mu P(\mu \to \nu) = p_\nu P(\nu \to \mu). \tag{2.18}$$

However, because we want the equilibrium distribution to be the Boltzmann distribution, p_μ and p_ν are set to be the Boltzmann probabilities. Then, the detailed balance eq. (2.18) becomes

$$\frac{P(\mu \to \nu)}{P(\nu \to \mu)} = \frac{p_\nu}{p_\mu} = e^{-\beta(E_\nu - E_\mu)}. \tag{2.19}$$

Usually, the probability $P(\mu \to \nu)$ is written as

$$P(\mu \to \nu) = g(\mu \to \nu)A(\mu \to \nu). \tag{2.20}$$

The quantity $g(\mu \to \nu)$ is the selection probability, the probability of generating a new state ν from an old state μ, and $A(\mu \to \nu)$ is the acceptance ratio, the probability of accepting that new state. Combining eq. (2.18 - 2.20), we get

$$\frac{P(\mu \to \nu)}{P(\nu \to \mu)} = \frac{g(\mu \to \nu)A(\mu \to \nu)}{g(\nu \to \mu)A(\nu \to \mu)} = e^{-\beta(E_\nu - E_\mu)}. \tag{2.21}$$

At this point, various algorithms in Monte Carlo simulations can have different selective probabilities and acceptance ratios. However, all of them adhere to the same concept of detailed balance eq. (2.21).

2.4   Implementation

To make a Monte Carlo simulation of a magnetic system, firstly, we set up an appropriate spin model and specify a lattice structure for the system (SC, BCC, or FCC). Secondly, we choose an algorithm and run the simulation. After that, we locate the equilibration point. Then, we start recording the measurements. Finally, we analyse the data and calculate the errors. Details of these are given in the following.

2.4.1   The Ising Model

In this simple model, the spin can be only +1 and -1. The hamiltonian is

$$H = - \sum_{<ij>} J_{ij} S_i S_j, \qquad (2.22)$$

where the notation $<ij>$ refers to the pairs. J_{ij} denotes the exchange parameter between site i and j.

Despite its simplicity and its inability to describe most real magnetic materials adequately, it can be solved exactly in one [9] and two dimensions [10]. Then, we can test our simulations for these cases. Moreover, because of its simplicity, we can also use it to study the development of the dimension crossover in thin-films before considering a more realistic model (by using the Heisenberg model discussed in a later chapter).

2.4.2 Monte Carlo Simulation Algorithms

There are different algorithms which use different probabilities and have different efficiencies. The most commonly used algorithms are the Metropolis algorithm [11] and the Wolff algorithm [12].

The Metropolis Algorithm

This is one of the simplest algorithms in Monte Carlo simulation. The algorithm defines that each new state is different from the old state by a single spin. Thus, if there are N spins in the system, there can be N different spins we can choose, and hence N possible states we can make from the initial state. Because of this, there are N selection probabilities and each of them has

$$g(\mu \to \nu) = \frac{1}{N}. \tag{2.23}$$

With these selection probabilities, the condition of detailed balance eq. (2.21) becomes

$$\frac{P(\mu \to \nu)}{P(\nu \to \mu)} = \frac{A(\mu \to \nu)}{A(\nu \to \mu)} = e^{-\beta(E_\nu - E_\mu)}. \tag{2.24}$$

However, to make the algorithm as efficient as possible, the acceptance probabilities have to be as large as possible. A way to do this is to give the larger part of the two ratios the largest possible value, and adjust the other to satisfy the constraint. For instance, if $E_\mu < E_\nu$, $A(\nu \to \mu)$ is larger than the other so we set it to be one, and $A(\mu \to \nu)$ is set to be $e^{-\beta(E_\nu - E_\mu)}$ to satisfy eq. (2.24); thus,

$$A(\mu \to \nu) = \begin{cases} e^{-\beta(E_\nu - E_\mu)} & \text{if } E_\nu - E_\mu > 0 \\ 1 & \text{otherwise} \end{cases} \tag{2.25}$$

13

The Wolff Algorithm

This algorithm is based on the observation that spins can be grouped together and all spins in a group can be flipped at the same time. The main purpose is to reduce the correlation time (to be described later) which in turn helps to reduce statistical errors.

To apply this algorithm to the Ising model, a random seed spin (S_i) is chosen. Then those of the neighbouring spins (S_j) that are pointing in the same direction are added with a probability $P(S_i, S_j) = 1 - e^{-2\beta J_{ij}}$ to form a group. Next, we repeat this process for just the added neighbour spins, whilst ignoring the spins that are already in the group, until no more new spins are added. Finally, all spins in the group (cluster) are flipped, $S_i \rightarrow -S_i$.

In this way, ergodicity is guaranteed because P can be very small so that the cluster contains only one site. Then, any configurations can be reached in a suitable time scale. Also, for the detailed balance, by choosing the adding probability in this way, it gives $\frac{A(\mu \rightarrow \nu)}{A(\nu \rightarrow \mu)} = 1$ (e.g. see [13]). So the cluster is always flipped.

The main benefit of using the Wolff algorithm rather than the much simpler Metropolis algorithm is the dramatic reduction in correlation time. The correlation time arises from any one state being created from previous states. So, many states are correlated to many other states and this can increase the statistical errors in terms of correlation. The Metropolis algorithm updates each spin individually. This makes spins in the ferromagnetic phase to have less tendency update because to make one spin align differently from its neighbour costs a large energy. Then, the average may be calculated from many states which are the same. However, the Wolff algorithm allows more than one spin to flip (and always flip) at the same time. Thus, this can push the system to a state which is far more different from the previous state than one obtained from the Metropolis algorithm. As a result, it produces less

correlation. So, it improves statistical errors (described in a later section).

2.4.3 Equilibration

Because we are interested only in static behaviour, we discard any measurements taken before the system reaches its equilibrium point. The time to reach this point is the equilibration time τ_{eq}, and any measurements taken before this time belong to dynamic behaviour. One of the simplest ways to find the equilibration time is to plot the observables of interest against time and find the point where the observables start fluctuating within a narrow range around their mean. Moreover, we can also improve the accuracy of finding the equilibration time by introducing another simulation starting with different initial configuration. At the equilibrium, both of them should give the same mean (average).

2.4.4 Observables

When the system is in an equilibrium state, we record the total energy (the hamiltonian)

$$E = - \sum_{<ij>} J_{ij} S_i S_j \tag{2.26}$$

and the magnetisation per spin

$$m = \frac{1}{N} \sum_i^N S_i \tag{2.27}$$

as a function of time. Then, from the fluctuation in the magnetisation, we calculate the susceptibility

$$\chi = \beta N (<m^2> - <m>^2). \tag{2.28}$$

2.5 Analysis

2.5.1 Statistical Errors

In the Monte Carlo simulation, the main source of the error is from the fluctuation. Thus, if we perform the simulation making n measurements of the magnetisation m's during a particular run, we calculate the standard deviation by

$$\sigma = \sqrt{\frac{1}{N}[<m^2> - <m>^2]}. \qquad (2.29)$$

However, for small N, we need to replace N by $N - 1$.

This standard deviation (for a normal distribution) represents how good the expectation is as about 68% of the data lying around the mean in region $<m> \pm \sigma$.

In some cases, we can not use this direct way to find the error as some quantities, for example the magnetic susceptibility χ, are calculated from the fluctuation of the mean. We need to use a re-sampling method like the jackknife method (e.g. see [14]) to calculate the error.

In the jackknife method, suppose that there are n data of the magnetisation, we take the first magnetisation m_1 out and calculate χ_1. Then, putting m_1 back, taking m_2 out, we calculate the χ_2. After that, we repeat the process for all χ_i's and the estimate of the error is

$$\sigma = \sqrt{\sum_{i=1}^{N}(\chi_i - \chi)^2}, \qquad (2.30)$$

where χ is calculated from all N data.

However, finding the statistical errors in this way, each data in the series has to be independent from any other. Nevertheless, the quantities we measure from the simulations (for instance, the magnetisation) at a particular state are created from previous states. Thus, this creates another kind of statistical error in terms of a correlation.

2.5.2 Integrated Correlation Time

As we use the Markov process to update our magnetic system, our results (e.g. m's) are not independent. The correlation among them can be described by considering the expectation value of the square of the statistical error [15]

$$
\begin{aligned}
<(\delta m)^2> &= \left\langle \left[\frac{1}{N} \sum_{t=1}^{N} (m_t - <m>) \right]^2 \right\rangle \\
&= \left\langle \frac{1}{N^2} \sum_{t=1}^{N} (m_t - <m>)^2 \right\rangle \\
&\quad + \left\langle \frac{2}{N^2} \sum_{t=1}^{N} \sum_{t'>t}^{N} (m_t - <m>)(m_{t'} - <m>) \right\rangle.
\end{aligned} \tag{2.31}
$$

For the second sum from the second term on the right hand side, there are $(N - t)$ terms for each t in the first sum. Hence, it is possible to write [15]

$$
\begin{aligned}
<(\delta m)^2> &= \frac{1}{N}(<m^2> - <m>^2) + \frac{2}{N^2} \sum_{t=1}^{N} (N - t)[<m_0 m_t> - <m>^2] \\
&= \frac{1}{N}(<m^2> - <m>^2)(1 + 2\tau),
\end{aligned} \tag{2.32}
$$

where $\tau = \sum_{t=1}^{N} (1 - \frac{t}{N}) \frac{<m_0 m_t> - <m>^2}{<m^2> - <m>^2}$ is called integrated correlation time and the smaller this term, the less dependent among the data in the system. Thus, the algorithm used in a simulation should produce as small a τ as possible.

However, we may be able to discard τ, from the fact that $\phi(t) = \frac{<m_0 m_t> - <m>^2}{<m^2> - <m>^2}$ decays with time, by re-sampling the data with time interval Δt between two successive data at least 2τ (e.g. see [13]). Thus, we can now assume that there is no correlation in our new data set.

2.5.3 Extrapolation Technique

When carrying out a Monte Carlo simulation, to find the location of the critical temperature T_C is time consuming as we do not know exactly where the critical

point is. So, we need to perform many short simulations at several temperatures to guess roughly the T_C at which the variation with temperature of the magnetisation is greatest and where the susceptibility shows a peak. After that, we can proceed by making a long simulation at the guessed T_C and record a series of data, and use an extrapolation technique to achieve data from nearby temperatures to find the actual T_C (by using finite size scaling technique e.g. [16]). As a result, we can save a lot of computer resource (time).

Single Histogram

The single histogram technique [17] uses extrapolation to extract some results from the temperatures around the temperature at which we perform the simulation, T_0. Recalling the ordinary estimator eq. (2.16), instead of choosing p_i as its own Boltzmann probability, we choose p_i to be the same as the Boltzmann probability from the performed temperature T_0. Thus,

$$
\begin{aligned}
Q_{est}(\beta) &= \frac{\sum_i Q_i e^{-(\beta-\beta_0)E_i}}{\sum_i e^{-(\beta-\beta_0)E_i}} \\
&= \frac{\sum_{E,Q} Q N(E,Q) \exp(-(\beta-\beta_0)E)}{\sum_{E,Q} N(E,Q) \exp(-(\beta-\beta_0)E)} ,
\end{aligned}
\tag{2.33}
$$

where $\beta_0 = 1/k_B T_0$, and $N(E,Q)$ is the two dimensional histogram for the energy E and the observable Q.

The reason of using the histogram $N(E,Q)$ instead of raw data Q_i's and E_i's is that in the past the media for data recording was expensive. However, although the media are much cheaper and large memory is more readily available now, we still find some advantages in terms of computer time i.e. we do not have to go through every raw data but use the histogram bins instead. Nevertheless, the bin should not be too large to bring significant error or too small to use unnecessarily computer resource. The optimum size is found by experiment.

18

However, there are two main problems with the histogram method. One is that it becomes unfeasible to fit the histogram in the computer memory with the extensive variables, E and Q. So, instead of making two-dimensional histogram (E and Q are indices), we follow [16] and use one-dimensional arrays to keep the average of Q as a function of E (by performing the sums over Q first) as

$$Q_{est}(\beta) = \frac{\sum_E <Q(E)> N(E) \exp(-(\beta - \beta_0)E)}{\sum_E N(E) \exp(-(\beta - \beta_0)E)}, \tag{2.34}$$

where $<Q(E)>$ is the constant energy average of Q.

The other problem is that when making the summation of the exponential function, both numerator and denominator exceed the computer limit whereas the fraction does not. The solution to this is to perform the summation in logarithmic terms [13]. For example, for two large numbers, x_1 and x_2, with their logarithms l_1 and l_2 with $l_1 \geq l_2$, the logarithmic sum is

$$\begin{aligned}
\log(x_1 + x_2) &= \log(e^{l_1} + e^{l_2}) = \log(e^{l_1}(1 + e^{l_2 - l_1})) \\
&= l_1 + \log(1 + e^{l_2 - l_1}).
\end{aligned} \tag{2.35}$$

Then, when expressing both numerator and denominator sum in logarithmic forms, we can calculate Q_{est} in eq. (2.34) as

$$Q_{est} = \frac{\text{num.}}{\text{denom.}} = e^{\log(\text{num.}) - \log(\text{denom.})}. \tag{2.36}$$

One more thing to be aware of is the range of making the extrapolation. From eq. (2.33), the histogram weight

$$W(E, Q) = \frac{N(E, Q)e^{-(\beta - \beta_0)E}}{\sum_{E,Q} N(E, Q)e^{-(\beta - \beta_0)E}} \tag{2.37}$$

is proportional to $N(E, Q)$ at the temperature $\beta = \beta_0$ at which the original simulation was performed. As a result, when β strays too far from β_0, the weight $W(E, Q)$ gives Q_{est} incorrectly [13].

19

One solution to this is to allow the largest $\triangle T = T - T_0$ which satisfies the criterion [18]

$$|U(T) - U(T_0)| \leq \sigma_E, \qquad (2.38)$$

where $U \equiv <E>$ and σ_E is standard deviation of E at T_0.

2.5.4 Finite Size Scaling

Because we can only model the real system by running the simulation for finite sizes and times, according to limitations of computer memory and time, we have to consider finite size effects which make properties behave differently from those in the thermodynamic limit. For this reason, we need finite size scaling theory to analyse the data measured from finite size simulations.

The Finite Size Method : Introduction

In the vicinity of a phase transition, where the order parameter of the system has to move from a symmetric to a broken symmetric state (or vice versus), lots of fluctuation occurs bringing about large correlation in this region. Usually, this kind of correlation is characterised by the correlation length ξ which diverges at the critical point.

In a magnetic system, the thermodynamic properties such as the susceptibility χ and the magnetisation m are also characterised by the correlation length ξ in the critical region and they vary as [19, 20]

$$\xi \propto |t|^{-\nu},$$
$$m \propto |t|^{\beta},$$
$$\chi \propto |t|^{-\gamma},$$

$$(2.39)$$

where $t = \frac{T - T_C}{T_C}$ is the reduced temperature used to measure the distance away from critical point. Here, the critical exponents γ, β, and ν depend only on symmetry of the order parameter m and the dimension of the system.

All the equations in eq. (2.39) represent asymptotic expressions and valid only when $t \to 0$. Notice m in eq. (2.39), the equation is for a system below the critical temperature.

In any finite size systems, the system's linear dimension length L has the effects on the correlation length such that if $L \gg \xi$, no significant finite size effect should be observed. Nevertheless, when $L \ll \xi$, the system size will cut off the correlation length so that a finite size rounding of the critical point is expected. Then, by rewriting the susceptibility χ and in terms of correlation length ξ in eq. (2.39) (e.g. [13],[20]-[23]), we get

$$\chi = \xi^{\gamma/\nu} \chi_0(L/\xi), \qquad (2.40)$$

where χ_0 is a dimensionless function and has the properties

$$
\begin{aligned}
\chi_0(x) &= \text{constant} && \text{for } x \gg 1 \\
&\sim x^{\gamma/\nu} && \text{as } x \to 0,
\end{aligned}
\qquad (2.41)
$$

which leaves χ untouched in thermodynamic limit, but limits χ corresponding to the system dimension L in critical region. However, χ_0 is not very useful as it still contains the correlation length ξ. For this reason, it is more conventional and convenient to define a scaling function such that

$$\tilde{\chi}(x) = x^{-\gamma} \chi_0(x^\nu), \qquad (2.42)$$

then, we get

$$\chi = L^{\gamma/\nu} \tilde{\chi}(L^{1/\nu} t). \qquad (2.43)$$

Notice that the absolute of the reduced temperature t is taken out to allow the scaling function below T_C to behave differently from the scaling function above T_C.

This is in an agreement with the behaviour of χ as it is not symmetric on the two sides of the phase transition. Similarly, we can write the magnetisation m as

$$m = L^{-\beta/\nu}\widetilde{m}(L^{1/\nu}t), \qquad (2.44)$$

but, as has mentioned before, it is valid only in the magnetically ordered phase.

Now, the next step is to find T_C from finite sizes. One of the ways to do this is to look at the scaling functions $\widetilde{\chi}$'s near T_C among different sizes because they should lie on the same curve if we use correct values of ν and T_C. However, to guess both ν and T_C is not practical especially when the data is not perfect (i.e. finite system size and measurements over finite time).

Then, the next way is to consider the scaling variable $x = L^{1/\nu}t$, and we can write

$$T_0 = T_C(1 + x_0 L^{-1/\nu}), \qquad (2.45)$$

where $x_0 = L^{1/\nu}\left(\frac{T_0 - T_C}{T_C}\right)$ and T_0 is temperature where χ in finite size gets its peak. So, by plotting T_0 against L and using correct ν, we can locate T_C at the y-intercept. Nevertheless, ν must be known beforehand.

Fortunately, there is also another way of finding the T_C very accurately by using the fourth order cumulant [24] as

$$U_L = 1 - \frac{1}{3}\frac{<m^4>}{<m^2>}, \qquad (2.46)$$

which for different sizes of L's produce the same U_L at the critical point making $(U_{L'}/U_L)_{T=T_C} = 1$ where $L' = bL$. This fourth order cumulant is derived from spin probability distribution function in finite size scaling theory [22].

However, in finite systems, there seem to be the presence of residual corrections to finite size scaling [24]. As a result, to use the cumulant to locate the T_C correctly, one actually needs to plot $T_C(b)$ against $(\ln b)^{-1}$, and extrapolate the results of the method for $(\ln b)^{-1} \to 0$ [24].

22

2.6 Conclusion

In this chapter, we have presented the statistical physics theoretical background for the Monte Carlo simulation. In next chapter, we will move onto describing Monte Carlo simulation in Ising thin films to study how thickness of the films relates to the properties of the Ising magnet in the critical region.

Chapter 3

Ising Thin-Film Simulations

3.1 Introduction

In this chapter, we aim to study magnetic thin-film systems near critical temperatures T_C and examine how T_C and critical exponents relate to the film thickness. Then, we apply finite size scaling method to systems with layered geometries where the in-plane and out-of-plane dimensions of the films are different i.e. $L_x = L_y = L$ and $L_z = l \ll L$ (z is treated to be a normal direction to the film surface).

In the finite size technique, we consider the correlation length ξ near T_C. The two-dimensionality of the behaviour of the films should start when the correlation length along the out-of-plane direction is the same size as the film thickness l. On the other hand, along the in-plane direction, the correlation length is still smaller than the film size L, and becomes the same size as L when $T \to T_C$.

So, we assume that for this thin-film structure ($L_x = L_y = L$ and $L_z = l \ll L$), close to T_C, a single correlation length $\xi = \xi_x = \xi_y$ is enough to describe the thin-film systems because we may be able to treat $\xi_z = l$ as a constant. Then,

within this assumption, we study formulae based on the two-point correlation of the magnetisation to investigate how the critical exponents scale with film thickness. Also, for the critical temperatures T_C, we use the fourth order cumulant U_L of the magnetisation [24] described in chapter 2 as a way to extract T_C from the thin-film geometries.

In brief, we use Monte Carlo simulations of Ising thin-films to check the validity of our assumption via the hyperscaling relation (the following section). Next, we extract T_C and critical exponents for each thin-film system. Finally, we close this chapter by summarising the simulation results and the conclusion of their behaviour. This is preliminary to the studies of the more complicated but realistic system, Heisenberg model, which we will describe in the next chapter.

3.2 Finite Size Scaling in Thin-Films

In this section, we propose a method used to investigate how magnetic behaviour relates to the size of the system in critical region. For example, in thin-films $L \times L \times l$ where l is the film thickness and fixed, we vary the film size $L \times L$ to find how the magnetic susceptibility and the magnetisation scale with L at the phase transition.

3.2.1 Critical Exponents and Temperatures

With the assumption that only a single correlation length ξ is required, the hyperscaling relation should be satisfied as [25, 26]

$$d\nu = \gamma + 2\beta = 2 - \alpha, \tag{3.1}$$

$$(2 - \eta)\nu = \gamma, \tag{3.2}$$

where d is the dimension of the system. Then, by following the idea in [27] (finite size scaling in anisotropic shaped structures), we apply this technique to thin-film

systems by starting with the connected two-point correlation function (e.g. consider [21]) of the magnetisation as

$$G_c^{(2)}(r) \equiv \ <m(\vec{r}_1)m(\vec{r}_2)> - \ <m>^2,$$ (3.3)

$$\equiv \ <m(0)m(r)> - \ <m>^2,$$

where $r = |\vec{r}_1 - \vec{r}_2|$ and $m(\vec{r}_1)$ is the magnetisation magnitude at $\vec{r}_1$. However, at T_C (reduced temperature $t = 0$), the asymptotic form for the correlation function for isotropic-shape systems is [28]

$$G_c^{(2)}(r, t = 0) \sim \frac{1}{r^{d-2+\eta}} \sim (x^2 + y^2 + z^2)^{-(d-2+\eta)/2},$$ (3.4)

where η is the critical exponent for $G_c^{(2)}$. Suppose that this correlation function is also valid for anisotropic-shape system e.g. thin-films, if we consider the susceptibility

$$k_B T \chi = \frac{1}{L_x L_y L_z} \sum_{x_1=1}^{L_x} \sum_{y_1=1}^{L_y} \sum_{z_1=1}^{L_z} \sum_{x_2=1}^{L_x} \sum_{y_2=1}^{L_y} \sum_{z_2=1}^{L_z} <m(x_1, y_1, z_1)m(x_2, y_2, z_2)> - \ <m>^2,$$
(3.5)

and using the periodic boundary condition along xy directions, we get

$$k_B T \chi = \frac{1}{L_z} \sum_{x=1}^{L_x} \sum_{y=1}^{L_y} \sum_{z_1=1}^{L_z} \sum_{z_2=1}^{L_z} <m(1, 1, z_1)m(x, y, z_2)> - \ <m>^2.$$ (3.6)

Then, by changing the index z_2 to $z_1 + z$, we get

$$k_B T \chi = \frac{1}{L_z} \sum_{x=1}^{L_x} \sum_{y=1}^{L_y} \sum_{z_1=1}^{L_z} \sum_{z=1-z_1}^{L_z-z_1} <m(1, 1, z_1)m(x, y, z_1 + z)> - \ <m>^2.$$ (3.7)

If L_x and $L_y \gg 1$, the sum can be replaced by the integral by choosing the lattice spacing as unity,

$$k_B T \chi \simeq \frac{1}{L_z} \int_0^{L_x} dx \int_0^{L_y} dy \sum_{z_1=1}^{L_z} \sum_{z=1-z_1}^{L_z-z_1} <m(0, 0, z_1)m(x, y, z_1 + z)> - \ <m>^2.$$
(3.8)

Next, by changing the variable $x \to L_x x'$ and $y \to L_y y'$, and including condition in eq. (3.3) and (3.4) that $<m(0,0,z_1)m(x,y,z_1+z)>_{T_C} \propto (x^2+y^2+z^2)^{-(d-2+\eta)/2}$, we rewrite the susceptibility as

$$
\begin{aligned}
k_B T_C \chi(T_C) \quad \simeq \quad & \frac{(L_x L_y)^{1-(d-2+\eta)/2}}{L_z} \int_0^1 dx' \int_0^1 dy' \times \\
& \sum_{z_1=1}^{L_z} \sum_{z=1-z_1}^{L_z-z_1} \left(\frac{L_x x'^2}{L_y} + \frac{L_y y'^2}{L_x} + \frac{z^2}{L_x L_y} \right)^{-(d-2+\eta)/2} .
\end{aligned}
\tag{3.9}
$$

Nevertheless, in thin-film structure, we set $L_x = L_y \equiv L$ and $L_z \equiv l$, then

$$
\begin{aligned}
k_B T_C \chi(T_C) \quad \simeq \quad & \frac{(L^2)^{1-(d-2+\eta)/2}}{l} \int_0^1 dx' \int_0^1 dy' \times \\
& \sum_{z_1=1}^{l} \sum_{z=1-z_1}^{l-z_1} \left(x'^2 + y'^2 + \frac{z^2}{L^2} \right)^{-(d-2+\eta)/2} .
\end{aligned}
\tag{3.10}
$$

As $z \in [1-l, l-1]$ and we set $l \ll L$ so $\frac{z^2}{L^2} \ll 1$. Thus, we may discard the term $\frac{z^2}{L^2}$. As a result, $\sum_{z_1=1}^{l} \sum_{z=1-z_1}^{l-z_1} (x'^2 + y'^2 + \frac{z^2}{L^2}) \approx l^2(x'^2 + y'^2)$. So the susceptibility becomes

$$
\begin{aligned}
k_B T_C \chi(T_C) \quad \sim \quad & l(L^2)^{1-\frac{d-2+\eta}{2}} \int_0^1 dx' \int_0^1 dy' (x'^2 + y'^2)^{-(d-2+\eta)/2}, \\
\propto \quad & L^{\frac{\gamma}{\nu}+2-d} l,
\end{aligned}
\tag{3.11}
$$

where the scaling relation $\gamma/\nu = 2 - \eta$ [26] is used. Notice that for a particular thin-film system, l is a constant, the only variable in the scaling is L i.e.

$$
\chi(T_C) \propto L^{\frac{\gamma}{\nu}+2-d}.
\tag{3.12}
$$

We have verified that this formula is also valid in thick thin-film case as long as $l \ll L$. However, when l approaches L, the formula should be no longer valid as the integral part is now L dependent.

Now turning to the magnetisation $<m>$, we may assume that $<m>$ is of the same order as the root mean square magnetisation $<m^2>_{T_C}^{1/2}$,

$$
<m>_{T_C} \quad \propto \quad <m^2>_{T_C}^{1/2},
$$

27

$$= \left[\frac{k_B T_C \chi(T_C)}{L^2 l} \right]^{1/2},$$

$$\propto L^{-\beta/\nu}, \tag{3.13}$$

where again we use $-\frac{\beta}{\nu} = \frac{\gamma}{2\nu} - \frac{d}{2}$ [26]. However, one may argue that, by approaching T_C from above, $<m>_{T_C}$ should be zero. This is correct only in the thermodynamical limit and not in a finite size simulation. Also, as can be seen, $<m>$ scales only with L in the same way as isotropic shaped systems.

To find T_C, it is possible by considering the fourth order cumulant [24] . At T_C, for a particular thickness, it is expected that [23, 29]

$$U_L(T_C, l) \simeq \tilde{U}(l). \tag{3.14}$$

In detail, to understand the cumulant in thin-films more clearly, the investigation of the four spin correlation function is needed. Nevertheless, if the curves of U_L's from various L's cross at the same temperature then this method is valid.

3.2.2 Scaling Functions

A way to check how good the critical exponents are is to consider the scaling function i.e. if using the correct exponents, close to T_C, the scaling function for different lattice sizes should collapse onto the same curve. Then, we can expand the susceptibility functions eq. (3.11) and the magnetisation eq. (3.13) for nearby temperatures.

For a thin-film system, as we mentioned before, the film-behaviour should start when the correlation length ξ along the out-of-plane direction becomes the same size as the thickness ($\xi_z = l$), whereas along the in-plane direction, the correlation length ($\xi_x = \xi_y \equiv \xi$) should still be smaller than L. However, when $\xi \rightarrow L$, there will be a cut off behaviour.

Then, by matching eq. (2.43) with eq. (3.11) and eq. (2.44) with eq. (3.13), we

28

expect

$$\chi(T,l) \quad = \quad L^{(\gamma/\nu)'}\widetilde{\chi}(L^{1/\nu}t,l), \qquad (3.15)$$

$$<m(T,l)> \quad = \quad L^{-\beta/\nu}\widetilde{m}(L^{1/\nu}t,l). \qquad (3.16)$$

where $(\gamma/\nu)' \equiv \gamma/\nu + d - 2$ and the thickness l is absorbed into the scaling function $\widetilde{\chi}(L^{1/\nu}t,l)$. Nevertheless, in this case, the exponent ν must be known before hand. Fortunately, from [24], it was shown that the slope of the cumulant at T_C, or anywhere in the finite-size scaling region, varies with system size like $L^{1/\nu}$. Thus, we can use this technique to calculate ν and also the scaling functions.

3.3   Simulation

3.3.1   Lattice Structure and Implementation in Computer Memory

For a simple cubic (SC) system, it is straightforward to use a three-dimensional array to store the spins. However, the maximum size in each dimension should be equal to 2^n where n is a positive integer to save computer time [30]. Then, this sometimes requires extra memory when the length in each dimension is not equal to 2^n. So, instead, we use a one-dimensional array and create a mapping function to match an array index to the location of a spin in the actual lattice structure.

For the boundary condition, for our thin-film structure, we use helical periodic boundary conditions along the in-plane direction (x and y directions). For the out-of-plane (z) direction, we set a free boundary.

In SC films with L lattice points along the in-plane directions (x,y) and l points (layers) along the out-of-plane directions (z), the nearest neighbour sites to a site i are

1. in-plane directions: $i + 1, i - 1, i + L, i - L$

2. out-of-plane directions: $i + L^2$, $i - L^2$

Now, by considering the FCC and BCC structure, the simplest way to create those structures is to treat them as sub lattices of the cubic lattices. If we use (h, k, l) as indices of a point in a cubic lattice, when $h + k + l$ is even, this site belongs to FCC lattice. Nevertheless, if h, k, and l are either all even or all odd, it belongs to BCC lattice. However, in this way, respectively half and 3/4 of the space is unused in FCC and BCC lattice. Then, again, we use one-dimensional arrays and use mapping functions for FCC and BCC structures so that each element in the arrays refers to a lattice point.

For FCC films, we construct the film structure as shown in figure (3.1).
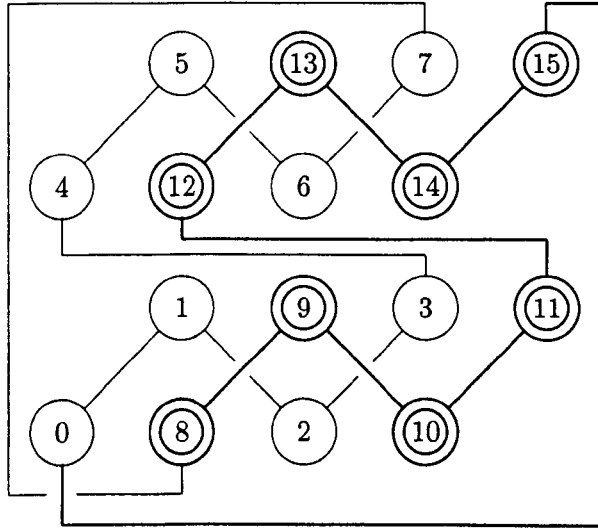
Figure 3.1: FCC thin-film structure for $L = 4$ and $l = 2$. The single circles are lattice points in even (bottom) layer and the double circles are for odd (top) layer.

By this way, we can create FCC films by adding more even and odd layers and so on. From the figure, the nearest neighbours to site i are set according to the following prescriptions:

30

1. in-plane direction :

   (a) if i mod 2 is even : $i - L - 1, i - L + 1, i - 1, i + 1$

   (b) if i mod 2 is odd : $i + L - 1, i + L + 1, i - 1, i + 1$

2. out-of-plane :

   (a) if i is in an even layer

      i. if i mod 2 is even : $i \pm \frac{L^2}{2}, i \pm \frac{L^2}{2} - 1, i \pm \frac{L^2}{2} - 2, i \pm \frac{L^2}{2} - L - 1$

      ii. if i mod 2 is odd : $i \pm \frac{L^2}{2}, i \pm \frac{L^2}{2} - 1, i \pm \frac{L^2}{2} - 2, i \pm \frac{L^2}{2} + L - 1$

   (b) if i is in an odd layer

      i. if i mod 2 is even : $i \pm \frac{L^2}{2}, i \pm \frac{L^2}{2} + 1, i \pm \frac{L^2}{2} + 2, i \pm \frac{L^2}{2} - L + 1$

      ii. if i mod 2 is odd : $i \pm \frac{L^2}{2}, i \pm \frac{L^2}{2} + 1, i \pm \frac{L^2}{2} + 2, i \pm \frac{L^2}{2} + L - 1.$

For BCC films, as can be seen figure (3.2), the nearest neighbours are not in the same layer but either in the upper and lower layers. The prescription is

1. if i is in an even layer : $i \pm \frac{L^2}{4} - 1, i \pm \frac{L^2}{4}, i \pm \frac{L^2}{4} - \frac{L}{2}, i \pm \frac{L^2}{4} - \frac{L}{2} - 1.$

2. if i is in an odd layer : $i \pm \frac{L^2}{4} + \frac{L}{2}, i \pm \frac{L^2}{4} + \frac{L}{2} + 1, i \pm \frac{L^2}{4}, i \pm \frac{L^2}{4} + 1$

Notice that we have defined the linear dimension L by looking at the projection of points on a particular axis (e.g. x). Then, L equals to number of lattice points on that projected axis. Also, because we use free a boundary condition for the surface layers, there will be no neighbouring site below the bottommost layer and above the topmost layer.

3.3.2 Random Number Generator

Random numbers play a vital role in Monte Carlo simulations. As the algorithm can only provide the probability to move onto another state, we need a random
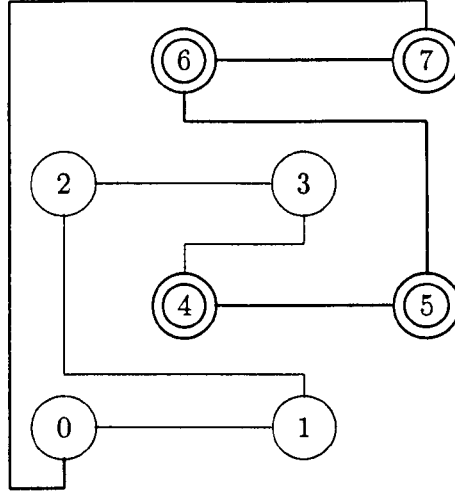
Figure 3.2: BCC thin-film structure for $L = 4$ and $l = 2$

number $[0, 1)$ to accept or reject that moving. However, non-uniform and correlated pseudo-random number generators can severely give incorrect results [31]. Then, before using a generator, we need to test it first. A good generator should give a series of random numbers as an uncorrelated sequence with long period, uniform, and use modest computer time in comparison with the whole simulation (e.g. see [32]).

We decided to use the generator **drand48** $LCG(2^{48}, 5DEECE66D_{16}, 11)$ which is employed by the ANSI C. The reasons are that it gives good results for the spectral test (structure analysis) [32, 33]. Moreover, used in a test Monte Carlo simulation [34], it led to results which agreed very well with the exact results for $2D$ Ising model .

3.3.3 Ising Hamiltonian

The hamiltonian of Ising model is defined as

$$H = - \sum_{<ij>} J_{ij} S_i S_j, \qquad (3.17)$$

where $<ij>$ discards any double sums and S_i can be only ± 1. To compare with the exact result for $2D$ [10] ($k_B T_C/J \approx 2.269$), we set $J_{ij} = 1$ where site i and j are nearest neighbour and $J_{ij} = 0$ otherwise. With this type of hamiltonian, we can measure the energy and the magnetisation as

$$m = \frac{1}{N} \sum_i S_i, \qquad (3.18)$$

$$E = - \sum_{<ij>} J_{ij} S_i S_j, \qquad (3.19)$$

and the magnetic susceptibility per spin is calculated from

$$\chi = \beta N (<m^2> - <m>^2). \qquad (3.20)$$

3.3.4 Simulation Techniques

To study the critical behaviour in the Ising films, we perform Monte Carlo simulations for SC, BCC, and FCC films with film thicknesses l as 1,2,4,6,8,10,15 and 20 using Ising hamiltonian with $J_{ij} = 1$ only for first nearest neighbours and zero otherwise. However, in the BCC films, we omit monolayer as the first nearest neighbour is the actual second nearest neighbour in BCC structure. Next, for each film thickness, we vary the film size $L \times L$ with L ranging from 48 to 128 (using a step of 16). In addition, we also perform simulations for bulk systems ($L \times L \times L$) with the same L's as in thin-film case. However, in bulk systems, we perform 2 runs using 2 different boundary conditions for the surface layers i.e. free and periodic boundary conditions.

Equilibration

As our interest is the static behaviour, during the simulation, before making any measurements, we need to ignore some states to allow the system to reach the equilibrium state. Then, we make some test simulations for both Wolff and Metropolis algorithms (discussed in the previous chapter). The magnetisation of the 128×128 Ising model as a function of time (measured in Monte Carlo steps per site) is shown in figure (3.3).

In the Metropolis algorithm, the number of Monte Carlo steps per site (mcs/site) is defined in terms of the number of attempts to flip one spin per site. Then, in this way, it does not mean that for 1 mcs/site a spin must be flipped. However, for the Wolff algorithm, as all spins in a group will be flipped once a group is formed, we then define the Monte Carlo step per site in terms of the number of attempts to add one spin into a group per site.

From the figure (3.3), for low and high temperatures, the equilibration time for both Wolff and Metropolis algorithms seem to be the same. However, when the temperature is close to T_C (for $2D$ Ising model, $T_C \approx 2.269$), by using the Wolff algorithm, the system reaches the equilibrium state faster. Moreover, if we consider the flipping percentage

$$\text{Flipping Percentage} = \frac{\text{number of spins that are successfully flipped}}{\text{number of attempts to flip spins}} \times 100, \quad (3.21)$$

where in the Wolff algorithm, the number of attempts to flip spins changes to the number of attempts to add spins into groups, we can compare the efficiency of these two algorithms as in figure (3.4). Also in the figure, we investigate the real c.p.u. time used to successfully update a spin for both algorithms. In the simulations, for this Ising model, 90 percent of all operations in flipping are bitwise operations (mostly exclusive nor and or) to minimise computer time usage. The processor we used is a Pentium III 800 MHz for this comparison.
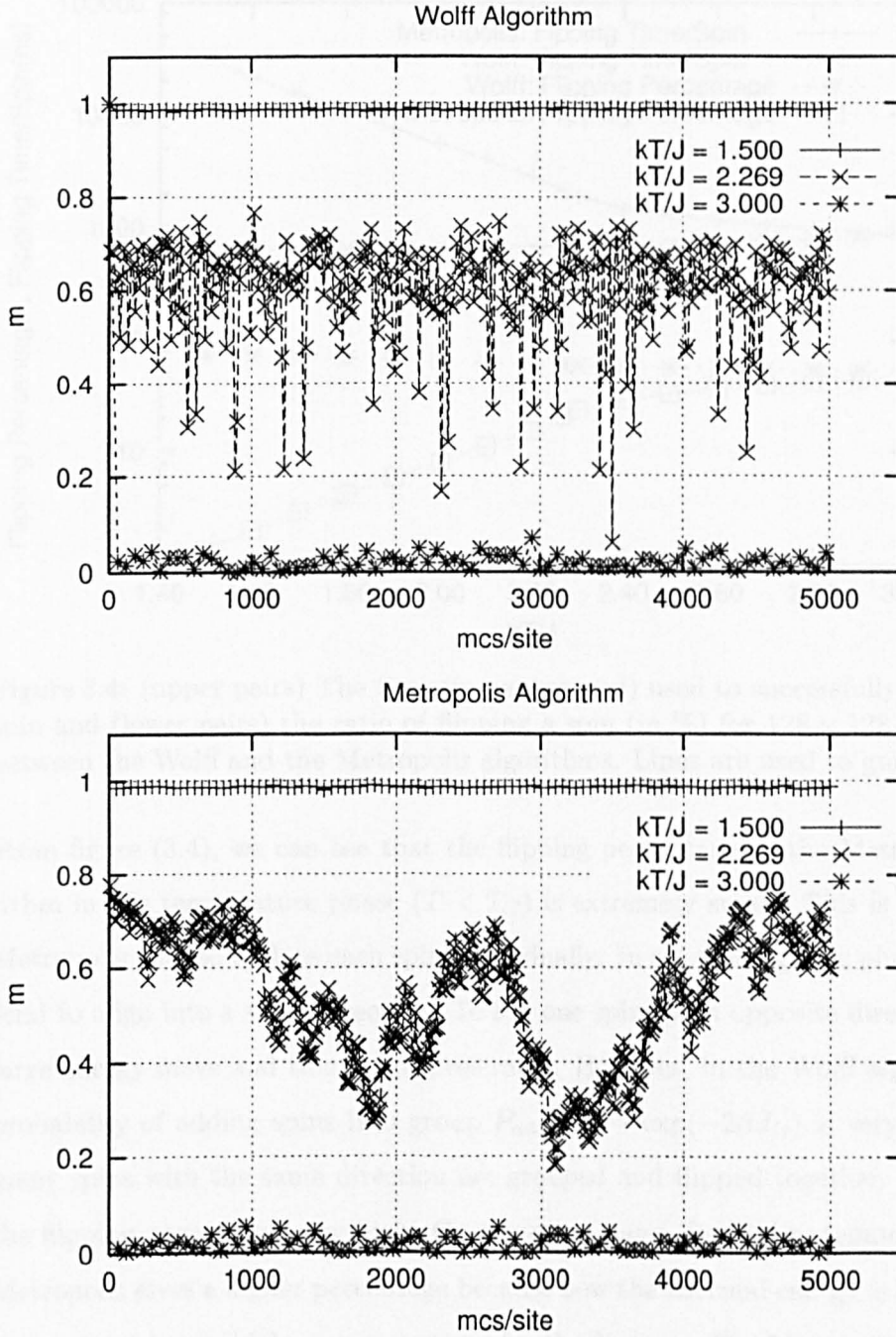
Figure 3.3: The magnetisation per spin (m) of 128×128 Ising model using the Wolff algorithm (upper figure) and the Metropolis algorithm (lower figure) as a function of time. The initial configurations were randomly chosen. The fluctuation is large near critical temperature $kT_C/J \approx 2.269$.

35
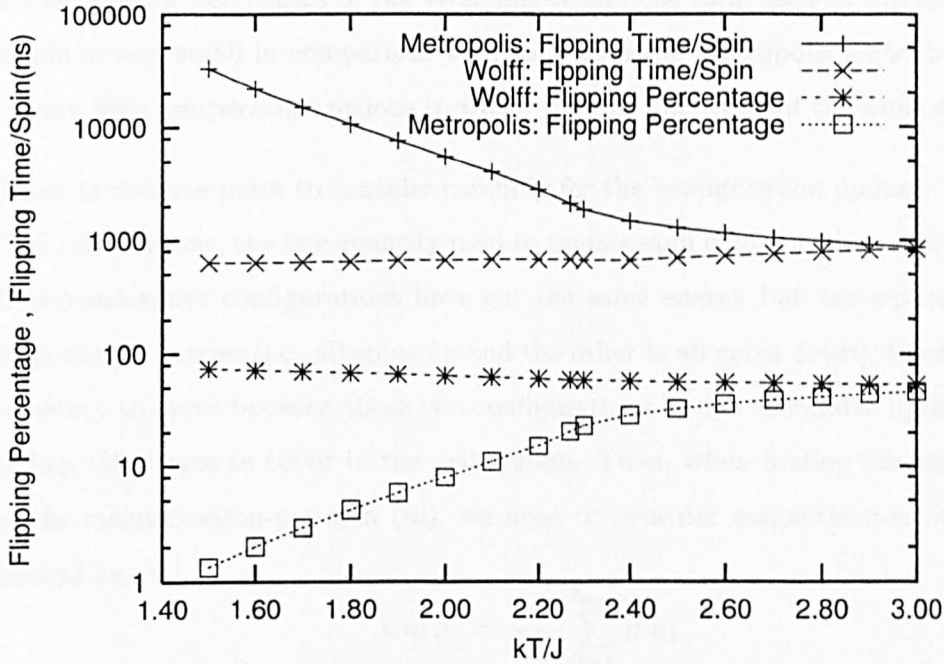
Figure 3.4: (upper pairs) The time (in nanosecond) used to successfully update one spin and (lower pairs) the ratio of flipping a spin (in %) for 128×128 Ising model between the Wolff and the Metropolis algorithms. Lines are used to guide the eyes.

From figure (3.4), we can see that the flipping percentage in the Metropolis algorithm in low temperature phase ($T < T_C$) is extremely small. This is because the Metropolis tries to update each spin individually. In a ferromagnetic phase, all spins tend to align into a same direction. To flip one spin to an opposite direction causes large energy move and this is not preferable. However, in the Wolff algorithm, the probability of adding spins into group $P_{add} = 1 - \exp(-2\beta J_{ij})$ is very high; thus, many spins with the same direction are grouped and flipped together. This makes the flipping percentage very high. On the other hand, for higher temperatures, the Metropolis gives a higher percentage because now the thermal energy is high enough to compensate any high energy required for the flipping. The Metropolis percentage is still lower than that of the Wolff algorithm.

In addition, in terms of c.p.u. time, it is very clear from the figure that with the

36

higher flipping percentage of the Wolff algorithm, the time used to successfully flip a spin is very small in comparison with that from the Metropolis algorithm except in very high temperature regions in which it turns out to be of the same size.

There is also one point to consider carefully for the configuration update. In Monte Carlo simulations, the key quantity used to update spin configurations is the energy. If two successive configurations have got the same energy but are separated by a huge energy barrier (i.e. all spins up and the other is all spins down), there is still a tendency to move between those two configurations in one successive update which in fact takes ages to occur in the real system. Then, when finding the expectation of the magnetisation-per-spin (m), we need to consider magnetisation magnitude instead i.e.

$$<m> = \frac{1}{t_{max}} \sum_{t=1}^{t_{max}} |m_t| \qquad (3.22)$$

Integrated Correlation Time

The correlation time represents correlation among the data arising from dependencies. To choose carefully the algorithm for our simulations, we need to consider the (integrated) correlation time given by both the Metropolis and the Wolff algorithm i.e. in figure (3.5).

However, as in the Wolff algorithm, a group of spins is flipped together; thus, one needs to be careful about the unit of time used in measuring the observables. For example, if we define a unit time in the Metropolis algorithm as one attempt to flip a spin per site, and we want to compare the correlation time between these two algorithms, we need consider them on the same time scale. This can be done as the following way.

In the Metropolis simulation, we record observables when number of attempts to flip spins is equal to N (the number of spins in the system). This time is defined as
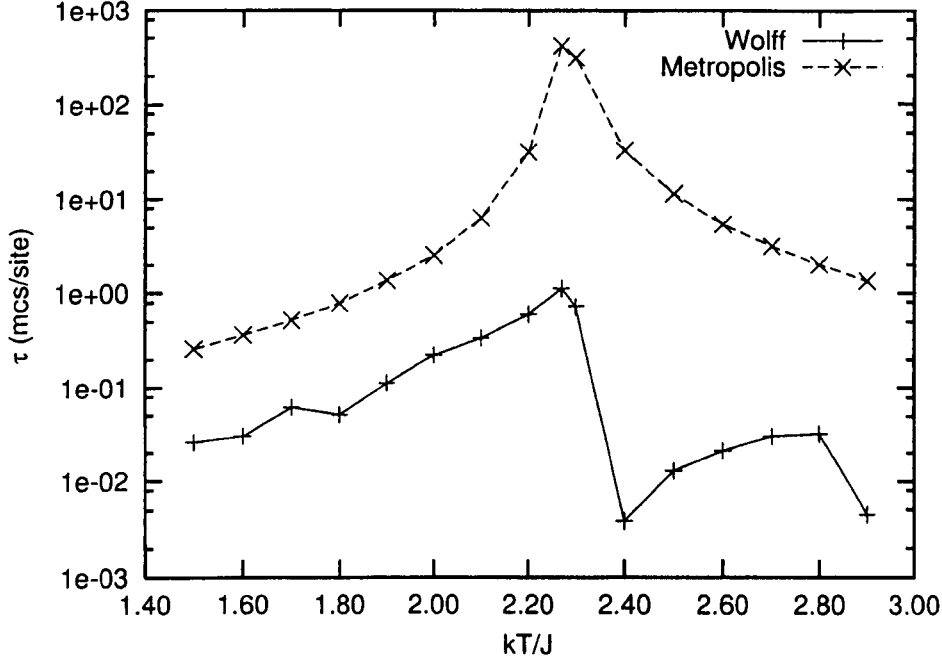
Figure 3.5: The integrated correlation time τ for $(2D)$ 128 × 128 Ising spins of the Metropolis and the Wolff algorithms after mapping onto the same time scale (see text). Lines are used to guide the eyes. For all temperatures, 2000 configurations are discarded and use 10^5 configurations to find τ.

1 mcs/site. However, in the Wolff simulation, we can measure the observables only after at least a group of spins is flipped. Moreover, this group can be very small to contain only 1 site at a very high temperature, or it can be very big to contain all sites at a very low temperature. Then, in the Wolff simulation, we let groups of spins to be flipped and measure one observable only after the number of spins in the flipped clusters (groups) exceed or are equal to N. In this way the time interval between two successive observables (in a unit of 1 site flipping) is approximately

$$\delta t \equiv \frac{i \times (\text{average cluster size})}{N}, \tag{3.23}$$

where i is the smallest integer such that $i \times$ (average cluster size) $\geq N$. Next, we need to convert this 'successful flipping time' to 'attempt to flip time' by using eq. (3.21). By this way, we can convert the Wolff time to Metropolis time. Then, to

map the Wolff correlation time onto the Metropolis time scale, we multiply τ_{wolff} by the Wolff time in Metropolis unit.

By investigating the figure (3.5), we notice that close to the interesting critical region where critical slowing down takes place (for instance, $k_BT_C/J \simeq 2.269$ for $2D$ Ising model), the Wolff algorithm dramatically cuts down the correlation time. One of the reasons is that the Wolff algorithm updates many spins at the same time instead of the individual updating of the Metropolis algorithm. This is a way to push the system far away from the previous state. As a result, this brings less correlation. So, by comparing both algorithms in terms of spin updating time and correlation time, we use the Wolff algorithm for all our Ising simulations.

Critical Temperatures and Critical Exponents

To estimate T_C for each film, firstly, we need to roughly locate the critical regions. So, for each system with layer size $L \times L$ and thickness l, we perform series of short simulations using 5000 configurations to make the average for temperatures kT/J vary from 1.00 to 11.00 with a step of 0.10. In each simulation, 2000 configurations are discarded for equilibration. Then, we look for the critical region where the susceptibilities have peaks or the magnetisation curves have maximum gradients e.g. figure (3.6).

From the figure, the temperature where the the magnetisation curves have maximum gradient increases with increasing number of layers. Also, the peaks of the magnetic susceptibilities show the same trend for all our lattice structures (SC, FCC, and BCC).

Next, we define the $k_BT_0(L,l)/J$ as the temperature at the centre of the critical region. In addition to the temperature that the magnetisation curve have maximum gradient or the susceptibility shows its peak, we can also roughly locate the critical
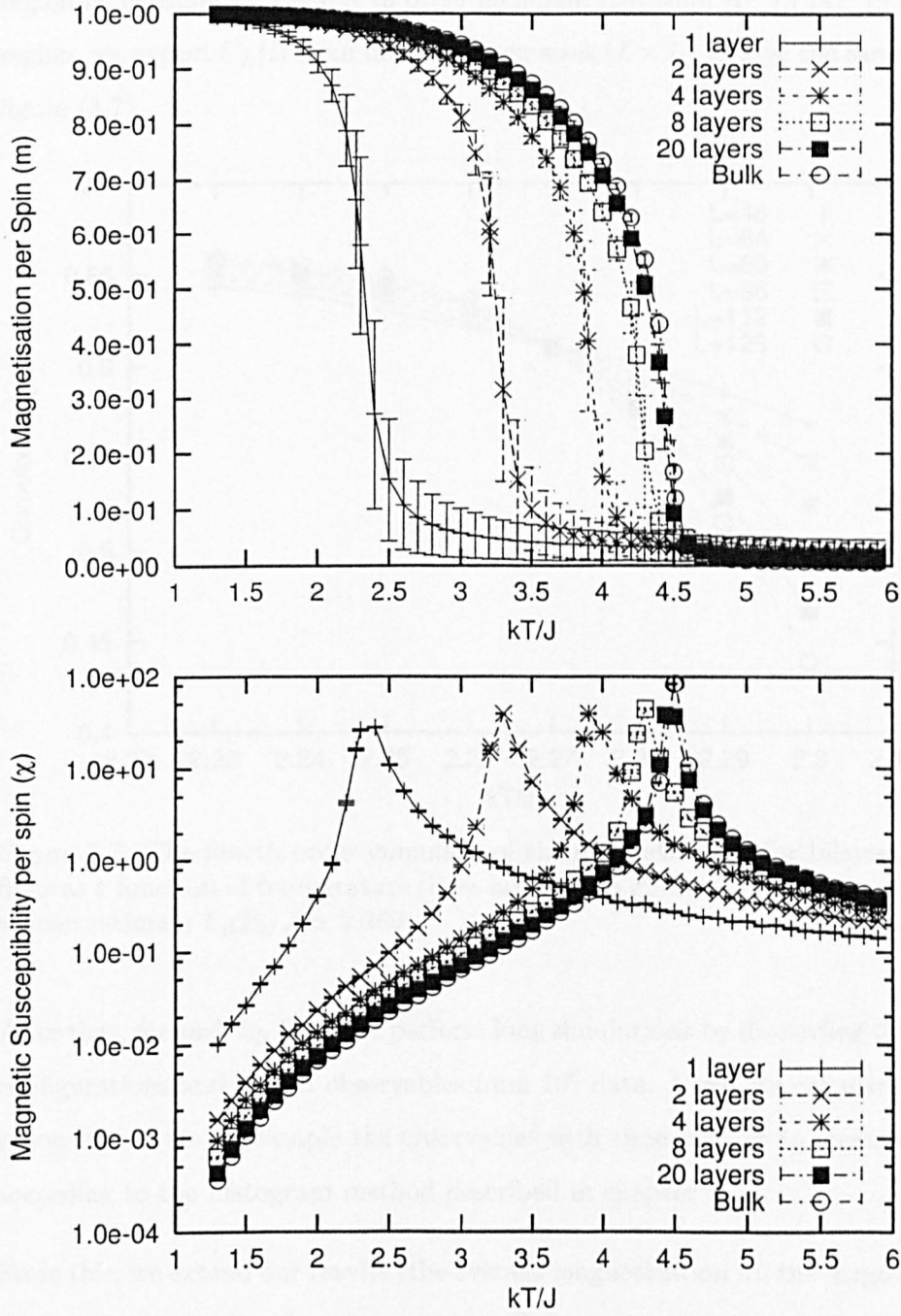
Figure 3.6: Magnetisation(upper) and magnetic susceptibility(lower) for $48 \times 48 \times l$ Ising SC thin-films ($l \equiv$ number of layers) and $48 \times 48 \times 48$ SC Ising bulk system as a function of temperature (lines are used to guide the eyes). For increasing number of layers, $k_B T_0/J$ shifts from the 2D value ($k_B T_C/J \approx 2.269$ [10]) to the 3D value ($k_B T_C/J \approx 4.511$ [16]).

region by considering the fourth order cumulant [24] from eq. (3.14). In the critical region, we expect $U_L(l)$ from different layer sizes ($L \times L$) to give the same $U^*(l)$ e.g. figure (3.7).
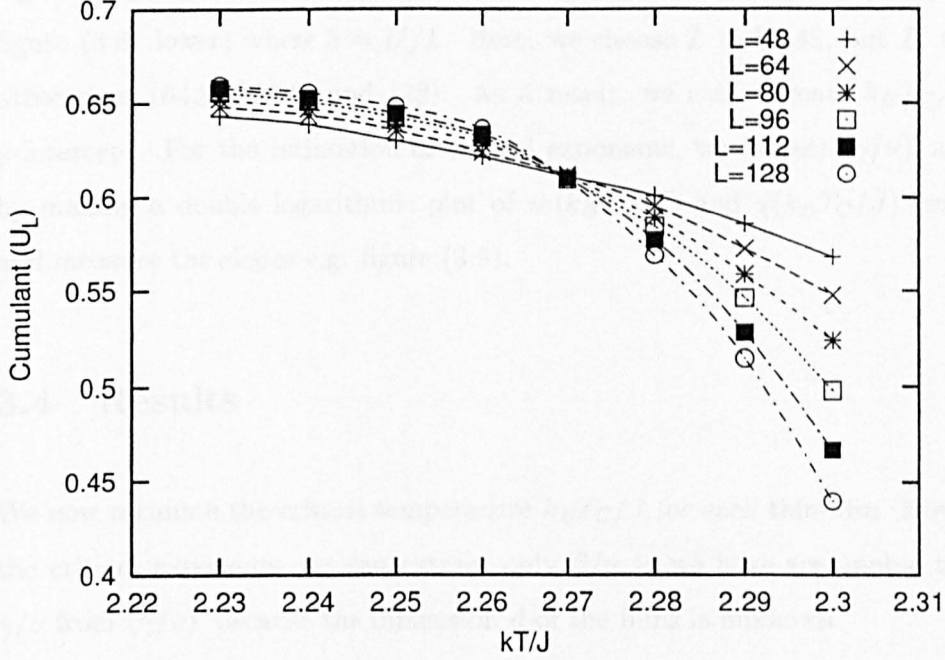
Figure 3.7: The fourth order cumulant of the magnetization for bilayer Ising BCC films as a function of temperature (lines are used to guide the eyes). From the figure, we can estimate $k_B T_0 / J \simeq 2.269$

After that, for each $k_B T_0 / J$, we perform long simulations by discarding the first 2000 configurations and record observables from 10^6 data. Next, we calculate the correlation time τ and re-sample the observables with time step 2τ to create histograms according to the histogram method described in chapter 2.

From this, we extend our results (the average magnetisation m, the magnetic susceptibility χ, and the fourth order cumulant U_L) to temperatures nearby $k_B T_0(L,l)/J$ with temperature step as $k_B T/J = 10^{-5}$. As a result, we can locate the critical temperature for each film thickness l by again looking at the intersection of U_L on a very fine scale.

41

At the critical temperature, for a particular film thickness l, the $U_L(l)$ curves should cross at the same temperature. However, for finite systems, all U_L curves may not cross at the same point (e.g. [35]). So, we need to plot $k_B T_C/J$ from each pair of U_L and $U_{L'}$ against $(\ln b)^{-1}$ and extrapolate the results for $(\ln b)^{-1} \to 0$ [24] e.g. figure (3.8: lower) where $b = L'/L$. Here, we choose L to be 48, but L' to be any other sizes (64,80,96,112 and 128). As a result, we can estimate $k_B T_C/J$ at the y-intercept. For the estimation of critical exponents, we extract $(\gamma/\nu)'$ and (β/ν) by making a double logarithmic plot of $m(k_B T_C/J)$ and $\chi(k_B T_C/J)$ versus $\log L$ and measure the slopes e.g. figure (3.9).

3.4   Results

We now estimate the critical temperature $k_B T_C/J$ for each thin-film. However, for the critical exponents, we can extract only β/ν as we have are unable to extract γ/ν from $(\gamma/\nu)'$ because the dimension d of the films is unknown.

Next, we check if the seed numbers of the random number generator have any effects on our results. So, for each system, we run each simulation twice by using different seed numbers generated randomly from computer clock, and we have found that the seed numbers do not affect the results significantly as the differences are very small (less than 1%).

Results of critical temperatures and critical exponents are listed in table (3.1) and plotted in figure (3.10). The results listed are calculated from the simulations of those 2 different seed numbers via formulae

$$Q = \left[\frac{Q_1}{(\Delta Q_1)^2} + \frac{Q_2}{(\Delta Q_2)^2} \right] (\Delta Q)^2, \tag{3.24}$$

$$\frac{1}{(\Delta Q)^2} = \frac{1}{(\Delta Q_1)^2} + \frac{1}{(\Delta Q_2)^2}, \tag{3.25}$$

where Q is the observable we average from Q_1 (seed 1) and Q_2 (seed 2).
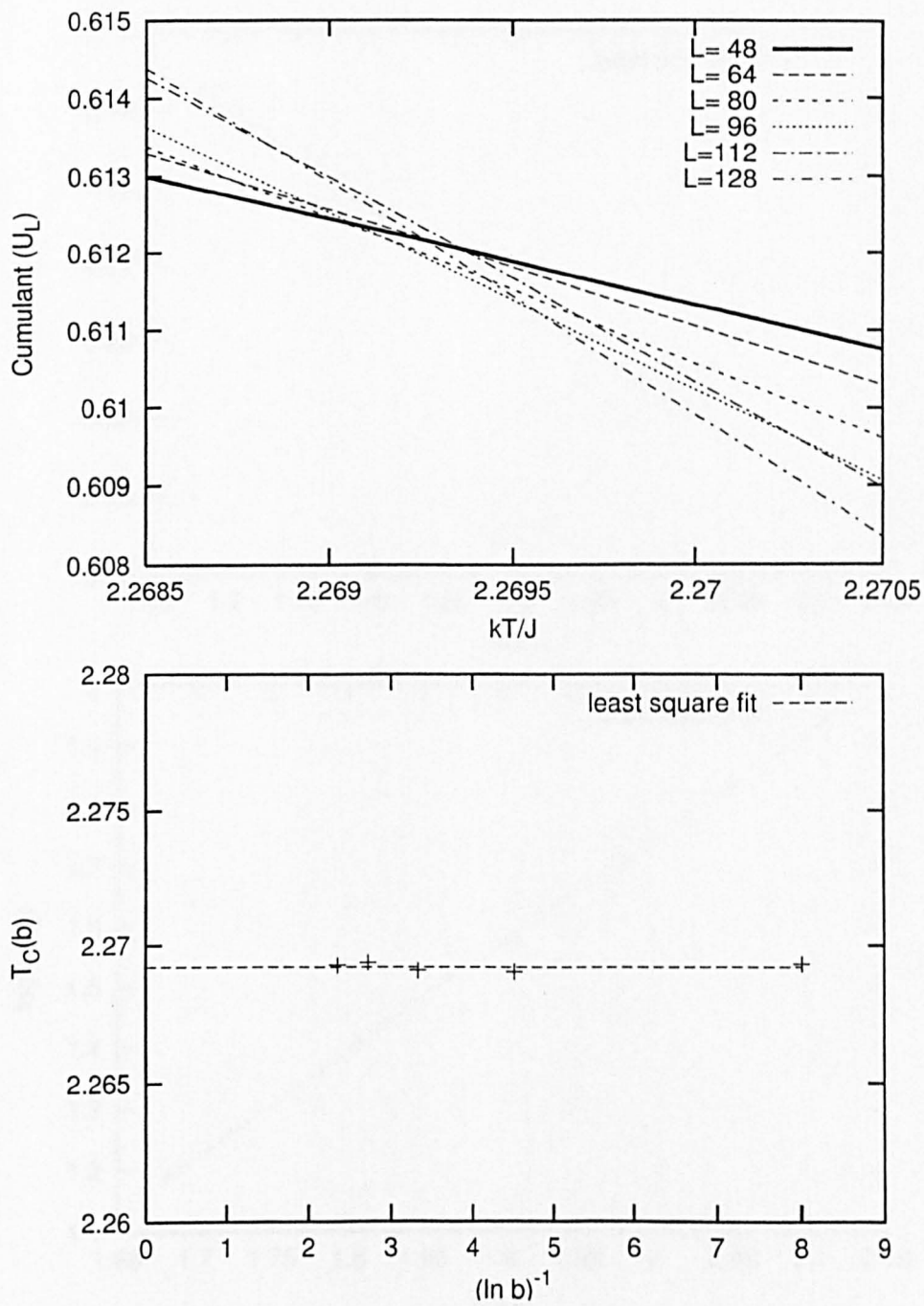
Figure 3.8: (upper): Intersection of U_L curves extrapolated from histogram method performed at $kT_0/J = 2.269$. (lower): Estimation of T_C plotted vs inverse logarithm of the scale factor $b = L'/L$. In the figure, $L = 48$ and $L' = 64, \cdots, 128$. The line is drawn from least square fitting giving $T_C = 2.2688 \pm 3.0 \times 10^{-4}$. The results are taken from those for bilayer Ising BCC films.

43
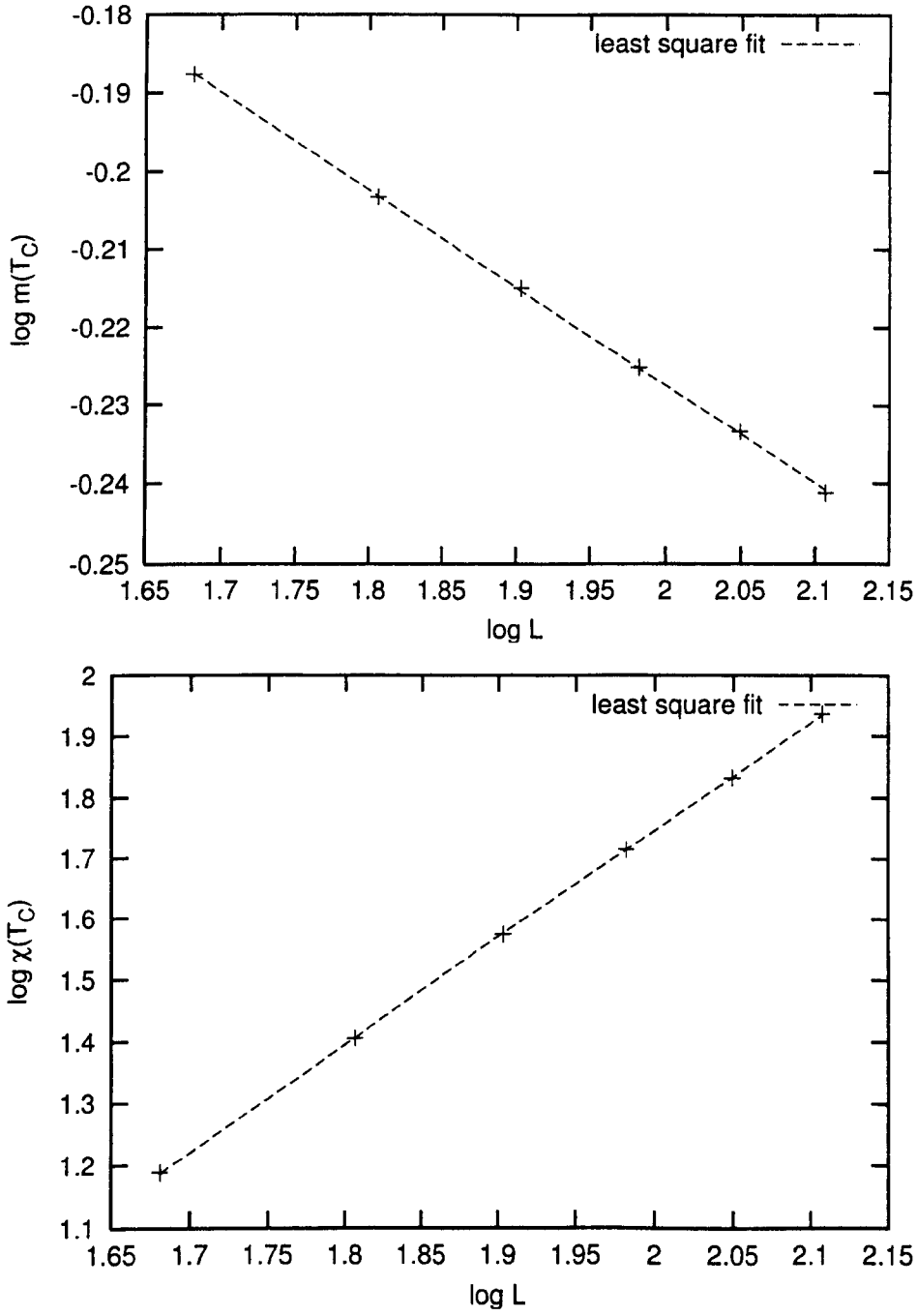
Figure 3.9: Double logarithmic plot of the magnetisation (upper) and magnetic susceptibility (lower) at T_C vs lattice size L for monolayer Ising FCC films. The lines are drawn from linear curve fitting using least square method giving $\beta/\nu = 0.1252 \pm 7.2 \times 10^{-4}$ and $\gamma/\nu = 1.753 \pm 5.3 \times 10^{-3}$

44

	#layers	$k_B T_C / J$	β/ν	$(\gamma/\nu)'$
	2D(Exact)	≈ 2.2692	0.1250	1.7500
	1	$2.26903 \pm 6.3 \times 10^{-5}$	$0.1227 \pm 4.0 \times 10^{-4}$	$1.754 \pm 1.8 \times 10^{-3}$
	2	$3.20770 \pm 1.8 \times 10^{-4}$	$0.1220 \pm 1.0 \times 10^{-3}$	$1.742 \pm 5.0 \times 10^{-3}$
	4	$3.87060 \pm 1.5 \times 10^{-4}$	$0.1285 \pm 9.1 \times 10^{-4}$	$1.734 \pm 6.9 \times 10^{-3}$
	6	$4.11820 \pm 1.0 \times 10^{-4}$	$0.1340 \pm 5.4 \times 10^{-4}$	$1.730 \pm 3.8 \times 10^{-3}$
sc	8	$4.24070 \pm 1.6 \times 10^{-4}$	$0.1350 \pm 1.4 \times 10^{-3}$	$1.710 \pm 8.6 \times 10^{-2}$
	10	$4.31180 \pm 1.5 \times 10^{-4}$	$0.1500 \pm 1.9 \times 10^{-3}$	$1.710 \pm 1.1 \times 10^{-2}$
	15	$4.39947 \pm 5.4 \times 10^{-5}$	$0.1580 \pm 1.3 \times 10^{-3}$	$1.680 \pm 1.1 \times 10^{-2}$
	20	$4.43830 \pm 1.8 \times 10^{-4}$	$0.1690 \pm 1.5 \times 10^{-3}$	$1.640 \pm 1.5 \times 10^{-2}$
	Bulk*	$4.51110 \pm 1.4 \times 10^{-4}$	$0.5130 \pm 8.3 \times 10^{-3}$	$0.950 \pm 1.0 \times 10^{-2}$
	Bulk	$4.51162 \pm 6.0 \times 10^{-5}$	$0.5260 \pm 5.4 \times 10^{-3}$	$0.970 \pm 4.9 \times 10^{-2}$
	2	$2.26918 \pm 4.3 \times 10^{-6}$	$0.1172 \pm 4.2 \times 10^{-4}$	$1.755 \pm 4.2 \times 10^{-3}$
	4	$4.29450 \pm 2.8 \times 10^{-4}$	$0.1230 \pm 6.2 \times 10^{-4}$	$1.763 \pm 4.4 \times 10^{-3}$
	6	$5.10170 \pm 5.1 \times 10^{-4}$	$0.1310 \pm 1.2 \times 10^{-3}$	$1.745 \pm 6.0 \times 10^{-3}$
	8	$5.50000 \pm 3.6 \times 10^{-4}$	$0.1280 \pm 1.3 \times 10^{-3}$	$1.736 \pm 7.3 \times 10^{-3}$
bcc	10	$5.72950 \pm 2.4 \times 10^{-4}$	$0.1398 \pm 8.5 \times 10^{-4}$	$1.743 \pm 4.2 \times 10^{-3}$
	15	$6.00700 \pm 5.1 \times 10^{-3}$	$0.1480 \pm 2.1 \times 10^{-3}$	$1.700 \pm 1.2 \times 10^{-2}$
	20	$6.12950 \pm 4.4 \times 10^{-4}$	$0.1590 \pm 2.5 \times 10^{-3}$	$1.650 \pm 1.7 \times 10^{-2}$
	Bulk*	$6.35550 \pm 1.9 \times 10^{-4}$	$0.5550 \pm 6.7 \times 10^{-3}$	$0.916 \pm 9.4 \times 10^{-3}$
	Bulk	$6.35530 \pm 1.5 \times 10^{-4}$	$0.5110 \pm 3.9 \times 10^{-3}$	$0.984 \pm 4.6 \times 10^{-3}$
	1	$2.26910 \pm 1.4 \times 10^{-4}$	$0.1243 \pm 4.3 \times 10^{-4}$	$1.750 \pm 2.4 \times 10^{-3}$
	2	$5.24110 \pm 1.8 \times 10^{-4}$	$0.1196 \pm 6.2 \times 10^{-4}$	$1.757 \pm 3.9 \times 10^{-3}$
	4	$7.57070 \pm 2.8 \times 10^{-4}$	$0.1253 \pm 7.6 \times 10^{-4}$	$1.751 \pm 2.9 \times 10^{-3}$
	6	$8.44190 \pm 4.6 \times 10^{-4}$	$0.1256 \pm 1.2 \times 10^{-4}$	$1.745 \pm 5.8 \times 10^{-3}$
fcc	8	$8.86570 \pm 4.1 \times 10^{-4}$	$0.1210 \pm 1.8 \times 10^{-3}$	$1.710 \pm 1.3 \times 10^{-2}$
	10	$9.11170 \pm 8.3 \times 10^{-4}$	$0.1410 \pm 1.3 \times 10^{-3}$	$1.720 \pm 1.0 \times 10^{-2}$
	15	$9.40510 \pm 3.0 \times 10^{-4}$	$0.1520 \pm 1.7 \times 10^{-3}$	$1.690 \pm 1.0 \times 10^{-2}$
	20	$9.53700 \pm 1.3 \times 10^{-3}$	$0.1790 \pm 3.8 \times 10^{-3}$	$1.680 \pm 1.9 \times 10^{-2}$
	Bulk*	$9.77300 \pm 2.5 \times 10^{-4}$	$0.5320 \pm 5.0 \times 10^{-3}$	$0.946 \pm 5.1 \times 10^{-3}$
	Bulk	$9.77350 \pm 1.6 \times 10^{-4}$	$0.4890 \pm 4.0 \times 10^{-3}$	$0.986 \pm 3.6 \times 10^{-3}$

Table 3.1: Ising film results. Bulk* refers to the bulk $3D$ system which has periodic boundary conditions along xy directions, but has a free boundary along z direction

3.5 Discussion and Conclusion

For a monolayer system (bilayer in BCC films), our results agree very well with the exact Ising $2D$ results. Then, when we increase the number of layers, the critical temperature $T_C(l)$ moves towards the bulk $3D$ value. This can be explained by looking at the lattice structure itself. For example, for the SC structure, in $2D$, the number of nearest neighbours is 4 whereas it is 6 in $3D$. Then, the average exchange energy per site is stronger with increasing number of layers. Thus, to change from a ferromagnetic phase to a paramagnetic phase, the system needs higher thermal energy to compensate the stronger exchange energy. Also, for the same reason, for the same number of layers, $T_C^{SC} < T_C^{BCC} < T_C^{FCC}$. Similarly, the bulk $3D$ T_C's from simulations using periodic-boundary surface condition are higher than those using the free-boundary surface condition except in the case of bulk *BCC* results where the results seem to agree within their error bars. This may be caused by the fact that the number of sites in bulk BCC simulations is $L^3/4$ which is less than SC and FCC with the same L making the BCC system more sensitive to statistical error.

For the critical exponent results $(\gamma/\nu)'$ and β/ν, we have found a movement from $2D$ values to $3D$ values for both of them as the film thicknesses are increased. However, since we cannot extract the film dimension d from our results, we cannot extract γ/ν out of $(\gamma/\nu)'$. The way $(\gamma/\nu)' \equiv \gamma/\nu + 2 - d$ decreases when increasing layers means that d increases faster than γ/ν which seems to be reasonable as for a $2D$ to a bulk system, d increases from 2 to 3 but γ/ν increases only a little from 1.75 to 1.98. Moreover, if we consider the summation of $(\gamma/\nu)' + 2(\beta/\nu)$ as

$$
\begin{aligned}
\left(\frac{\gamma}{\nu}\right)' + 2\frac{\beta}{\nu} &\equiv \frac{\gamma}{\nu} + 2 - d + 2\frac{\beta}{\nu} \\
&= 2 - d + d = 2,
\end{aligned}
\tag{3.26}
$$

where we use the relation $\gamma/\nu + 2\beta/\nu = d$ [26], we should get value of 2 when
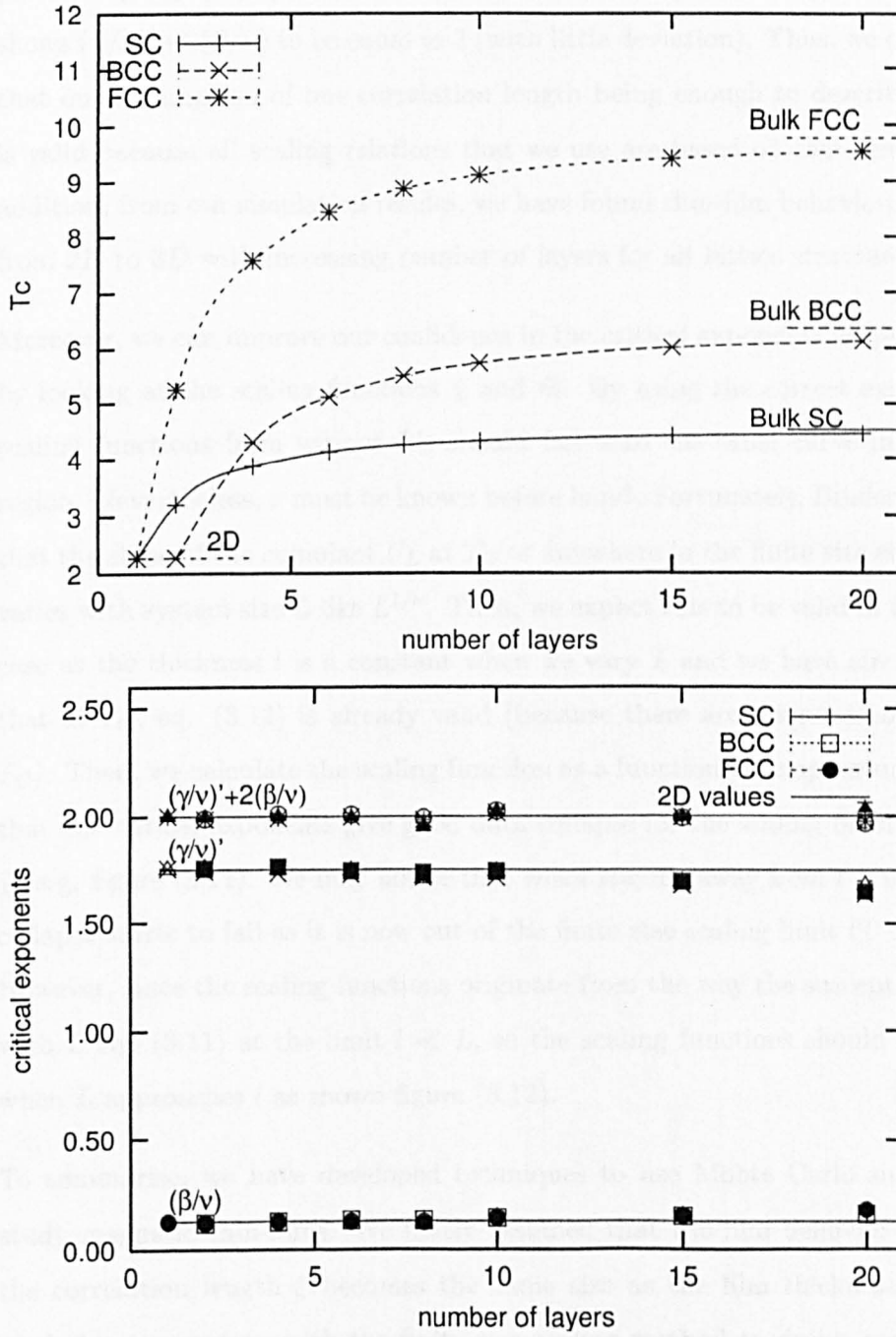
Figure 3.10: (upper) Critical temperature T_C as a function of film thickness for Ising thin-films. The bottommost line is the T_C in $2D$. The straight line above each curve is for the bulk values. (lower) Critical exponents $(\gamma/\nu)'$, β/ν and $(\gamma/\nu)' + 2(\beta/\nu)$ vs thicknesses for Ising thin-films. The lines are for $2D$ results.

performing $(\gamma/\nu)' + 2(\beta/\nu)$ which are extracted from the simulations. Figure (3.10) shows $(\gamma/\nu)' + 2(\beta/\nu)$ to be equal to 2 (with little deviation). Thus, we can conclude that our assumption of one correlation length being enough to describe thin-films is valid because all scaling relations that we use are based on this assumption. In addition, from our simulation results, we have found thin-film behaviour developing from $2D$ to $3D$ with increasing number of layers for all lattice structures.

Moreover, we can improve our confidence in the critical exponents we just extracted by looking at the scaling functions $\widetilde{\chi}$ and $\widetilde{m}$. By using the correct exponents, the scaling functions from various L's should fall onto the same curve in the critical region. Nevertheless, ν must be known before hand. Fortunately, Binder [24] showed that the slope of the cumulant U_L at T_C or anywhere in the finite size scaling region varies with system size L like $L^{1/\nu}$. Then, we expect this to be valid in the thin-film case as the thickness l is a constant when we vary L and we have already checked that at T_C, eq. (3.14) is already valid (because there are intersections of U_L's at T_C). Then, we calculate the scaling function as a function of temperature and found that our critical exponents give good data collapse for the scaling functions ($\widetilde{m}$ and $\widetilde{\chi}$) e.g. figure (3.11). We may notice that when staying away from $t = 0$ ($x = 0$) the collapse starts to fail as it is now out of the finite size scaling limit (T close to T_C). However, since the scaling functions originate from the way the susceptibility scales with L eq. (3.11) at the limit $l \ll L$, so the scaling functions should not collapse when L approaches l as shown figure (3.12).

To summarise, we have developed techniques to use Monte Carlo simulations to study magnetic thin-films. We firstly assumed that the film behavior starts when the correlation length ξ becomes the same size as the film thickness. Then, we used this assumption with the finite size scaling method to derive expressions for the extraction of critical temperatures T_C and critical exponents. Next, we checked our assumption by performing a series of simulations for SC, BCC and FCC films.
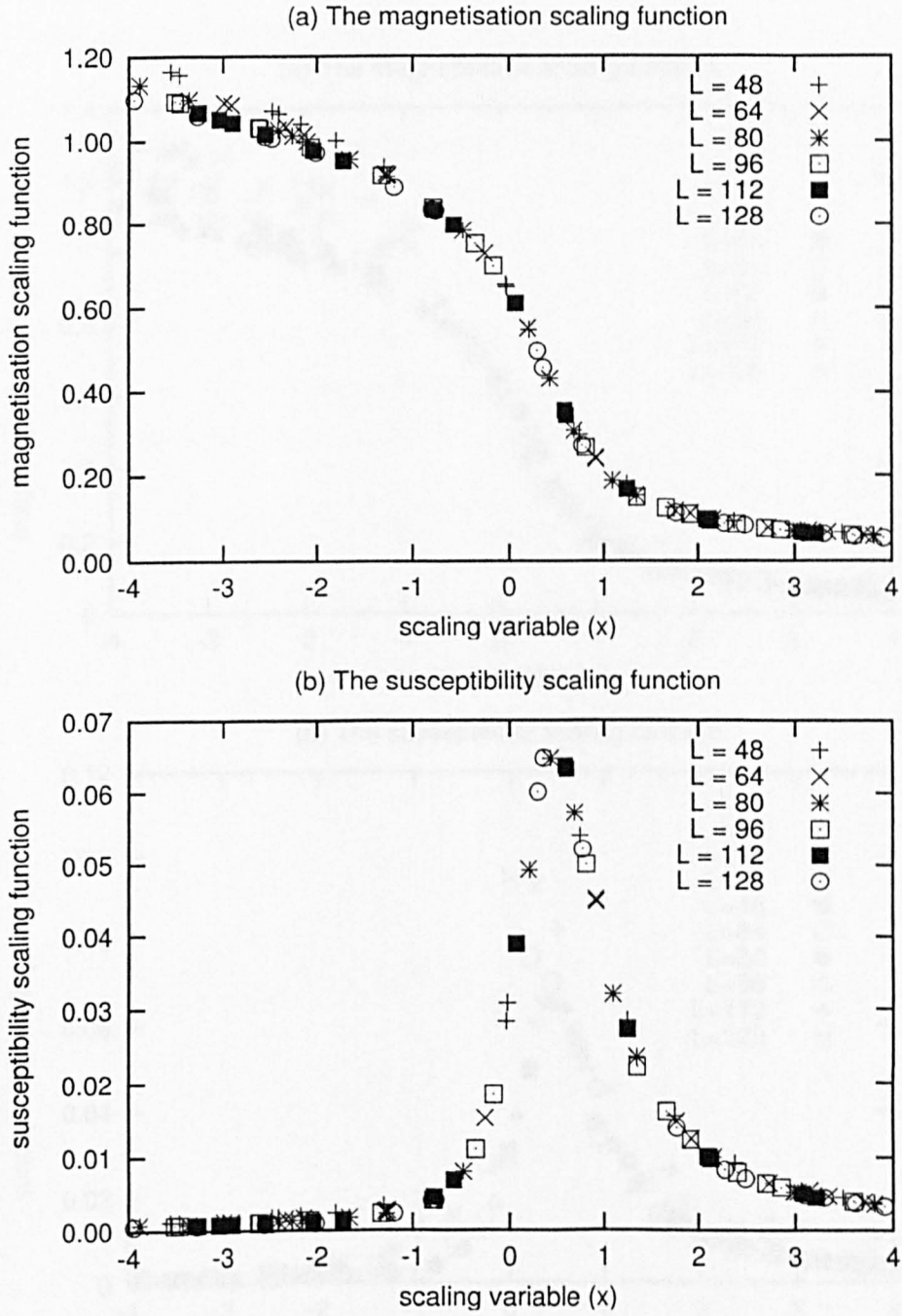
Figure 3.11: Data collapse of the magnetisation (Upper) and the susceptibility (Lower) scaling functions for 8 layers SC Ising-films as a function of scaling variable ($x = L^{1/\nu}t$). In this collapse, we use $(\gamma/\nu)' = 1.713094, \beta/\nu = 0.134686$, and $T_C = 4.240669$ which are extracted from finite size scaling method.

49
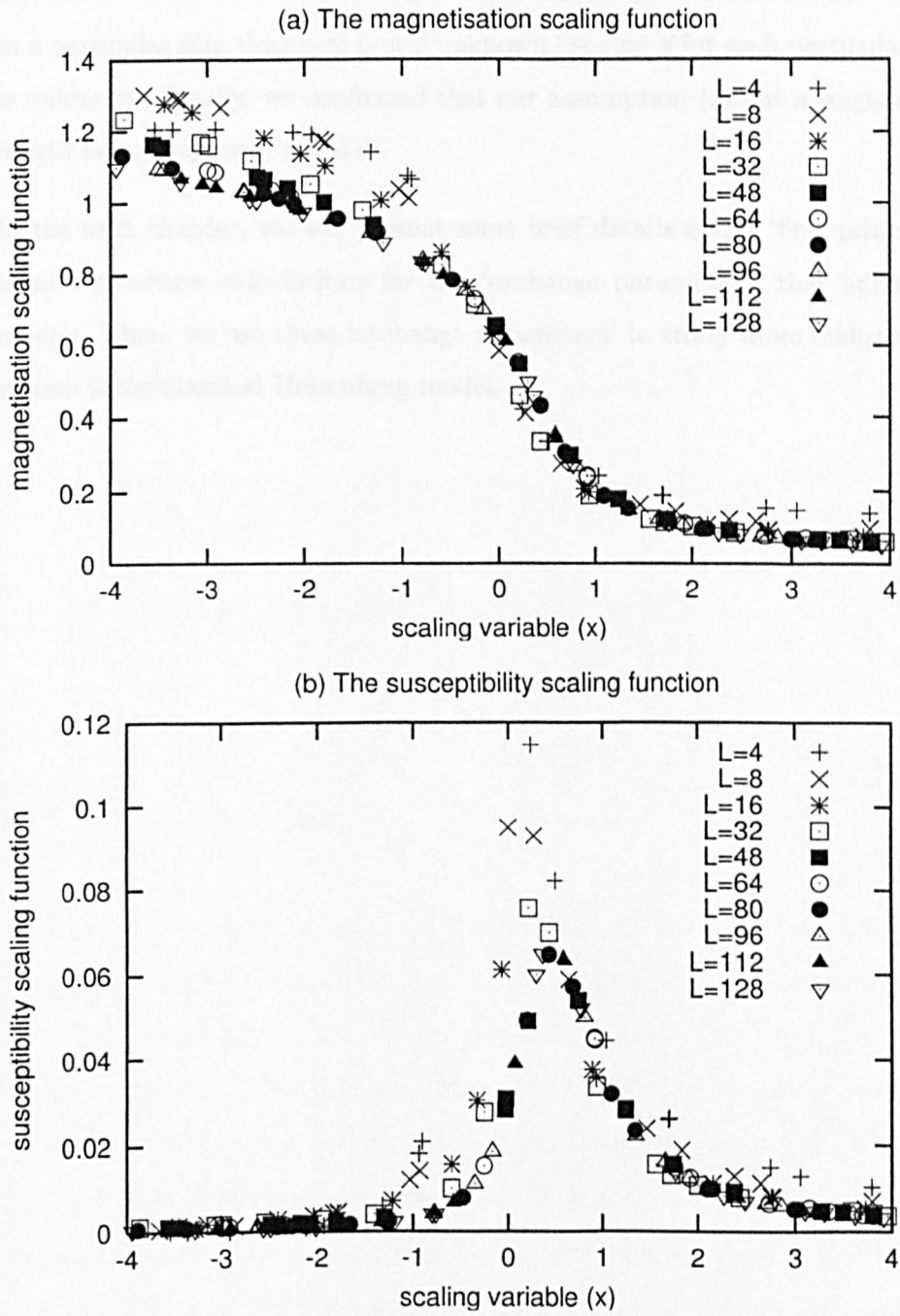
Figure 3.12: Same as figure (3.11), but include L = 4,8,16 and 32.

From our results, we noticed that the critical temperatures increased from $2D$ to $3D$ values. Also, we found the same behaviour for β/ν. However, the value of γ/ν in a particular film thickness is still unknown because d for each particular thickness is unknown. Finally, we confirmed that our assumption (about a single correlation length being required) is valid.

In the next chapter, we will present some brief details about 'first principles' electronics structure calculations for the 'exchange parameters' that appear in spin models. Then, we use these 'exchange parameters' to study more realistic magnetic system using classical Heisenberg model.

Chapter 4

'First Principles' Theory of Electronic Structure for 'Exchange Interaction'

4.1 Introduction

We begin this chapter with some brief details about the calculations of the 'exchange parameters' of layered metallic materials from the 'first principles' electronic structure calculations within a 'local moment' picture (e.g. [36]-[40]). From calculations in which a mean-field approximation is used, the 'exchange parameters' are extracted [39, 40] which we put in a classical Heisenberg model [41] and treat with our Monte Carlo simulations. Next, we note that in contradiction to the Mermin-Wagner theorem [42], some experiments for ultra-thin films (e.g. [43, 44]) reveal the presence of long-range ferromagnetic order at low temperatures implying that, phenomenologically, anisotropic effects should be included in models of these systems. Then, we close this chapter with an approximation of anisotropic energy extracted

from 'first principles' electronic structure calculations (e.g. [45, 46]).

4.2   Spin Density Functional Theory

The description of a metallic system is a many body problem involving the interaction of many electrons which is unsolvable even numerically. Thus, one needs to transform the problem into an effective one-electron problem instead i.e. the energy $E[n(\vec{r})]$ of an interacting electron system in the presence of an external potential $\nu^{ext}(\vec{r})$ needs to be expressed in terms of the charge density of the system $n(\vec{r})$.

This idea was originated from Thomas [47] and Fermi [48], and later was developed by Hohenberg and Kohn [49] who proposed that the electron density $n(\vec{r})$ is uniquely determined by the external potential $\nu^{ext}(\vec{r})$, and the ground state density $n(\vec{r})$ in the presence of $\nu^{ext}(\vec{r})$ gives the ground state energy. Then, Kohn and Sham [50] used the variational principle to minimise the ground state energy functional to derive single-electron Schrödinger equations

$$\left[-\frac{\hbar^2}{2m}\nabla^2 + \nu^{eff}(\vec{r}) \right] \phi_i(\vec{r}) = \varepsilon_i \phi_i(\vec{r}), \qquad (4.1)$$

of noninteracting electrons system moving in an effective potential

$$\nu^{eff}(\vec{r}) = \nu^{ext}(\vec{r}) + e^2 \int \frac{n(\vec{r}')}{|\vec{r} - \vec{r}'|} d\vec{r}' + \frac{\delta E^{xc}}{\delta n(\vec{r})}, \qquad (4.2)$$

which describes the external, the Hartree and the exchange correlation potential. The external term contains both electron-ion and external field potential, E^{xc} is usually approximated from the Local Density Approximation (LDA) [50].

However, to extend this density functional theory to magnetic systems, we must consider systems in magnetic fields $\vec{B}(\vec{r})$ in which the spin index α of one-electron wave function and the spin (magnetisation) density $\vec{m}(\vec{r})$ become relevant. Then, instead of being a single variable, there are now two separate charge density functions

for spin up $n_\uparrow(\vec{r})$ and spin down $n_\downarrow(\vec{r})$ electrons which define the total charge density

$$n(\vec{r}) = n_\uparrow(\vec{r}) + n_\downarrow(\vec{r}). \tag{4.3}$$

Actually, the Kohn-Sham argument is still valid in this case, but the minimisation needs to be with respect to variations in both the charge and spin density subjected to the constraint that the number of particles is a constant (e.g. [51]-[53]). Then, this leads to the Schrödinger equations

$$\left(-\frac{\hbar^2}{2m}\nabla^2 \mathbf{I} + \nu^{eff}(\vec{r})\mathbf{I} + \mu_B \vec{\sigma} \cdot \vec{\mathbf{B}}^{eff}(\vec{r})\right)\phi_i(\vec{r}) = \varepsilon_i\phi_i(\vec{r}), \tag{4.4}$$

where

$$\nu^{eff}(\vec{r}) = \nu^{ext}(\vec{r}) + e^2 \int \frac{n(\vec{r}')}{|\vec{r} - \vec{r}'|}d\vec{r}' + \frac{\delta E^{xc}[n, \vec{\mathbf{m}}]}{\delta n(\vec{r})} \tag{4.5}$$

$$\vec{\mathbf{B}}^{eff} = \vec{\mathbf{B}}^{ext} + \frac{1}{\mu_B}\frac{\delta E^{xc}[n, \vec{\mathbf{m}}]}{\delta \vec{\mathbf{m}}(\vec{r})}, \tag{4.6}$$

where $\vec{\sigma}$ is the Pauli matrices, $\mathbf{I}$ is 2×2 identity matrix and the ϕ_i are two-component spinors containing $\phi_\uparrow$ and $\phi_\downarrow$. So, the ground state energy can be written as

$$\begin{aligned} E[n, \vec{\mathbf{m}}] &= \sum_i \varepsilon_i - \frac{e^2}{2} \int\int \frac{n(\vec{r})n(\vec{r}')}{|\vec{r} - \vec{r}'|}d\vec{r}d\vec{r}' \\ &\quad - \int \frac{\delta E^{xc}}{\delta n(\vec{r})}n(\vec{r})d\vec{r} - \int \frac{\delta E^{xc}}{\delta \vec{\mathbf{m}}(\vec{r})} \cdot \vec{\mathbf{m}}(\vec{r})d\vec{r} + E^{xc}(\vec{r}) \end{aligned} \tag{4.7}$$

where the exchange correlation energy $E^{xc} = \int \varepsilon^{xc}(n(\vec{r}), |\vec{\mathbf{m}}(\vec{r})|)n(\vec{r})d\vec{r}$ can be approximated from Local Density Approximation (e.g. von Barth and Hedin's version [51]).

However, to extend this problem to finite temperatures (pioneered by Mermin [54]), the Gibbs grand potential is considered instead of the ground state energy. Then, $n(\vec{r})$ and $\vec{\mathbf{m}}(\vec{r})$ are temperature dependent via the Fermi-Dirac distribution $f(\varepsilon) = [1 + \exp\beta(\varepsilon - \mu)]^{-1}$ as

$$n(\vec{r}) = \sum_i f(\varepsilon_i)\phi_i^*(\vec{r})\phi_i(\vec{r}), \tag{4.8}$$

$$\vec{\mathbf{m}}(\vec{r}) = \sum_i f(\varepsilon_i)\phi_i^*(\vec{r})\vec{\sigma}\phi_i(\vec{r}). \tag{4.9}$$

Then, at a given temperature T and chemical potential μ, the equilibrium particle density $n(\vec{r})$ and magnetisation $\vec{m}(\vec{r})$ give the minimum of the Gibbs grand potential Ω (e.g. [55])

$$
\begin{aligned}
\Omega[\mathbf{n}, \vec{m}] \;=\; & -\beta^{-1} \sum_{i=1}^{\infty} \ln[1 + \exp \beta(\mu - \varepsilon_i)] - \frac{1}{2} e^2 \int \int \frac{n(\vec{r}) n(\vec{r}')}{|\vec{r} - \vec{r}'|} \mathrm{d}\vec{r}\mathrm{d}\vec{r}' \\
& - \int \frac{\delta \Omega^{xc}}{\delta n(\vec{r})} n(\vec{r}) \mathrm{d}\vec{r} - \int \frac{\delta \Omega^{xc}}{\delta \vec{m}(\vec{r})} \vec{m}(\vec{r}) \mathrm{d}\vec{r} + \Omega^{xc}[n, \vec{m}],
\end{aligned} \tag{4.10}
$$

where $\Omega^{xc} \simeq E^{xc}$ is the exchange grand potential.

Now, it is possible to find the temperature T_C^{Stoner} where the magnetisation vanishes. However, this T_C is too high, and there is no moment above T_C because it is solved from local density approximation with the magnetisation in each unit cell pointing in the same direction. Then, a new improved theory is needed which should allow moments to vary from unit cell to unit cell. Also, the absence of magnetisation above T_C should be caused by the cancellation of moments in disordered pattern, not because of the absence of the moments. One successful view to look at this problem in finite temperature is the Disordered Local Moments picture [39, 40].

4.3   Disordered Local Moments

The Disordered Local Moment (DLM) [39, 40] is a theory used to describe a magnetic behaviour of transition metals at finite temperatures. The theory is based on the time differences between electron hopping from atom to atom and spin wave time period. Then, for a suitable time scale τ, the correlation of the spin orientations caused by the coming and outgoing electrons give nonzero magnetisation when averaged over time τ. This gives a 'local magnetic moment' to each site with a magnitude of

$$
\mu_i^\tau = \left| \int_{V_i} \mathrm{d}^3 \vec{r} \; \vec{m}_\tau(\vec{r}) \right|, \tag{4.11}
$$

55

where V_i is the volume at site i and $\vec{m}$ is the magnetisation density. For this time scale τ, the average of the magnetisation density $\hat{e}$ is given by

$$\hat{e}_i = \frac{\int_{V_i} d^3\vec{r} \; \vec{m}_\tau(\vec{r})}{\mid \int_{V_i} d^3\vec{r} \; \vec{m}_\tau(\vec{r}) \mid},$$ (4.12)

and the probability of finding the orientational configuration $\{\hat{e}\}$ is

$$P(\{\hat{e}_i\}) = \frac{1}{Z} \exp(-\beta\Omega(\{\hat{e}_i\})),$$ (4.13)

where the partition function $Z = \prod_j \int d\hat{e}_j \exp(-\beta\Omega(\{\hat{e}_i\}))$ and Ω is a 'generalised' grand potential describing the interacting electron system under the constraint that the local moments are oriented along the directions $\{\hat{e}\}$. However, the partition function in this form is not useful because Ω may be too complicated to achieve directly. A better way to proceed [39, 40] is to write

$$\Omega(\{\hat{e}_i\}) = H_0(\{\hat{e}_i\}) + (\Omega(\{\hat{e}_i\}) - H_0(\{\hat{e}_i\})),$$ (4.14)

where $H_0(\{\hat{e}_i\})$ is an arbitrary trial hamiltonian. Then, from the Feynman-Peierls' inequality [56], an upper bound to any free energy F is

$$F \leq F_1 = F_0 + <\Omega - H_0>_0,$$ (4.15)

with

$$F_0 = -k_B T \log Z_0,$$ (4.16)

where $Z_0 = \prod_j \int d\hat{e}_j \exp(-\beta H_0(\{\hat{e}_i\}))$ and the average $< \ldots >_0$ is with respect to $P_0(\{\hat{e}_i\}) = \frac{1}{Z_0} \exp(-\beta H_0(\{\hat{e}_i\}))$. A flexible form for choosing H_0 is to expand the trial hamiltonian in a series like

$$H_0 = \sum_i \omega_i^{(1)}(\hat{e}_i) + \frac{1}{2}\sum_{i,j} \omega_{i,j}^{(2)}(\hat{e}_i, \hat{e}_j) + \ldots,$$ (4.17)

where $\omega_i^{(1)}, \omega_{i,j}^{(2)}, \cdots$ are arbitrary functions of their variables. The condition used to determine $\omega_i^{(1)}, \omega_{i,j}^{(2)}, \cdots$ are [39]

$$\frac{\delta F_1}{\delta \omega_i^{(1)}(\hat{e}_i)} = 0, \quad \frac{\delta F_1}{\delta \omega_{i,j}^{(2)}(\hat{e}_i, \hat{e}_j)} = 0, \quad \ldots$$ (4.18)

56

However, if we take some approximation by keeping only single site terms, $\sum_i \omega_i^{(1)}(\hat{e}_i)$, we can use the mean-field choice for the trial hamiltonian H_0. By considering the trial hamiltonian

$$H_0 = -\sum_i \vec{h}_i \cdot \hat{e}_i, \tag{4.19}$$

F_1 can be determined by evaluating Z_0 in a local frame of reference where the z axis is oriented along $\vec{h}_i$ i.e.

$$Z_0 = \prod_i \int_0^{2\pi} d\varphi_i \int_0^\pi \sin\theta_i d\theta_i \exp(\beta h_i \cos\theta_i) = \prod_i \frac{4\pi}{\beta h_i} \sinh\beta h_i, \tag{4.20}$$

and the free energy F_0 becomes

$$F_0 = -\beta^{-1} \sum_i \ln\left(\frac{4\pi}{\beta h_i} \sinh\beta h_i\right), \tag{4.21}$$

and

$$<H_0>_0 = -\frac{\partial}{\partial\beta} \ln Z_0 = -\sum_i h_i m_i, \tag{4.22}$$

where the average magnetic moment $\vec{m}_i \equiv <\hat{e}_i> \equiv m_i \hat{h}_i$ is now Langevin function as

$$m_i = \coth\beta h_i - 1/\beta h_i \equiv L(\beta h_i). \tag{4.23}$$

So

$$F_1 = -\beta^{-1} \sum_i \ln\left(\frac{4\pi}{\beta h_i} \sinh\beta h_i\right) + \sum_i h_i m_i + <\Omega>_0. \tag{4.24}$$

Then, by minimising F_1 with respect to h_j ($\partial F_1/\partial h_j = 0$) , it can be obtained that

$$h_j = -\frac{\partial <\Omega>_0}{\partial m_j}. \tag{4.25}$$

Now, the magnetisation can be written

$$\vec{m}_i = L(\beta|\vec{h}_i^{MF} + \vec{h}_i^{ext}|)\frac{\vec{h}_i^{MF} + \vec{h}_i^{ext}}{|\vec{h}_i^{MF} + \vec{h}_i^{ext}|}, \tag{4.26}$$

where the field $\vec{h}_i$ breaks into mean-field ($\vec{h}_i^{MF}$) and external field ($\vec{h}_i^{ext}$) parts . Near and above the Curie temperature the magnetisation and the fields are small so that

$$\vec{m}_i \simeq \frac{1}{3}\beta(\vec{h}_i^{MF} + \vec{h}_i^{ext}). \tag{4.27}$$

The susceptibility $\bar{\chi}_{ij} \equiv \partial m_i / \partial h_j^{\text{ext}}$ in paramagnetic state $\{\vec{m}_i\} = 0$ with zero external field is given by

$$\bar{\chi}_{ij} = \frac{1}{3}\beta\delta_{ij} + \frac{1}{3}\beta\sum_k S_{ik}^{(2)}\chi_{kj}, \tag{4.28}$$

where

$$S_{ik}^{(2)} = \frac{\partial h_i}{\partial m_k} = -\left(\frac{\partial^2 <\bar{\Omega}>_0}{\partial m_i \partial m_k}\right)_{\{\vec{m}_i=0\}}. \tag{4.29}$$

In a paramagnetic state, the system is homogeneous; thus, $S_{ij}^{(2)}$ depends on the distance between site i and j. However, by taking Fourier Transform, the susceptibility becomes

$$\chi(q, T) = \frac{\mu^2}{3k_BT - S^{(2)}(q, T)}, \tag{4.30}$$

where μ the magnitude of the local moment is included to fix the units. This is the condition to find T_C from mean-field approximation

$$T_C = \frac{S^{(2)}(q, T)}{3k_B}. \tag{4.31}$$

Now, the remaining part is to find $S_{ij}^{(2)}$. Nevertheless, if we assume that the grand potential Ω is the classical Heisenberg model

$$H = -\sum_{ij} J_{ij}\hat{\mathbf{e}}_i \cdot \hat{\mathbf{e}}_j. \tag{4.32}$$

Then, in paramagnetic state,

$$<\Omega>_0 = <H>_0 = -\sum_{<ij>} J_{ij}m_i m_j, \tag{4.33}$$

where m is assumed to be the magnitude of the magnetic moment. As a result, we may associate

$$S_{ij}^{(2)} = \frac{\partial^2 <H>_0}{\partial m_i \partial m_j}, \tag{4.34}$$

with an 'exchange parameter' to use in a classical Heisenberg model for the Monte Carlo simulations. $S_{ij}^{(2)}$ can be determined from spin-polarised screened Korringa-Kohn-Rostoker (KKR) Coherent-Potential Approximation (CPA) calculations. A few brief details are given below and more information can be found in references [39, 40].

4.4 Spin Polarised Screened KKR-CPA

The KKR method [57] is a tool used to solve the Schrödinger equation via Green's functions. Moreover, in the paramagnetic state of the DLM picture, the problem can be mapped onto a random binary alloy system $A_{0.5}B_{0.5}$ [39, 40] with A and B represent up spin and down spin for a particular site. Then, it is possible to use KKR-CPA method [58] for disordered alloys to find $S_{ij}^{(2)}$.

In this section, we give a very brief description about KKR-CPA theory which is used to extract scattering matrices (for a more details, consult e.g. [59]). Next, by moving to layer structures, we make a summary about how to find the 'exchange parameter' in thin-film systems.

4.4.1 KKR

The KKR calculation starts from an effective potential describing the interaction of a single electron with the nuclear Coulomb potential $V_0(r) = \frac{Ze^2}{r}$ for all r up to muffin tin radius plus Hartree and exchange correlation potential. Then, this potential is put into the Schrödinger equation and the t-matrix (t) is found from the scattering solution. Next the free electron Green's function G_0 is determined and, included with the t-matrix t, the scattering-path operator τ (multiple site scattering operator) is formed (e.g. [59]).

Next, τ is used to calculate the total Green's function G leading to electron density $n(\vec{r})$ as one of its observables. After that, $n(\vec{r})$ is used to find the new effective potential ν^{eff} and the whole processes repeated until there is consistency. The whole process need to be done for both up and down spins together.

In a description of the DLM paramagnetic state, an average over different orientational configurations needs to be taken. The Coherent Potential Approximation

(CPA) [58] is used to solve this problem of electron propagation through a disordered arrays of fields.

4.4.2 Coherent Potential Approximation (CPA)

The idea of the CPA is to create an effective medium from the real alloy system (e.g. disordered binary alloy $A_c B_{1-c}$) [58, 60, 61]. An electron propagating through this effective medium should behave similarly to an electron moving through the disordered lattice on the average. Then, to create the effective medium, by considering a random lattice where each site is occupied by either ν_A^{eff} or ν_B^{eff}, the real t-matrices t_α related to the its own potentials ν_α^{eff} (α is either type A or B) is replaced by a new effective t-matrix for that effective medium through the CPA ansatz

$$cX_A + (1 - c)X_B = 0, \tag{4.35}$$

where X is an 'extra' scattering from $A(B)$ site and is given by

$$X_{A(B)} = \left[\left(t_{A(B)}^{-1} - t^{-1} \right)^{-1} + \tau^{00} \right]^{-1}; \qquad X_A + X_B = 0, \tag{4.36}$$

which the quantities τ^{ij} are the CPA path-operator matrices in the site-representation, $t_{A(B)}$ is the scattering matrix for the $A(B)$ type, and t is the scattering matrix for the CPA effective medium.

For a DLM paramagnetic state, a site with the local magnetic moment pointing in any $\hat{e}$ direction in the effective medium has a probability density $P(\hat{e}) = 1/4\pi$ and it can be shown that the CPA condition becomes [62]

$$\frac{1}{2}[1 + (t_\downarrow^{-1} - t^{-1})\tau]^{-1} + \frac{1}{2}[1 + (t_\uparrow^{-1} - t^{-1})\tau]^{-1} = 1, \tag{4.37}$$

where $t_{\uparrow(\downarrow)}$ is spin up(down) scattering matrix in the local coordinate system which direction of $\hat{e}$ is the local z axis. t and τ are the scattering matrix and path operator calculated from the effective medium. As can be seen, eq. (4.37) and eq. (4.35) are equivalent for binary alloy system for $c = 0.5$ i.e. $A_{0.5}B_{0.5}$ [39, 40, 62].

From the KKR-CPA [63, 64], an expression for the $S^{(2)}_{P_iQ_k}$ 'exchange parameters' for both bulk system and thin-films can be written in terms of $t_\uparrow$, $t_\downarrow$, t, and τ where i, k belong to layers P, Q respectively, and for layered systems the paramagnetic spin susceptibility after making two dimensional Fourier transformation is given by [65]

$$\chi_{PQ} = \left[3k_BT\mathbf{I} - \mathbf{S}^{(2)}(\vec{q}_\parallel)\right]^{-1}_{PQ} m_Q^2,\qquad(4.38)$$

where $\vec{q}_\parallel$ is a reciprocal vector along in-plane directions in any layers and m_P the magnetic moment in layer P and $\mathbf{S}^{(2)}$ is a matrix with elements $S^{(2)}_{PQ}$. Then the mean-field Curie temperature for the paramagnetic to ferromagnetic transition is obtained by solving [65]

$$||3k_BT_C\mathbf{I} - \mathbf{S}^{(2)}(\vec{q}_\parallel = 0)|| = 0,\qquad(4.39)$$

where T_C = (Largest positive eigenvalue of $\mathbf{S}^{(2)}(\vec{q}_\parallel))/3k_B$.

4.5 Magneto Crystalline Anisotropic Energy

In addition to the exchange energy, we now discuss the energy involved in rotating the magnetisation from a direction of low energy (easy axis) to a direction of high energy (hard axis) i.e. the anisotropic energy. Usually, for transition ferromagnets, the energy difference between hard and easy axes is very small compared to the exchange energy.

The anisotropic energy consists of two parts, one from spin-orbit coupling effects on the electronic bands and the other from the magnetic dipole interaction. However, the dipole interaction is very long ranged so it is very computer-time expensive. Thus, at this moment, we consider only the electronic band term.

For the classical Heisenberg model, we can phenomenologically insert an extra

anisotropic part into the Hamiltonian

$$H = -\sum_{ij} J_{ij}\hat{e}_i \cdot \hat{e}_j - \sum_i K_i(\hat{e}_i \cdot \hat{n})^2, \qquad (4.40)$$

which $\hat{n}$ is a unit vector pointing along the film surface. Notice that in this case, some approximations are used i.e. the anisotropic energy is assumed to be described by

$$E_{ani} \simeq \sum_i K_i(\hat{n} \cdot \hat{e}_i)^2, \qquad (4.41)$$

where K_i is an anisotropic constant extracted from (under the constraint of ferromagnetic configuration of moments i.e. $\hat{e}_i = \hat{e}$ for every site)

$$K_i = E_i(\hat{e} = \perp) - E_i(\hat{e} = \parallel), \qquad (4.42)$$

where $\perp$ and $\parallel$ refer respectively to the perpendicular and parallel directions to the film surface. This energy difference K is due to spin-orbit coupling which breaks the rotational invariance with respect to the spin quantization axis. It can be calculated by using ab-initio density functional methods extended to include relativistic effects. The usual way is to determine the total energy choosing the magnetisation along two nonequivalent directions via the using of the 'force theorem' or frozen potential approximation (see e.g. [66]).

For thin-film geometry, where all moments in the same layer are identical but vary from layer to layer, two calculations need to be performed. Firstly, all moments are forced to point along perpendicular direction to the surface ($\perp$) Then, they are forced again, but this time along the in-plane direction ($\parallel$). Next, the difference of the band energy $K_{Pi} = K_P \equiv \triangle E_P$ in layer P is calculated as [45, 46]

$$\triangle E = E(\perp) - E(\parallel) = \sum_P \triangle E_P. \qquad (4.43)$$

For a layer P, from the CPA, $\triangle E_P$ is defined as

$$\triangle E_P = \int_{-\infty}^{\epsilon_F^\perp} n_\perp^P(\epsilon)\epsilon d\epsilon - \int_{-\infty}^{\epsilon_F^\parallel} n_\parallel^P(\epsilon)\epsilon d\epsilon \qquad (4.44)$$

$$= \int_{-\infty}^{\epsilon_F^\parallel} (n_\perp^P(\epsilon) - n_\parallel^P(\epsilon))\epsilon d\epsilon - \int_{\epsilon_F^\perp}^{\epsilon_F^\parallel} n_\perp^P(\epsilon)\epsilon d\epsilon \qquad (4.45)$$

where P specifies a certain layer and $n^P_{\perp(\parallel)}(\epsilon)$ are the layer and component projected local densities of states. Since $\int_{\epsilon^\perp_F}^{\epsilon^\parallel_F} n^P_\perp(\epsilon)\epsilon d\epsilon$ is rather very small, $K \equiv \triangle E$ is usually termed the 'band energy contribution' to the magnetic anisotropy.

4.6 Conclusion

In this chapter, we have presented some information about how to extract 'exchange parameter' from 'first principles' electronic structure calculations within the DLM picture and adding the magnetic anisotropic terms. In the next chapter, we will use these exchange and anisotropic parameters to simulate Fe/W(001) thin-films using the classical Heisenberg model.

Chapter 5

Monte Carlo Applications to Fe/W (001) Thin-Films

5.1 Introduction

In this chapter, we study a more realistic model that uses the 'exchange parameters' extracted from the 'first principles' electronic structure calculations based on the Disordered Local Moment (DLM) theory which was discussed in chapter 4. Thus, it is now possible to calculate critical temperatures T_C in real units (Kelvin). However, unlike the Ising model, the order parameter is now a vector. So, we need to use the classical Heisenberg model [41].

In the classical isotropic Heisenberg model, it was proved rigorously by Mermin and Wagner [42] and Hohenberg [67] that for a $2D$ infinite system with not too long ranged interactions and in the absence of an external field, the magnetisation magnitude is always zero for any finite temperatures i.e.

$$<m_z>_{N=\infty} \simeq \frac{\text{const}}{\sqrt{T}} \frac{1}{|\ln |\vec{h}||^{1/2}} \rightarrow 0 \text{ as } |\vec{h}| \rightarrow 0, \tag{5.1}$$

where $\bar{h}$ is an external field along z direction. This was later supported by Jasnow and Fisher [68] who proved the similar theorem without the necessity of introducing a symmetry breaking field saying that for $T > 0$

$$<m_z^2>_{h=0} \simeq \frac{\text{const}}{\ln N} \to 0 \qquad (5.2)$$

as number of spins $N \to \infty$. This was later confirmed by Fröhlich and Pfister [69].

Nevertheless, all proofs do not prohibit other types of the phase transitions such as the divergence of the response of the magnetisation to the external magnetic field i.e. the magnetic susceptibility. These kind of phenomena (the divergence of the susceptibility) has been found by using high temperature series expansions [70]-[72].

However, in contrast to $2D$ systems, the $3D$ Heisenberg systems present the usual phase transition where the broken symmetry of the order parameter takes place at finite temperatures. So, in this chapter, we use Monte Carlo simulations to study the Heisenberg ferromagnetic thin-films. We investigate their transitional behaviour, their dependence upon film thickness, and their development from $2D$ to $3D$. In addition, we also study a Heisenberg model which possesses a small anisotropic component in the Hamiltonian eq. (5.4) and investigate how this affects the results.

5.2 Theoretical Background

5.2.1 The Classical Heisenberg Model

By considering the exchange energy arising from exchanging the electrons among the atoms, proposed by Dirac [73], and taking the classical limit, the following hamiltonian can be proposed.

$$H = -\sum_{ij} J_{ij} \vec{S}_i \cdot \vec{S}_j. \qquad (5.3)$$

65

This leads to the Heisenberg model of ferromagnetism [41]. In this spin model, $\vec{S}_i$ is a unit vector in three dimensional space and denotes the direction of the average electron spins in an atom. The magnitude of spin moments are absorbed inside the exchange parameter J_{ij}. Phenomenologically, we can include an anisotropic energy to produce a more realistic Hamiltonian for an anisotropic shaped system, e.g. thin-films, as

$$H = -\sum_{ij} J_{ij}\vec{S}_i \cdot \vec{S}_j - \sum_i K_i(\hat{n} \cdot \vec{S}_i)^2, \tag{5.4}$$

where J_{ij} and K_i are extracted from the 'first principles' as describe in the previous chapter and $\hat{n}$ is a unit normal vector to the film surface which we choose to be z direction.

5.2.2 Algorithms

Bias Metropolis Algorithm

For both Heisenberg and Ising models, the Metropolis algorithm updates each spin individually by using the same acceptance probability eq. (2.25) even with anisotropic Hamiltonian. This leads to simulations, which are based on this Metropolis, suffering from high correlation times especially when the temperature is very low and many spins prefer to align along the same direction. Thus, to make just only one spin point into a different direction costs large energy (especially when the spin's new direction is very different from its old direction) and the move is likely to be rejected.

Thus, to rectify this lack of movement (bringing about large correlation time), one can increase the probability of accepting the new randomly chosen state by making a bias function such that the new randomly chosen spins are slightly different from the current considered spins. In some pioneering works on the Heisenberg model

66

[74, 75], the bias random spin was chosen to be

$$\vec{S}'_{i\alpha} = \frac{\vec{S}_{i\alpha} + \Delta\xi_\alpha}{\left[\sum_\alpha (\vec{S}_{i\alpha} + \Delta\xi_\alpha)^2\right]^{1/2}},$$

(5.5)

where α is the Cartesian spin components, ξ_α is a uniform random number between +1 and -1, and Δ is a limit for the maximum allowance for the spin components to change. However, it was later pointed out that this bias function provides incorrect results which are not reliable at low temperatures as the function does not provide a homogeneous distribution of the new random spin $\vec{S}'_i$ directions around the old spin $\vec{S}_i$ [76]. Thus, a better version of the bias function was given as [76]

$$\vec{S}'_i = \cos\theta_i\vec{S}_i + \sin\theta_i\vec{w}_i,$$

(5.6)

where $\vec{w}_i$ is a random unit vector normal to $\vec{S}_i$, and θ_i is the angle between old spin $\vec{S}_i$ and the new chosen spin $\vec{S}'_i$ which is defined by

$$\cos\theta_i = 1 + \xi_i(\cos\theta_{max} - 1),$$

(5.7)

where ξ_i is a random number between 0 and 1, and θ_{max} is the maximum allowed angle from which the new spin can rotate.

Wolff Algorithm

In the Wolff algorithm, for continuous spin models $O(n)$, Wolff [12] proposed a transformation function as

$$R(\hat{r})\vec{S}_i = \vec{S}_i - 2(\vec{S}_i \cdot \hat{r})\hat{r},$$

(5.8)

where $\hat{r}$ is a unit vector chosen to be a random mirror plane and $\vec{S}_i$ is also a unit vector referring to a spin. We can notice that $R(S_i) = -S_i$ in the Ising model.

To apply this algorithm to the simulation, we make a group of spins by firstly choosing both random mirror plane $\hat{r}$ and the lattice site i. Then, we mark i and

visit all sites connecting to i and add them to form a group with a probability

$$P(\vec{S}_i, \vec{S}_j) = 1 - \exp\{\min(0, -2\beta J_{ij}(\hat{r} \cdot \vec{S}_i)(\hat{r} \cdot \vec{S}_j))\}. \tag{5.9}$$

If $\vec{S}_j$ is successfully added, j is marked and the process is continued iteratively until no more new spins are added. Finally, we flip all the spins in the cluster (group), $\vec{S}_i \rightarrow R(\vec{S}_i)$. In this way, $(\hat{r} \cdot \vec{S}_j)$ and $(\hat{r} \cdot \vec{S}_i)$ must have the same sign unless the probability of adding becomes zero. In the algorithm, the ergodicity is still guaranteed because P can be very small to flip only one site at a time. So any configurations can be reached. However, the cluster is always flipped only in the isotropic model eq. (5.3). If we want to apply this Wolff method to the anisotropic system eq. (5.4), we need to carefully analyse the acceptance probability in detail as in the following.

By considering detailed balance eq. (2.21), we can start by considering two states $\{\vec{S}_i\}$, μ and $\{\vec{S}_i'\}$, ν that differ by a flip $R(\hat{r})$ on a cluster c. Next, by considering the selective probability ratio , we get

$$\frac{g(\mu \rightarrow \nu)}{g(\nu \rightarrow \mu)} = \prod_{<i,j> \, \in \, \partial c} \frac{1 - P(R(\hat{r})\vec{S}_i, \vec{S}_j)}{1 - P(R(\hat{r})\vec{S}_i', \vec{S}_j')}$$

$$= \left\{ \frac{\exp\left[-2\beta \sum_{(\vec{S}_i \cdot \hat{r})(\vec{S}_j \cdot \hat{r}) \geq 0} J_{ij}(\vec{S}_i \cdot \hat{r})(\vec{S}_j \cdot \hat{r})\right]}{\exp\left[-2\beta \sum_{(\vec{S}_i' \cdot \hat{r})(\vec{S}_j' \cdot \hat{r}) \geq 0} J_{ij}(\vec{S}_i' \cdot \hat{r})(\vec{S}_j' \cdot \hat{r})\right]} \right\}_{<i,j> \, \in \, \partial c},$$

where ∂c contains all links $<i,j>$ with $i \in c$ and $j \notin c$. Since $j \notin c$ then $\vec{S}_j' = \vec{S}_j$, and we know that $\vec{S}_i' \cdot \hat{r} = R(\hat{r})\vec{S}_i \cdot \hat{r} = -\vec{S}_i \cdot \hat{r}$, giving

$$\frac{g(\mu \rightarrow \nu)}{g(\nu \rightarrow \mu)} = \left\{ \frac{\exp\left[-2\beta \sum_{(\vec{S}_i \cdot \hat{r})(\vec{S}_j \cdot \hat{r}) \geq 0} J_{ij}(\vec{S}_i \cdot \hat{r})(\vec{S}_j \cdot \hat{r})\right]}{\exp\left[+2\beta \sum_{(\vec{S}_i \cdot \hat{r})(\vec{S}_j \cdot \hat{r}) < 0} J_{ij}(\vec{S}_i \cdot \hat{r})(\vec{S}_j \cdot \hat{r})\right]} \right\}_{<i,j> \, \in \, \partial c}$$

$$= \exp\left[-2\beta \sum_{<i,j> \, \in \, \partial c} J_{ij}(\vec{S}_i \cdot \hat{r})(\vec{S}_j \cdot \hat{r})\right]. \tag{5.10}$$

However, if we consider Hamiltonian with only the exchange interaction term eq. (5.3), we can find the energy difference between the old and new configuration after

68

flipping a cluster of spins as

$$\Delta E \equiv E_\nu - E_\mu = - \sum_{<ij>} J_{ij}(\vec{S}'_i \cdot \vec{S}'_j - \vec{S}_i \cdot \vec{S}_j), \qquad (5.11)$$

where S'_i and S'_j belong to the new configuration (after flipping). Now, we can analyse this energy difference in several cases as :-

1. If $\vec{S}_i$ and $\vec{S}_j$ were not in the flipped cluster; then $\vec{S}'_i = \vec{S}_i$ and $\vec{S}'_j = \vec{S}_j$ so

$$\vec{S}'_i \cdot \vec{S}'_j - \vec{S}_i \cdot \vec{S}_j = 0.$$

2. If both $\vec{S}_i$ and $\vec{S}_j$ were in the flipped cluster; then $\vec{S}'_i = R(\hat{r})\vec{S}_i = \vec{S}_i - 2(\vec{S}_i \cdot \hat{r})\hat{r}$ (and so as $\vec{S}'_j$), so again

$$\vec{S}'_i \cdot \vec{S}'_j - \vec{S}_i \cdot \vec{S}_j = (\vec{S}_i - 2(\vec{S}_i \cdot \hat{r})\hat{r}) \cdot (\vec{S}_j - 2(\vec{S}_j \cdot \hat{r})\hat{r}) - \vec{S}_i \cdot \vec{S}_j = 0.$$

3. If $\vec{S}_i$ was in the flipped cluster, but $\vec{S}_j$ was not, then

$$\begin{aligned}
\vec{S}'_i \cdot \vec{S}'_j - \vec{S}_i \cdot \vec{S}_j &\equiv R(\vec{S}_i) \cdot \vec{S}_j - \vec{S}_i \cdot \vec{S}_j \\
&= \vec{S}_i \cdot \vec{S}_j - 2(\vec{S}_i \cdot \hat{r})(\vec{S_j} \cdot \hat{r}) - \vec{S}_i \cdot \vec{S}_j \\
&= -2(\vec{S}_i \cdot \hat{r})(\vec{S_j} \cdot \hat{r}).
\end{aligned}$$

4. If $\vec{S}_i$ was not in the flipped cluster, but $\vec{S}_j$ was, this case is discarded as it is the double sum of the previous case and we do not include.

Thus, the detail balance condition becomes

$$\frac{A(\mu \to \nu)g(\mu \to \nu)}{A(\nu \to \mu)g(\nu \to \mu)} = e^{-\beta \Delta E} = \exp\left[-2\beta \sum_{<i,j> \,\in\, \partial c} J_{ij}(\vec{S}_i \cdot \hat{r})(\vec{S}_j \cdot \hat{r})\right], \qquad (5.12)$$

and by using eq. (5.10), we get the acceptance ratio as

$$\frac{A(\mu \to \nu)}{A(\nu \to \mu)} = 1. \qquad (5.13)$$

So we can always flip the cluster after it is formed provided that there is only isotropic terms (J_{ij}) in the hamiltonian.

However, when looking at the anisotropic hamiltonian eq. (5.4), the energy difference from the anisotropic part is

$$(\Delta E)^{ani} \equiv E^{ani}_\nu - E^{ani}_\mu = -\sum_i K_i \left[(\hat{n} \cdot \vec{S}'_i)^2 - (\hat{n} \cdot \vec{S}_i)^2 \right], \qquad (5.14)$$

where $\hat{n}$ is a unit vector normal to film surface (z axis). Similarly, we can notice that :-

1. If $\vec{S}_i$ was not in the cluster, so $\vec{S}'_i = \vec{S}_i$ giving

$$(\hat{n} \cdot \vec{S}'_i)^2 - (\hat{n} \cdot \vec{S}_i)^2 = 0.$$

2. However, if $\vec{S}_i$ was in the cluster, then

$$\begin{aligned}
(\hat{n} \cdot \vec{S}'_i)^2 - (\hat{n} \cdot \vec{S}_i)^2 &= \left(\left[\hat{n} \cdot \vec{S}_i - 2(\vec{S}_i \cdot \hat{r})(\hat{r} \cdot \hat{n}) \right]^2 - (\hat{n} \cdot \vec{S}_i)^2 \right) \\
&= 4(\vec{S}_i \cdot \hat{r})(\hat{r} \cdot \hat{n}) \left[(\vec{S}_i \cdot \hat{r})(\hat{r} \cdot \hat{n}) - (\hat{n} \cdot \vec{S}_i) \right],
\end{aligned}$$

which does not vanish. Nevertheless, the selection ratio from eq. (5.10) cancels only the term $\exp(-\beta(\Delta E)^{iso})$, so the acceptance ratio in this anisotropic hamiltonian is

$$\frac{A(\mu \to \nu)}{A(\nu \to \mu)} = \exp \left[-4\beta \sum_{i \epsilon c} K_i (\vec{S}_i \cdot \hat{r})(\hat{r} \cdot \hat{n}) \left\{ (\hat{n} \cdot \vec{S}_i) - (\vec{S}_i \cdot \hat{r})(\hat{r} \cdot \hat{n}) \right\} \right], \qquad (5.15)$$

and now the cluster of spins will be flipped with this probability.

As can be seen, the Wolff algorithm for the anisotropic hamiltonian is more complicated than the Metropolis. Nevertheless, the reason for considering the Wolff algorithm is that, usually, the Metropolis algorithm gives very high correlation times for simulations at low temperatures and in the critical region which brings about large statistical errors. So, we believe that by introducing the Wolff algorithm, the correlation time will be cut down in the same way as for the Ising model. However, for

70

more complicated Hamiltonians (e.g. including dipolar interaction), the Metropolis may still be a good choice.

At this stage, we now have 3 algorithm choices; the (original) Metropolis, the bias Metropolis, and the Wolff algorithms. So, before making any long simulations, we need to perform some tests of result reliability and correlation time to determine which is the best.

5.2.3 Measurements

The observables we are interested in are the magnetisation magnitude m and the magnetic susceptibility χ. However, as now the spins are vectors, the magnetisation is measured via

$$m = \frac{1}{N} \sqrt{ \sum_{i=1}^{N} \vec{\mathbf{S}}_i \cdot \sum_{j=1}^{N} \vec{\mathbf{S}}_j }. \tag{5.16}$$

We also need to record the energy of the system to extend our results via the histogram method. However, as now the energy become a continuous value, we cannot use each histogram bin for each specific energy like in the Ising model. Instead, we need to divide the range of the maximum and the minimum energy difference $(E_{max} - E_{min})$ for the simulated temperature into many bins. Then, when a measured energy has its value within the ith bin (E_i^{max} and E_i^{min}), we increase the number of data in this bin by one. In our simulations, for each temperature, we record data for 3 sizes of the histograms which are 1000 , 5000 , and 10000 bins. Then, by using the histogram method, we can now check how many bins (at a particular temperature) the system requires so that the number of histogram bins does not affect the results.

5.2.4 Critical Temperatures and Critical Exponents

From previous Monte Carlo work on the $2D$ classical Heisenberg magnet [77], it was pointed out that there exists a nonzero magnetisation for finite temperatures when using finite size systems. However, when increasing the system linear size L, except at zero temperature, the magnetisation converges very slowly to zero. So, this is consistent with Mermin and Wagner's work [42] as the rigorous proof is based on $N = \infty$. The slow convergence of the magnetisation was explained in terms of short-ranged order which appears to exceed the simulated system sizes making fluctuation in the samples and bringing about poor Monte Carlo convergence. This behaviour was confirmed in [75] as it was found that the average of the square of the magnetisation $<m^2>$ varies as N^{-x} with $0 < x < 1$.

Then, if this slow convergence also appears in our thin-film Monte Carlo work, it may not be possible to use the fourth order cumulant eq. (3.14) of the magnetisation to find the critical temperature T_C. Fortunately, there is an alternative way to avoid using the cumulant to find the critical temperature T_C.

By recalling the susceptibility scaling function $\tilde{\chi}$ from chapter 3 eq. (3.15)

$$\chi_L(T, l) = L^{\gamma/\nu}\tilde{\chi}(L^{1/\nu}t, l), \tag{5.17}$$

it can be pointed out that temperature T_0 associated to the peak of the susceptibility χ corresponds to the scaling parameter $x_0 = L^{1/\nu}t_0$ at the peak of the scaling susceptibility (e.g. figure 3.11). So, for all system size L's, the temperature T_0's corresponding to x_0's can be given by

$$T_0 = T_C(1 + x_0 L^{-1/\nu}). \tag{5.18}$$

Thus, by using nonlinear curve fitting, we may be able to find T_C and ν separately. However, in this case, to estimate both 2 parameters ν and T_C requires very high accuracy data.

72

5.3 Simulations

For our realistic thin-film simulations, we take Fe/W (001) films as a case study because the 'exchange parameters' extend to only the first-nearest neighbour pairs and second-nearest neighbour pairs that are in the same layer (figure 5.1). From the figure (5.1), the 2nd nearest neighbour interaction (2nn) is the intra-layer interaction and the 1st nearest neighbour (1nn) represents the inter-plane interaction. So, this means 2nn describes the tendency that spins in a same layer will point along the same direction and 1nn implies the possibility that magnetisation in that layer will point along the same direction with the adjacent layers.

In the simulations, the BCC structure of the Fe/W films is prepared by using the mapping function we described in chapter 2. We perform simulations for both the isotropic eq. (5.3) and anisotropic models eq. (5.4) where the anisotropic constants are again extracted from the 'first principles' and shown in figure (5.2) which we can see that the surface layers have the strongest anisotropic magnitude. However, even the strongest anisotropic constant is still about a hundred times smaller than the 'exchange interaction'; so it is likely that the anisotropic energy might not alter greatly the results from the original isotropic system. We will check this with our simulations described in this chapter.

In our studies, we vary the film thicknesses l from 2 to 8 layers. The reason we stop at 8 layered film is that the mean-field critical temperature T_C^{MF} for 8 layered film is about the same magnitude as in the bulk system [65]. Moreover, one may notice that we omit the monolayer film. This is because we are interested only the transition from paramagnetic to ferromagnetic phase. However, the 'first principles' calculations, for the monolayer film, gives anti-ferromagnetic 'exchange parameter' (in agreement with experiment [78, 79]) and indicates non-ferromagnetic behaviour in the monolayer case.

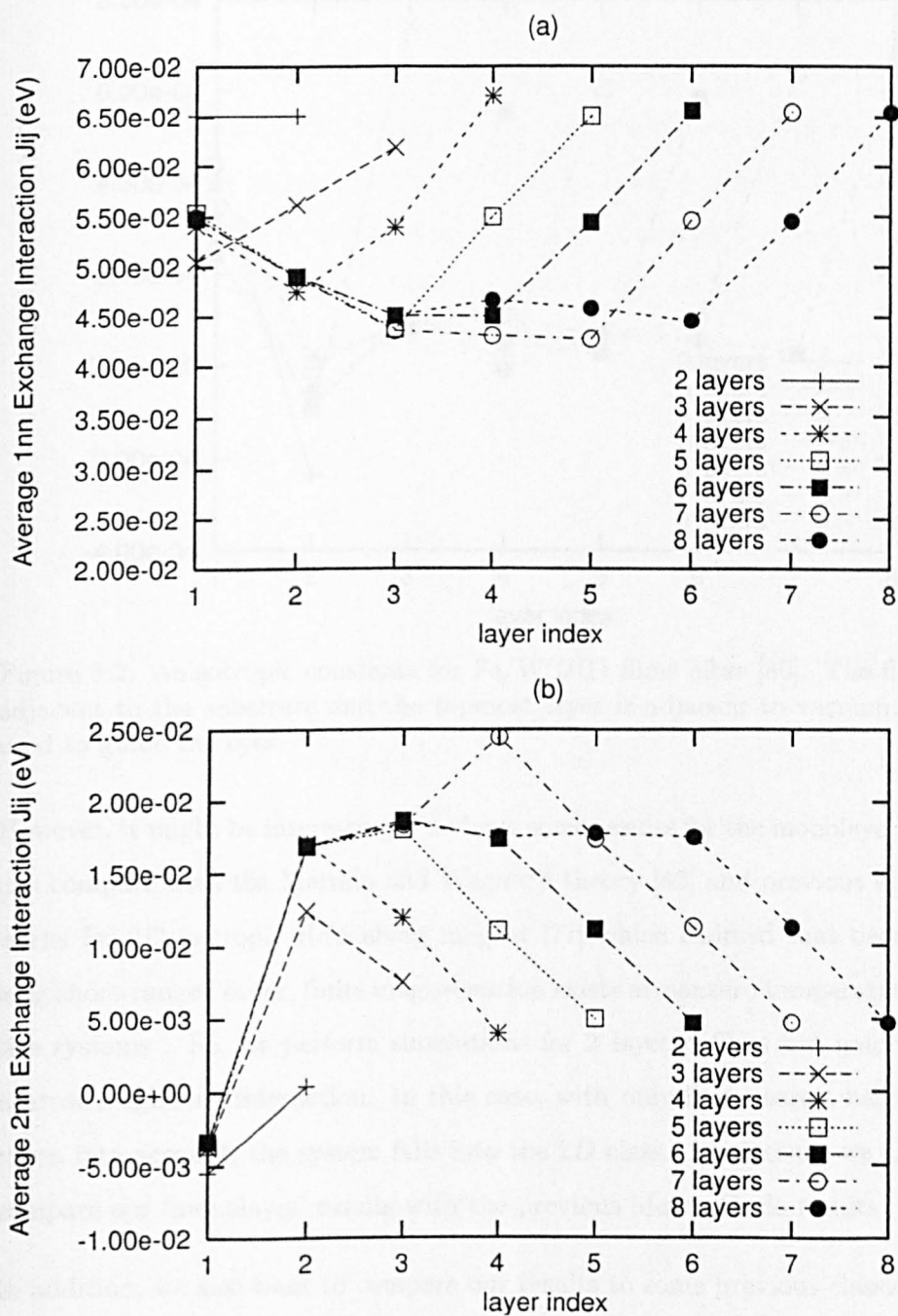Figure 5.1: Average 1st and 2nd nearest neighbour 'exchange parameter' for Fe/W(001) films up to 8 layers after [80]. The first layer is adjacent to the substrate and the topmost layer is adjacent to vacuum. Lines are used to guide the eyes.

74
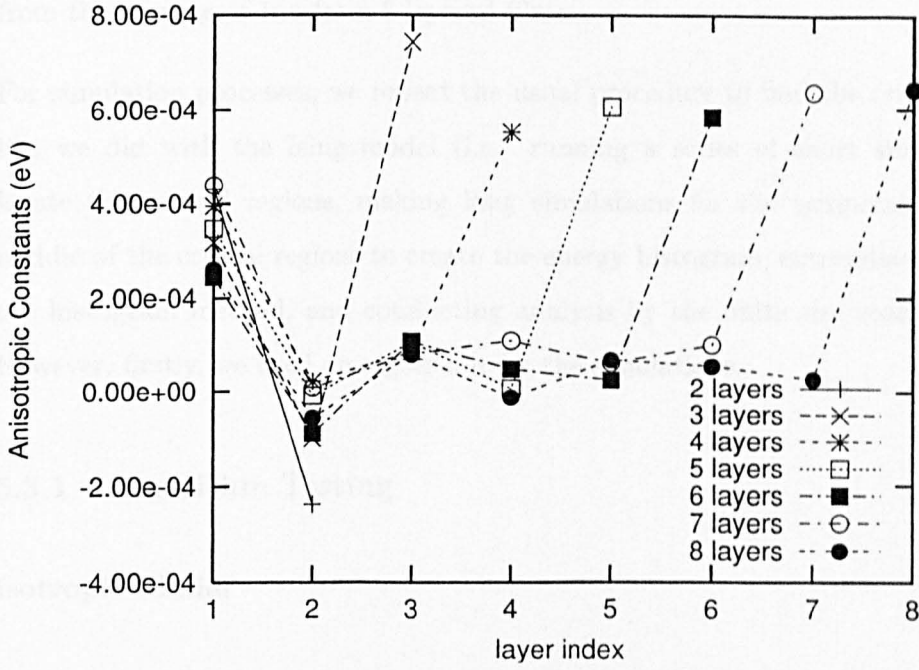
Figure 5.2: Anisotropic constants for Fe/W(001) films after [80]. The first layer is adjacent to the substrate and the topmost layer is adjacent to vacuum. Lines are used to guide the eyes.

However, it might be interesting if we have some results for the monolayer so that we can compare with the Mermin and Wagner's theory [42] and previous Monte Carlo works for $2D$ isotropic Heisenberg magnet [77] which claimed that because of the long short-ranged order, finite magnetisation exists at nonzero temperatures in finite size systems . So, we perform simulations for 2 layered films but ignoring second nearest neighbour interaction. In this case, with only first nearest neighbours are taken into account, the system falls into the $2D$ class. As a result, we can roughly compare our 'monolayer' results with the previous Monte Carlo results [77].

In addition, we also want to compare our results to some previous classical Heisenberg results on BCC bulk which claimed $k_B T_C/J$ to be 2.05612(81) [81] and 2.0540(6)[82] from series expansion methods, and 2.0541241(52) [83] from Monte Carlo work. Then, we perform simulations for the bulk system with 1nn only which is calculated

from the average of 1nn from 8 layered films.

For simulation processes, we repeat the usual procedure to find the critical regions like we did with the Ising model (i.e. running a series of short simulations to locate the critical regions, making long simulations for the temperatures at the middle of the critical regions to create the energy histogram, extrapolating data by the histogram method, and conducting analysis by the finite size scaling theory). However, firstly, we need an algorithm for the simulations.

5.3.1 Algorithm Testing

Isotropic Model

The algorithms we aim to test are the normal Metropolis (where there is no re-striction on the random choosing spins), the bias Metropolis (where the randomly chosen spins are limit to differ within some angles from the original), and the Wolff algorithms. The test is to investigate how well they can cut down the correlation time and how reliable are the results they give. So, by taking 2 layered Fe/W films as a study case, we perform simulations of $48 \times 48 \times 2$ isotropic Heisenberg magnet using all the mentioned algorithms. We omit the first 2000 magnetisation measurements for the equilibration and use up to 50000 data to calculate the correlation time τ i.e. figure (5.3).

From the figure, the time unit (mcs/site) is 1 attempt to flip a spin per site or 1 attempt to add a spin into a cluster for the Wolff algorithm. As can be seen, the bias Metropolis has smaller τ than the (original) Metropolis in low temperature region. However, for high temperatures, as angle θ_{max} in eq. (5.7) is controlled in a way that number of flipped spins is always 50% in one lattice sweep [76] when in fact the number of flipped spins should be very close to 100% in a high temperature phase; thus, the (normal) Metropolis (with no restrictions on the randomly chosen spins)
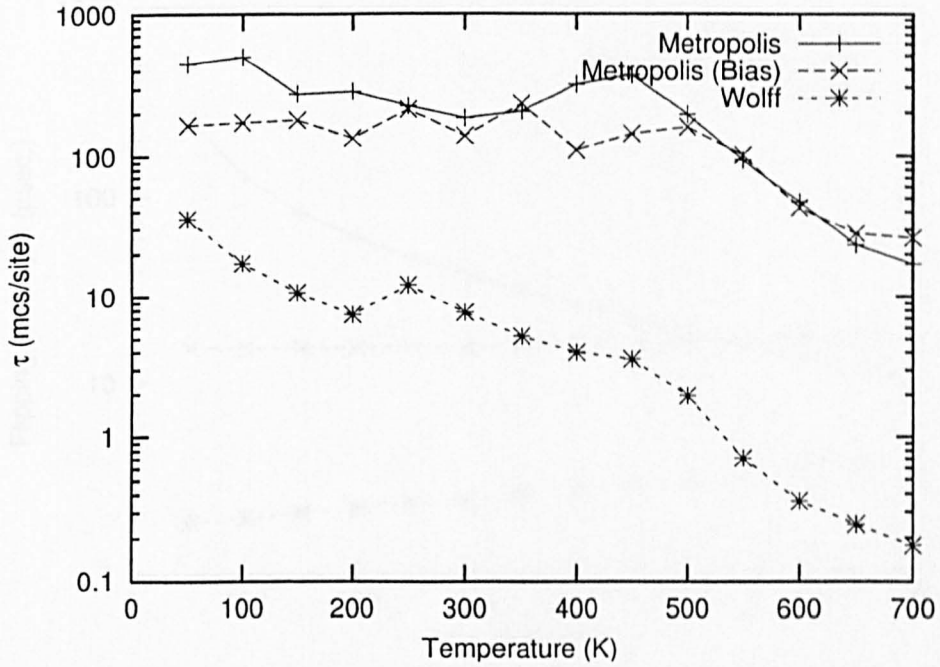
Figure 5.3: The correlation time against temperature for the Metropolis, the bias Metropolis, and the Wolff algorithm. The results are calculated from $48 \times 48 \times 2$ Heisenberg BCC films using 50000 observables with 2000 observables discarded for equilibration.

is proved to be more useful in this high temperature phase. On the other hand, the Wolff algorithm is the best algorithm as it gives the smallest correlation times for all temperatures we studied.

We can also compare the efficiencies of the algorithms by looking at the c.p.u. time used to successfully update one spin as in figure (5.4). With the same trend as figure (5.3), the bias Metropolis algorithm is better than the Metropolis at low temperatures, but worse at high temperatures. This is because the Metropolis suffers from low acceptance probability in the low temperature phase (very low thermal energy to move to new configurations), and for the high temperature phase, the higher thermal energy helps the Metropolis to increase the rate of spin flipping to be as high as the bias Metropolis, but the bias Metropolis uses more time to generate
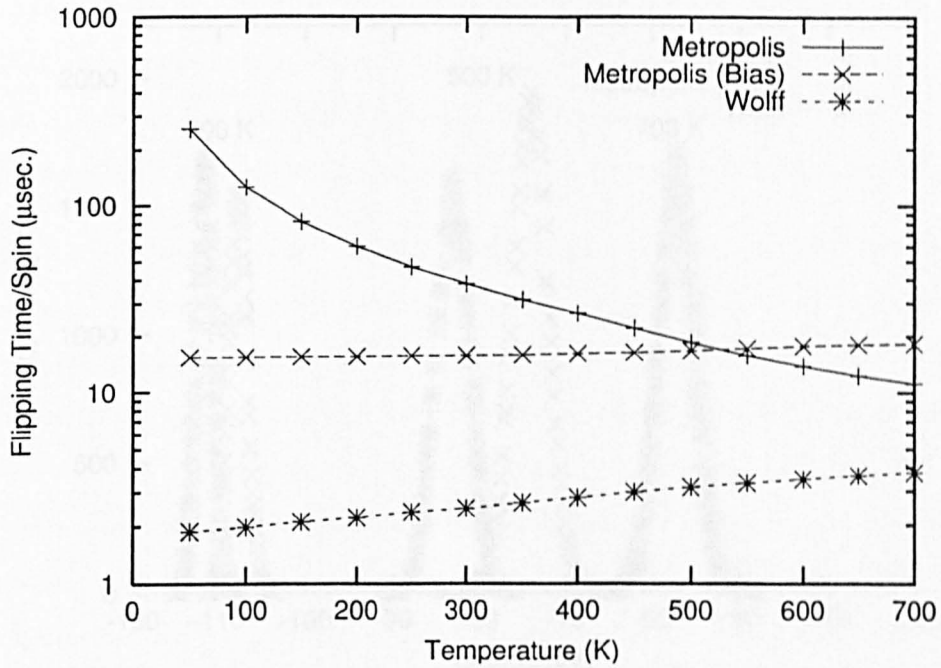
Figure 5.4: The computer time used to successfully update a spin from the Metropolis, the bias Metropolis, and the Wolff algorithm. The results are taken from the same system in figure (5.3). One can notice the crossing point of the Metropolis's at about 520 K which is the temperature at the middle of the critical region for $48 \times 48 \times 2$ BCC Heisenberg films.

spins. So, the Metropolis beats the bias Metropolis in paramagnetic region.

For the Wolff algorithm, with its consistent spin flipping, it is found to be the fastest algorithm to update the spins. However, it takes a longer time with increasing temperature because each spin starts to update individually, but it still consumes less time in comparison to the Metropolis's.

Moreover, we can also investigate the results these algorithms give by looking at the energy distribution (in terms of reliability) as in figure (5.5).

As we can see from the figure, the Metropolis and the Wolff algorithm results agree very well. However, for the bias Metropolis, except from high temperatures (paramagnetic phase), its results deviate from the Metropolis and the Wolff. This may

78
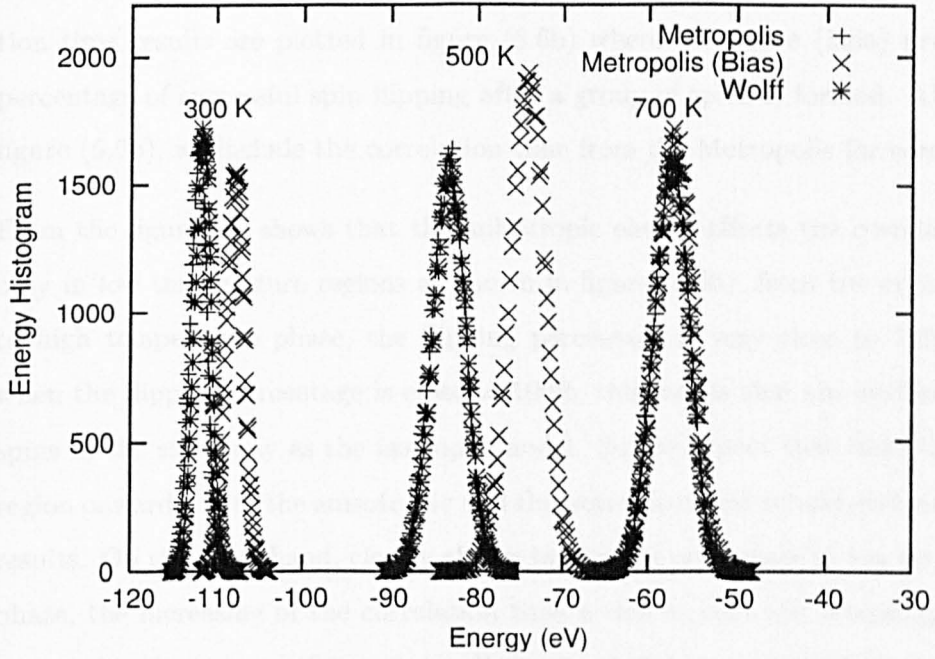
Figure 5.5: The total energy distribution from the Metropolis, the biased Metropolis, and the Wolff algorithm. The results are taken from the same system in figure (5.3).

be due to the bias on the randomly chosen spin to always make 50% of the spins flip in 1 lattice sweep (by increasing and decreasing θ_{max}) which at some points the system may already be in its equilibrium point. Thus, this lifts up the equilibrium energy state. So, we rule out the use of the bias Metropolis for our simulations. On the other hand, the Metropolis produces large correlation times. As a result, for all our isotropic simulations, we use the Wolff algorithm.

Anisotropic Model

As have been mentioned, in the anisotropic model, the Wolff algorithm does not always flip the spins after forming a group, but flips the group with a probability that is a function of the energy difference from the anisotropic part. Then, this can increase the correlation time in comparison to the correlation time from isotropic

model at the same temperature especially in low temperature phase. The correlation time results are plotted in figure (5.6b) where the figure (5.6a) presents the percentage of successful spin flipping after a group of spins is formed. Also, in the figure (5.6b), we include the correlation time from the Metropolis for comparison.

From the figures, it shows that the anisotropic energy affects the correlation time only in low temperature regions as shown in figure (5.6b), from the critical region to high temperature phase, the flipping percentage is very close to 100%. Also, when the flipping percentage is close to 100%, this means that the system flips the spins in the same way as the isotropic model. So, we expect that from the critical region onwards, both the anisotropic and the isotropic model should give very similar results. On the other hand, clearly shown by the low percentage in low temperature phase, the increasing of the correlation time is due to that the system spending a longer time in some configurations. However, this does not say if the anisotropic system should or should not produce deviations from the isotropic system. To check this, we need to investigate the magnitude of the magnetisation projected along the easy axis.

In terms of reliability, we check this from the energy distribution (histogram) measured from both these 2 algorithms for various temperatures and we have found that both 2 algorithms produce good agreement at all temperatures we perform as in the same as in the isotropic model. So, from the way the Wolff cuts down the correlation time from the Metropolis and its reliability, we again use the Wolff to simulate our anisotropic simulations.
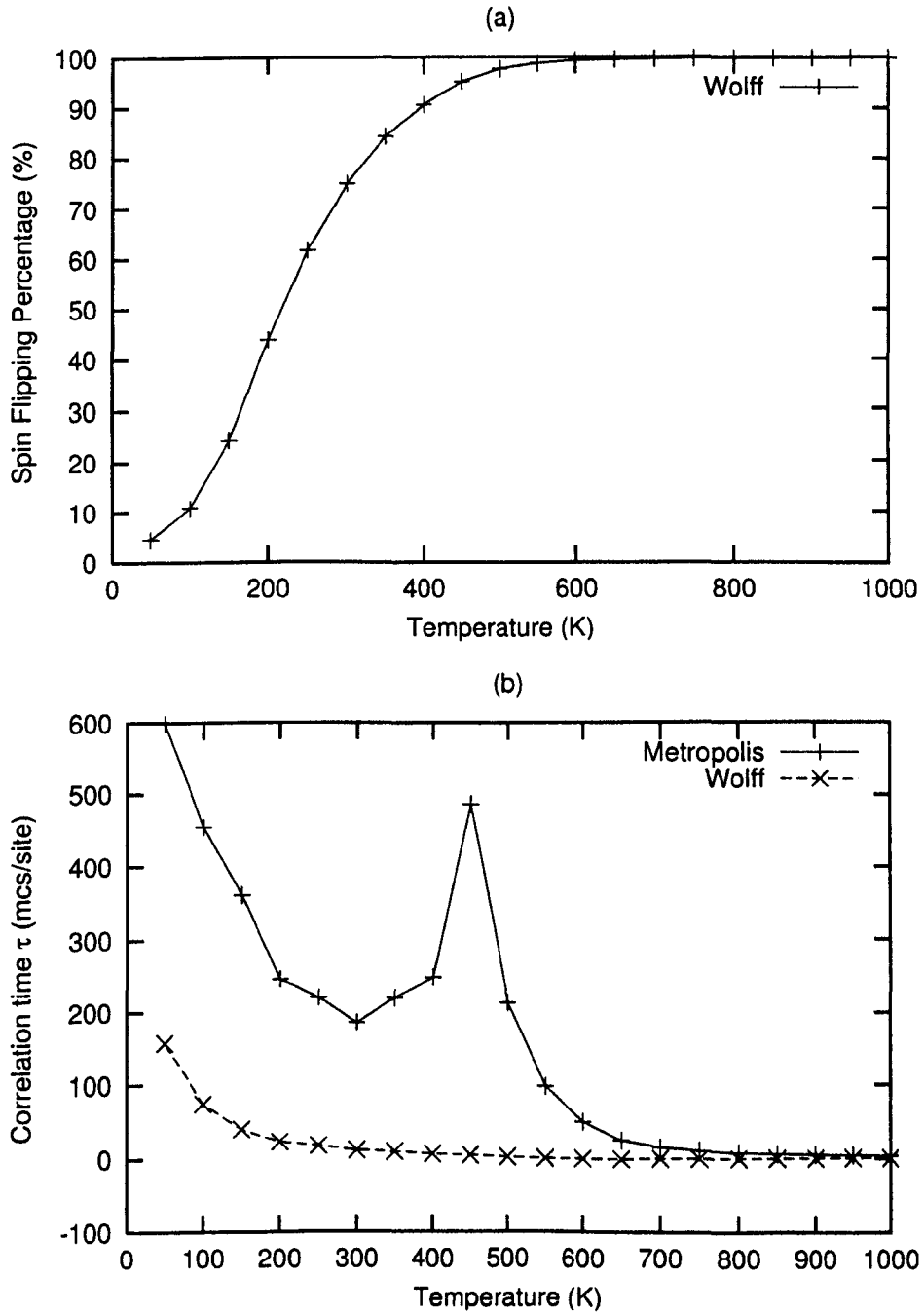
Figure 5.6: Percentage of successful spin updated after spin clusters are formed from the Wolff algorithm (a) and the correlation time comparison between the Metropolis and the Wolff algorithm (b) as a function of temperature in anisotropic model for $48 \times 48 \times 2$ Fe/W films. Lines are used to guide the eyes.

81

5.3.2 Isotropic Results

'Bulk' System

To compare our results with previous studies of $3D$ BCC Heisenberg magnet [81]-[83], we run simulations on the same lattice structure but using the average of 1nn from 8 layered Fe/W films as the 'bulk exchange parameter' and calculate the bulk critical temperature T_C from both the cumulant method shown in figure (5.7) and the nonlinear curve fitting eq. (5.18) shown in figure (5.8). For the critical exponents (γ, β, and ν) , we extract them from the slopes of their corresponding observables (χ, m and $dU/d\beta$ respectively) in logarithmic forms plotted against $\log(L)$. In addition, as the peak of the susceptibility scaling function corresponds to the peak of the susceptibilities via the scaling variable $x_0 = L^{1/\nu}t_0$ and the critical exponent γ/ν eq. (5.17), this provides another way to calculate γ/ν from the slope of a linear plot of $\log(\chi(T_0))$ against $\log(L)$.

However, as the works in [81]-[83] present critical temperatures T_C in a unit of the 1nn exchange parameter, we then convert their T_C's into Kelvin unit by using our 'bulk exchange parameter' and show with critical exponents in table (5.1).

	Ref. [81]	Ref. [82]	Ref. [83]	Cumulant analysis	Nonlinear curve fit
T_C(K)	1178.6(6)	1177.4(7)	1177.5117(9)	$1179.8 \pm 5.5 \times 10^{-1}$	$1170.0 \pm 7.8 \times 10^{1}$
γ/ν	1.9714(4)	-	1.9620(7)	$2.010 \pm 2.9 \times 10^{-2}$	$2.050 \pm 2.3 \times 10^{-2}$
β/ν	-	-	0.5197(8)	$0.494 \pm 7.0 \times 10^{-3}$	-
ν	0.700(5)	-	0.7059(37)	$0.800 \pm 1.2 \times 10^{-1}$	$0.700 \pm 1.2 \times 10^{-1}$

Table 5.1: A comparison of results for $3D$ BCC Heisenberg magnet obtained from cumulant analysis and nonlinear curve fitting.

As can be seen, our bulk-BCC T_C's agree very well with the previous works. However, the exponent ν seems to be higher. This may be due to the fact that we perform this task by making a quick comparison to previous works in bulk limit. Then, we use only 10^5 configurations (comparing to 10^6 in [83]) for making the energy histogram. Nevertheless, at this level of testing, we decide not to go further for just improving a few digits. Also, at each simulation, we recorded 3 different sizes of histograms which have different number of bins (i.e 1000 bins, 5000 bins, and 10000 bins) and the results we get from them are not significantly different. So, to save computer memory, we use 1000 bins histogram to record the energy distribution for all our continuous-energy simulations.

One may notice that we did not use the non-linear curve fitting method to find T_C, β/ν and ν from the magnetisation scaling function. This is because the gradient of the magnetisation to the temperature is very sensitive to the statistical errors in Monte Carlo works. So, we have found that 10^5 observables for the histogram is not enough to overcome the statistical errors that prevent a useful fitting.

'Monolayer'

As we do not have 'exchange parameters' for the monolayer Fe/W(001) film, we perform simulations of the 2 layered films using only the 1nn 'exchange parameter'. Now, the system falls into the $2D$ square lattice class as the coordination number is four. The simulations we perform for this 'monolayer' use 10^5 observables for the average, discarding the first 2000 configurations to make a rough investigation of the $2D$ behaviour presented in figure (5.9). The figure shows agreement with [77] as the magnetisation magnitude is still finite for finite temperatures in finite size systems i.e. figure (5.9a). However, with increasing the film size ($L \times L$), the magnetisation curve reduces very slowly and they seem to be converging to zero for all nonzero temperatures. It may be because of the slow convergence (shown in
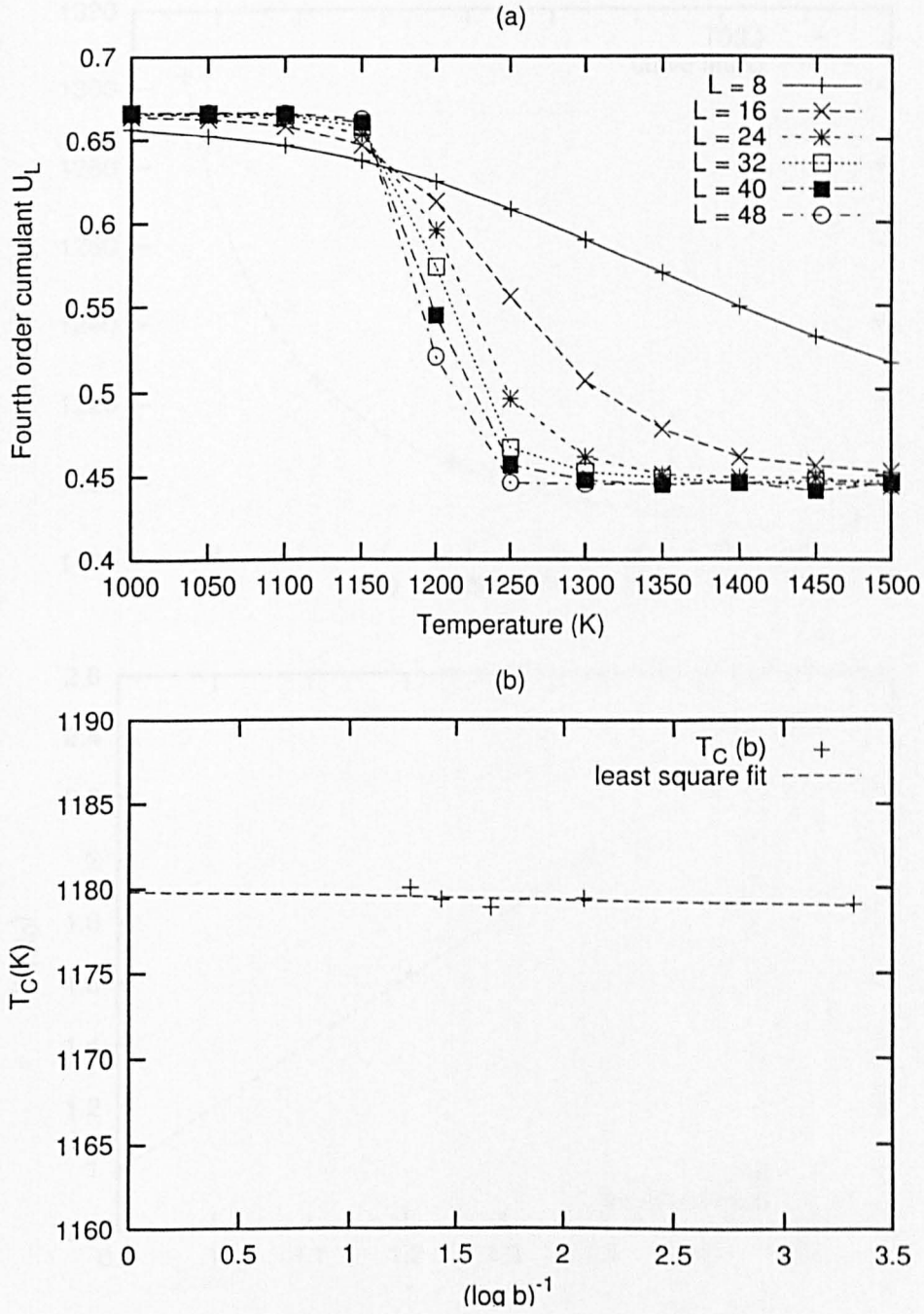
Figure 5.7: The fourth order cumulant U_L as a function of linear dimension L (a) and the extrapolation to find the critical temperature T_C (b) which gives $T_C = 1179.83 \pm 0.55$ K for 'bulk' BCC Fe. Lines are used to guide the eyes.
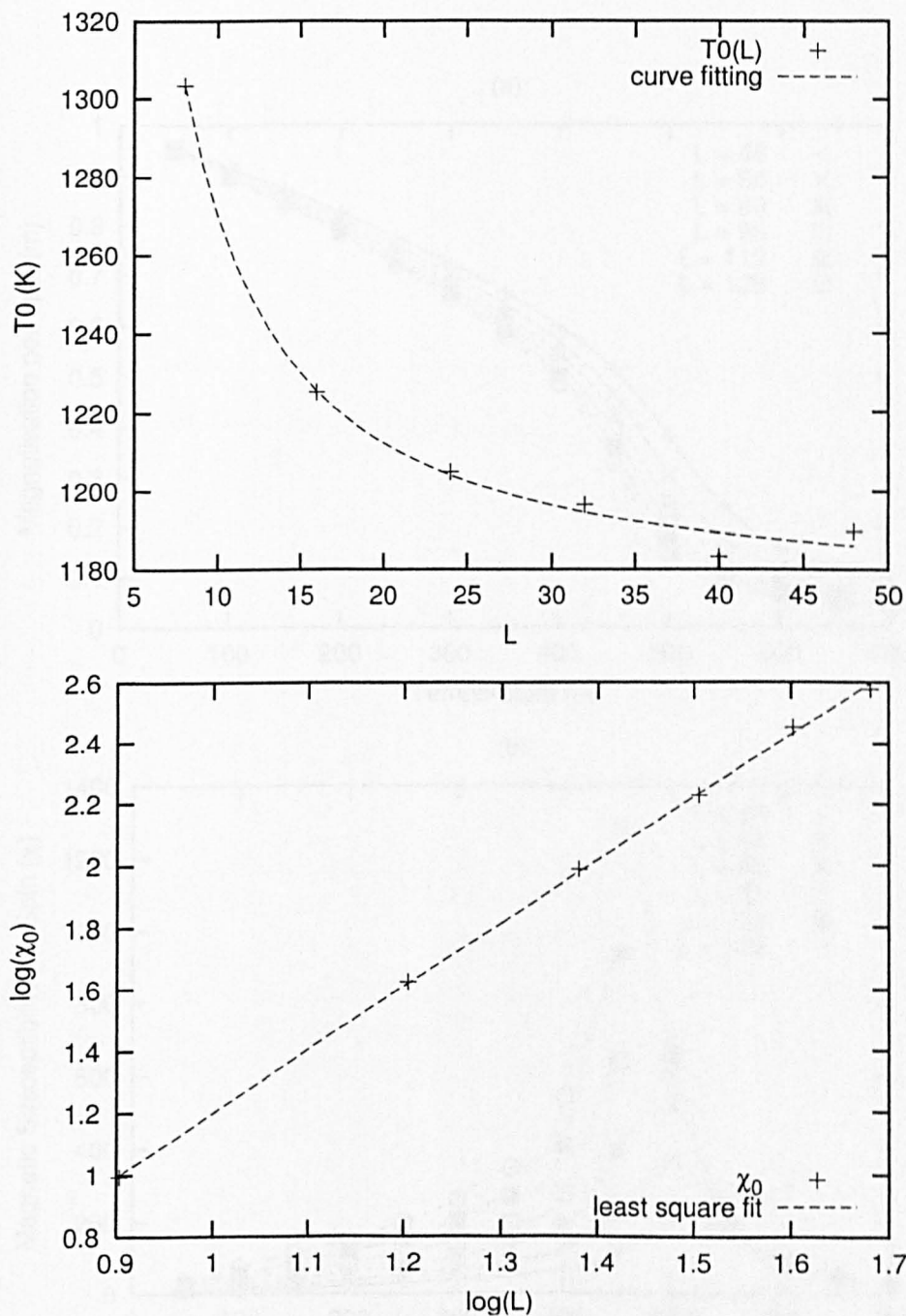
Figure 5.8: Nonlinear curve fitting for T_0 for the calculation of T_C and ν (upper) giving $T_c = 1174.3 \pm 7.7$ K and $\nu = 0.70 \pm 0.12$, and least square fit (lower) for $\log(\chi_0)$ against $\log(L)$ giving $\gamma/\nu = 2.050 \pm 0.023$ for 'bulk' BCC Fe.

(a)

(b)
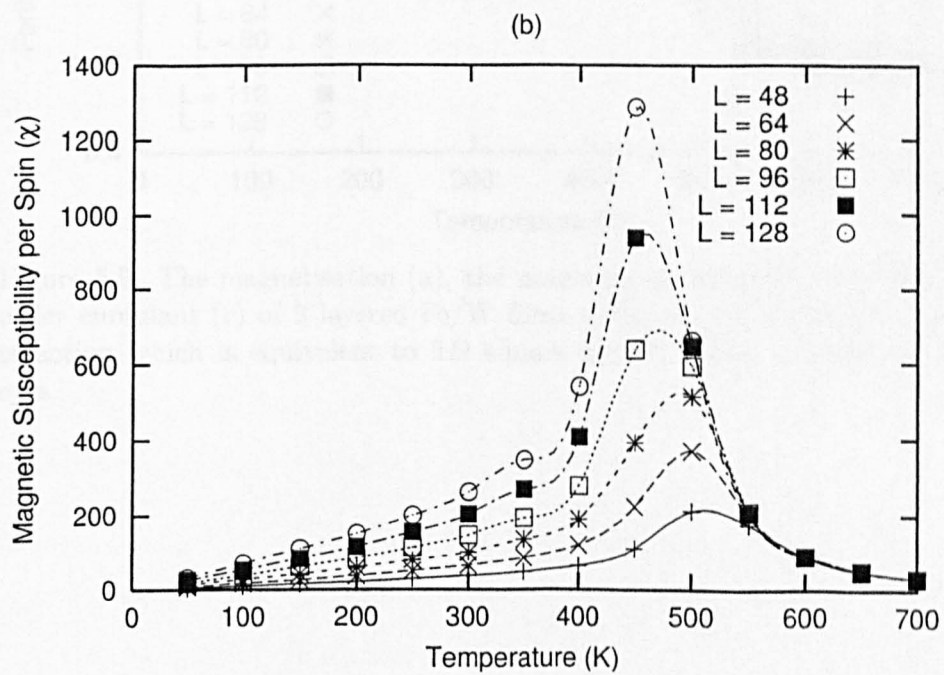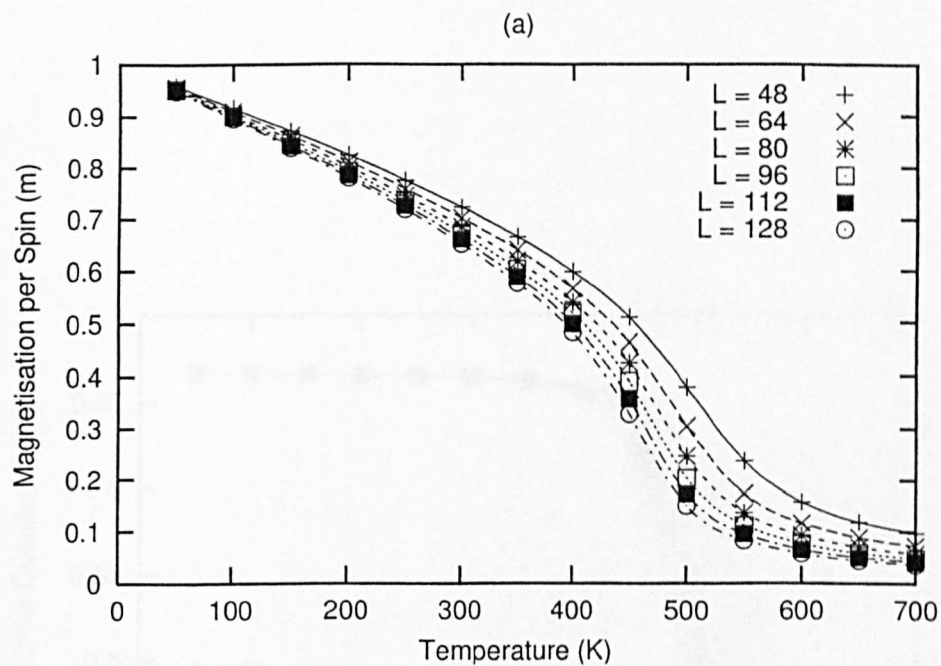
Figure 5.9: The magnetisation (a), the magnetic susceptibility (b) and the fourth order cumulant (c) of 2 layered Fe/W films using only first nearest neighbour interaction which is equivalent to $2D$ square lattice. Lines are used to guide the eyes.

figure 5.9c) that the cumulant curves do not cross except at low temperature (see figure 5.7a for a comparison). Thus, it is now not possible to use the cumulant to find critical temperature. Fortunately, from the figure (5.9b), the temperatures at the peaks of the susceptibility seem 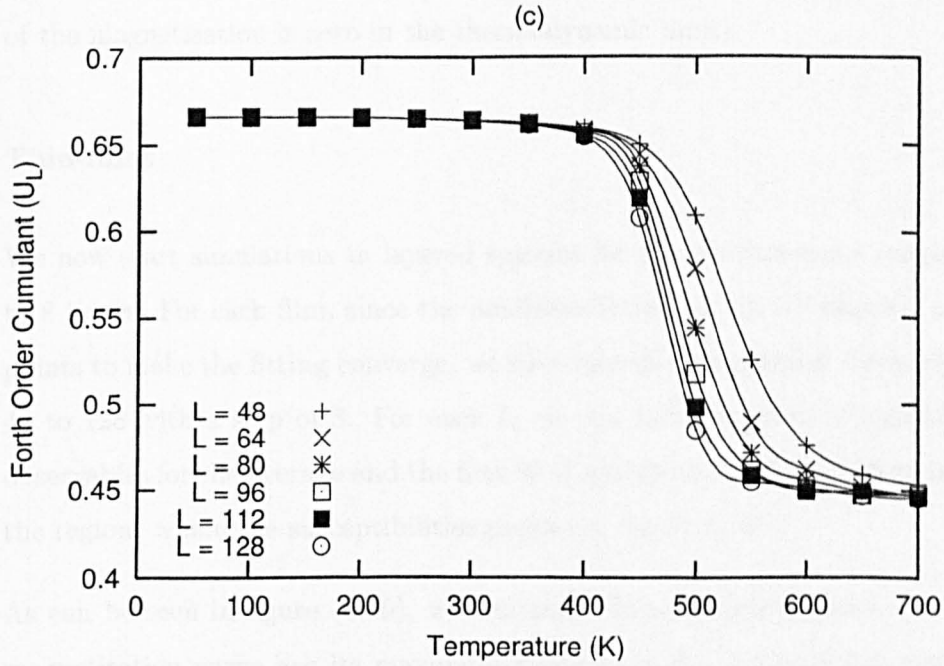to convert to nonzero value as have been predicted by high temperature series expansion (e.g. [70, 71]). So, we can use eq. (5.18) to find the critical temperature of this another kind of the phase transition (the magnetic susceptibility diverges at a finite temperature whereas the expectation of the magnetisation is zero in the thermodynamic limit).

Thin-films

We now start simulations in layered systems for film thicknesses l ranging from 2 to 8 layers. For each film, since the nonlinear fitting eq. (5.18) requires many data points to make the fitting converge, we then vary the films' linear dimension L from 48 to 128 with a step of 8. For each L, we run series of short simulations (50000 observables for the average and the first 2000 configurations being discarded) to find the regions where the susceptibilities peaks e.g. figure (5.10).

As can be seen in figure (5.10), we can notice that T_0 (temperature at which the magnetisation curve has its maximum gradient or the susceptibility gets it peak) move to higher temperature with increasing number of layers. For the cumulant curves, for all our layered systems, they give the same trends as in 'monolayer' system where there is no cumulant intersection. So, the only way we can use to find critical temperature T_C is from eq. (5.18).

For the bilayer film, we also compare the results with the 'monolayer' and we find the magnetisation curve converges faster as a result of putting 2nn in the bilayer film simulations as shown in figure (5.11).

Next, as the 'exchange parameters' vary from layer to layer, we plot the magnetisa-
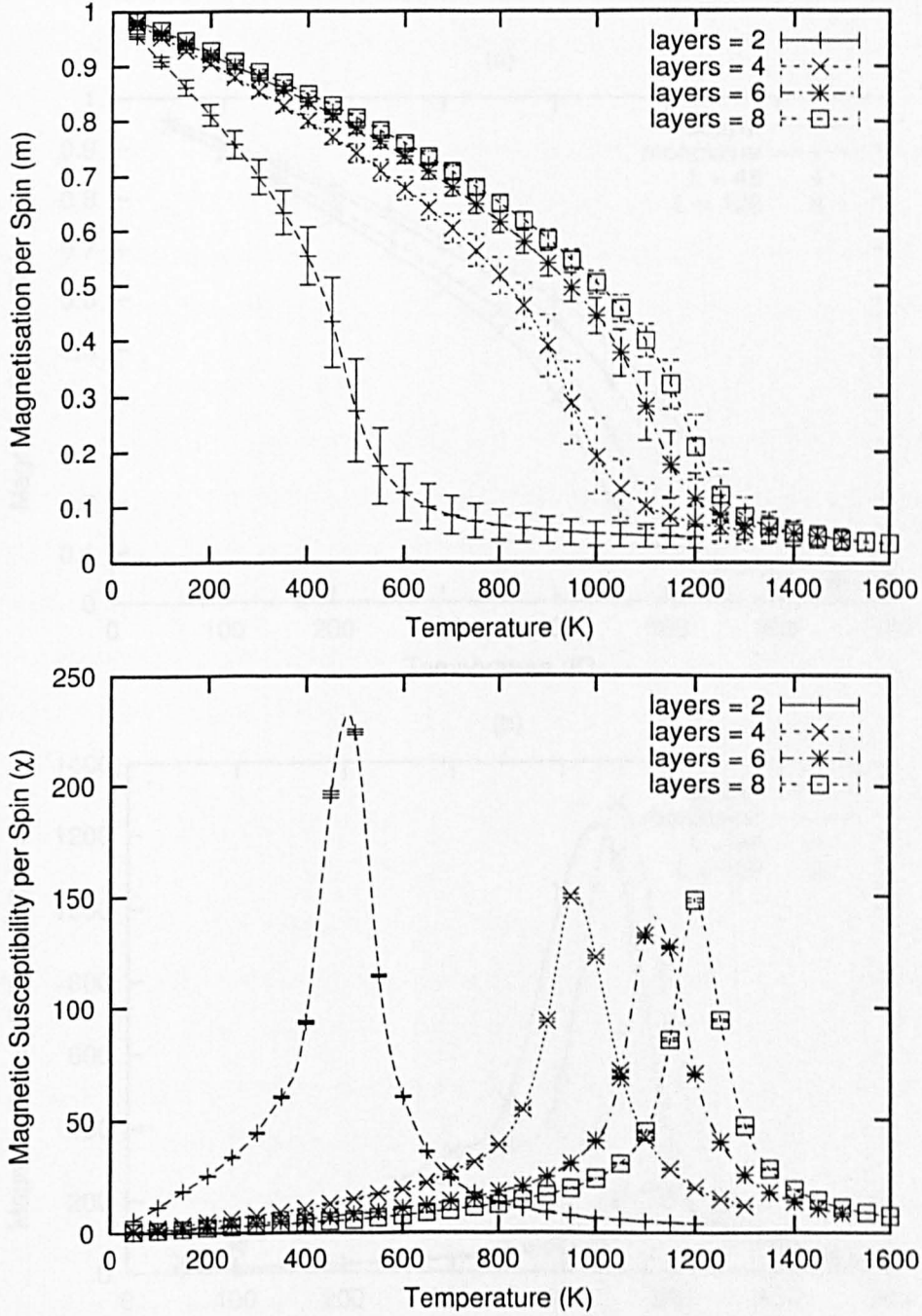
Figure 5.10: The magnetisation (a) and the susceptibility (b) as a function of temperature for $48 \times 48 \times l$ isotropic classical Heisenberg spins where l is number of layers in the film. The observable averages are taken from 50000 configurations. Lines are used only to guide the eyes.

Figure 5.11: Comparison of the magnetisation (a) and the susceptibility (b) between bilayer and 'monolayer' films for $L = 48$ and 128. Lines are used to guide the eyes.

tion and the susceptibility of each layer of the thin-films as a function of temperature to investigate how the 'exchange parameters' affect each layer in detail e.g. the bilayer film in figure (5.12) and 8 layers film in figure (5.13). For the bilayer film, figure (5.12), the 1st and 2nd layers have similar results. This is because of the strong 1nn 'exchange parameter'. For all other films, e.g. the 8 layer films in figure (5.13), the surface layers have smaller magnetisation and susceptibility magnitude than layers in the bulk as the 'exchange parameters' at the surfaces are smaller than those inside.

Now, as we have already marked the critical region for each system, we then run a reasonably long simulation measuring 10^5 observables for the histogram to extend the results and find more accurate temperatures of the peaks of the susceptibility. We analyse our results in a same way as we did for 'bulk' system. For convenience, we present the critical temperatures and critical exponents together with those from anisotropic model in table (5.2).

5.3.3   Anisotropic Result

For the anisotropic systems, we follow the same procedure as for the isotropic model to find the critical temperatures and exponents. Since the anisotropic constants are very small, we have found that the magnetisation average along the easy axis (z axis) m_z is very close to zero for all temperature e.g. figure (5.14) and the standard deviation is very large. This means that m_z is randomly distributed along the z direction (between +1 and -1) which implies that there is no preferred direction because of its very small anisotropic constants. Also, when we compare the magnetisation and the susceptibility results of both isotropic and anisotropic model, we have found that the results are not significantly different e.g. figure (5.15). The critical temperature T_C and critical exponents $(\gamma/\nu)' \equiv \gamma/\nu + 2 - d$ are presented for both isotropic and anisotropic models together with T_C from the mean-field calculation in table (5.2)
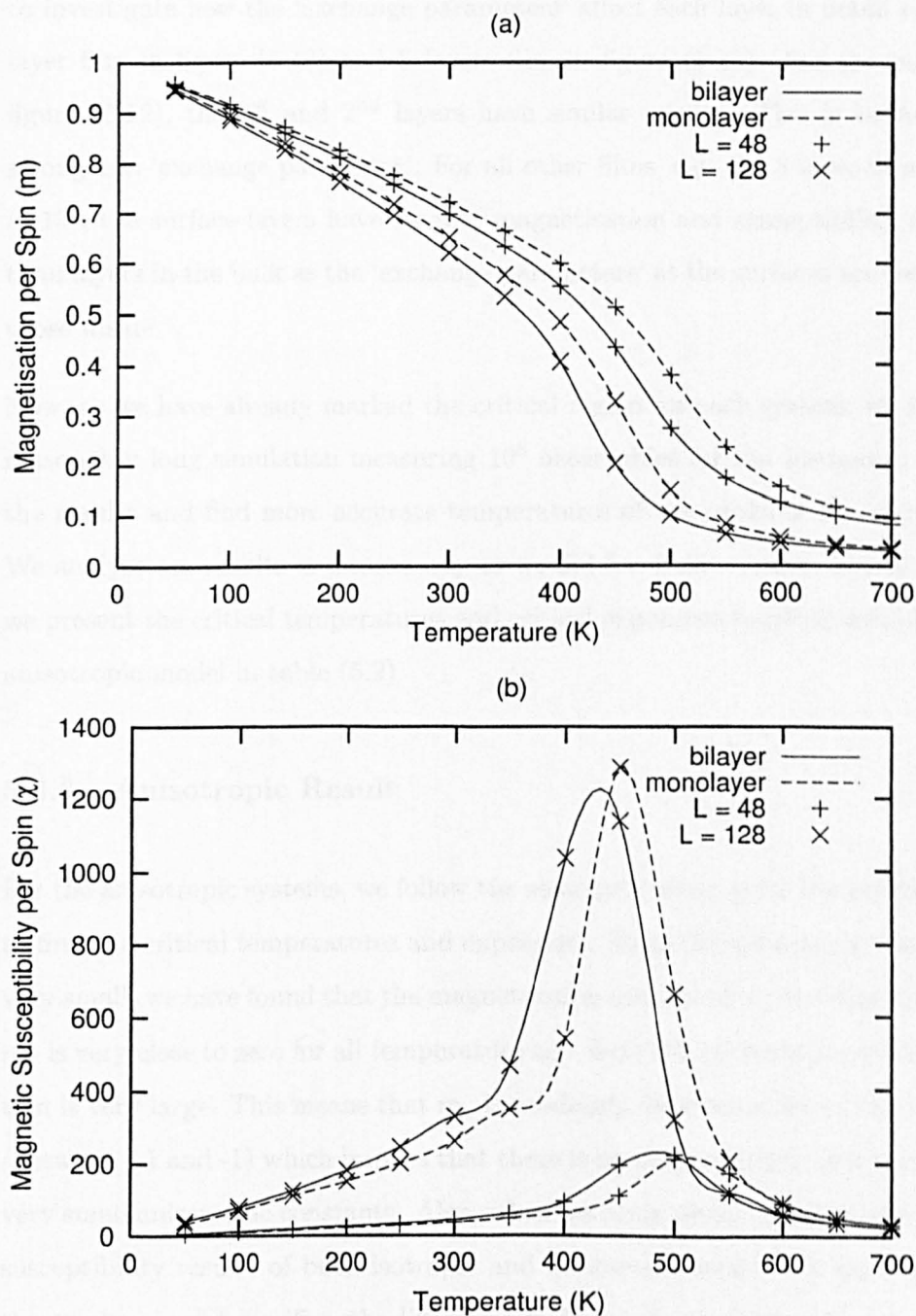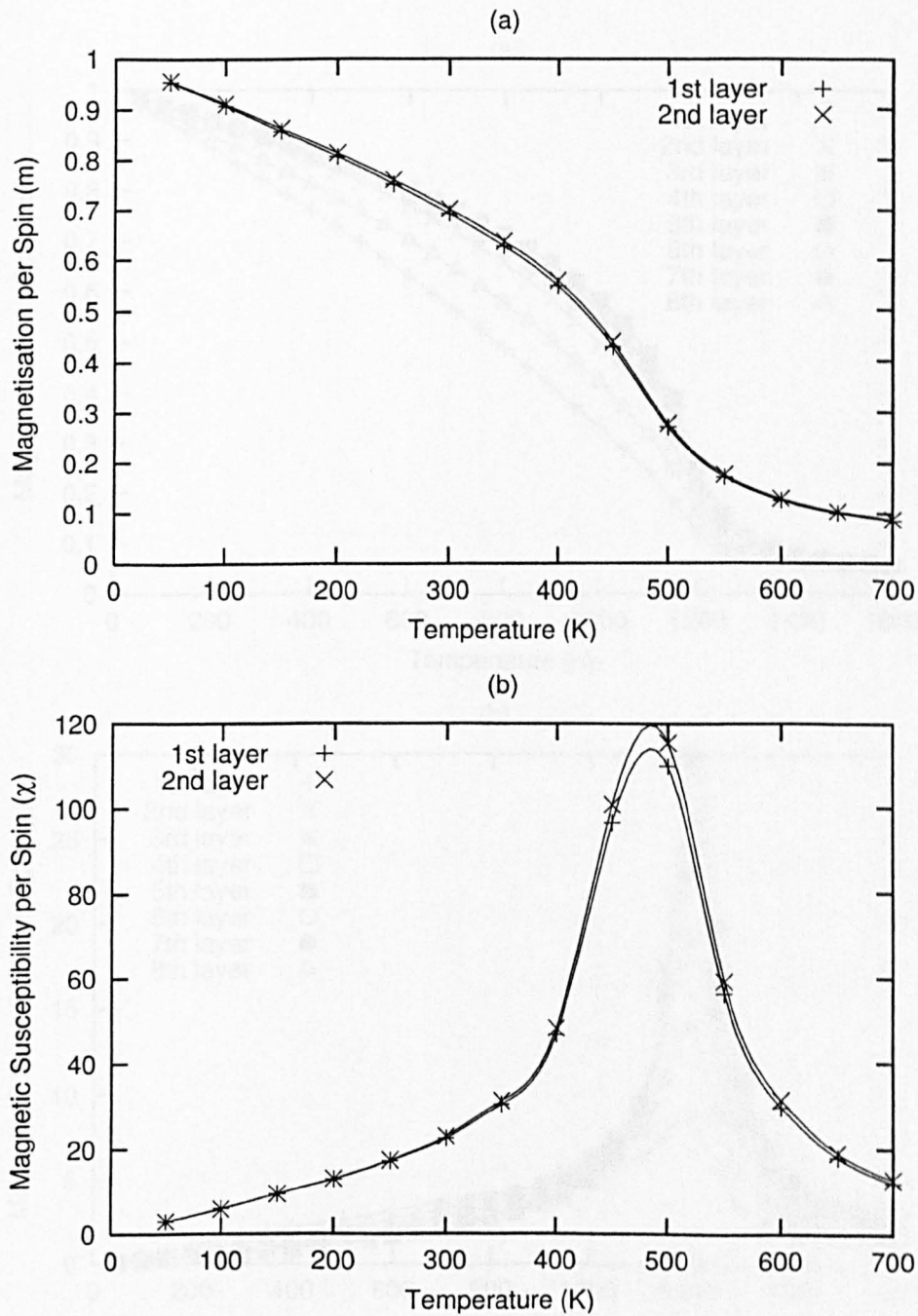
Figure 5.12: The magnetisation (a) and the susceptibility (b) as a function of temperature (K) in each layer for $48 \times 48 \times 2$ Fe/W (001) films. Lines are used to guide the eyes.

(a)

(b)
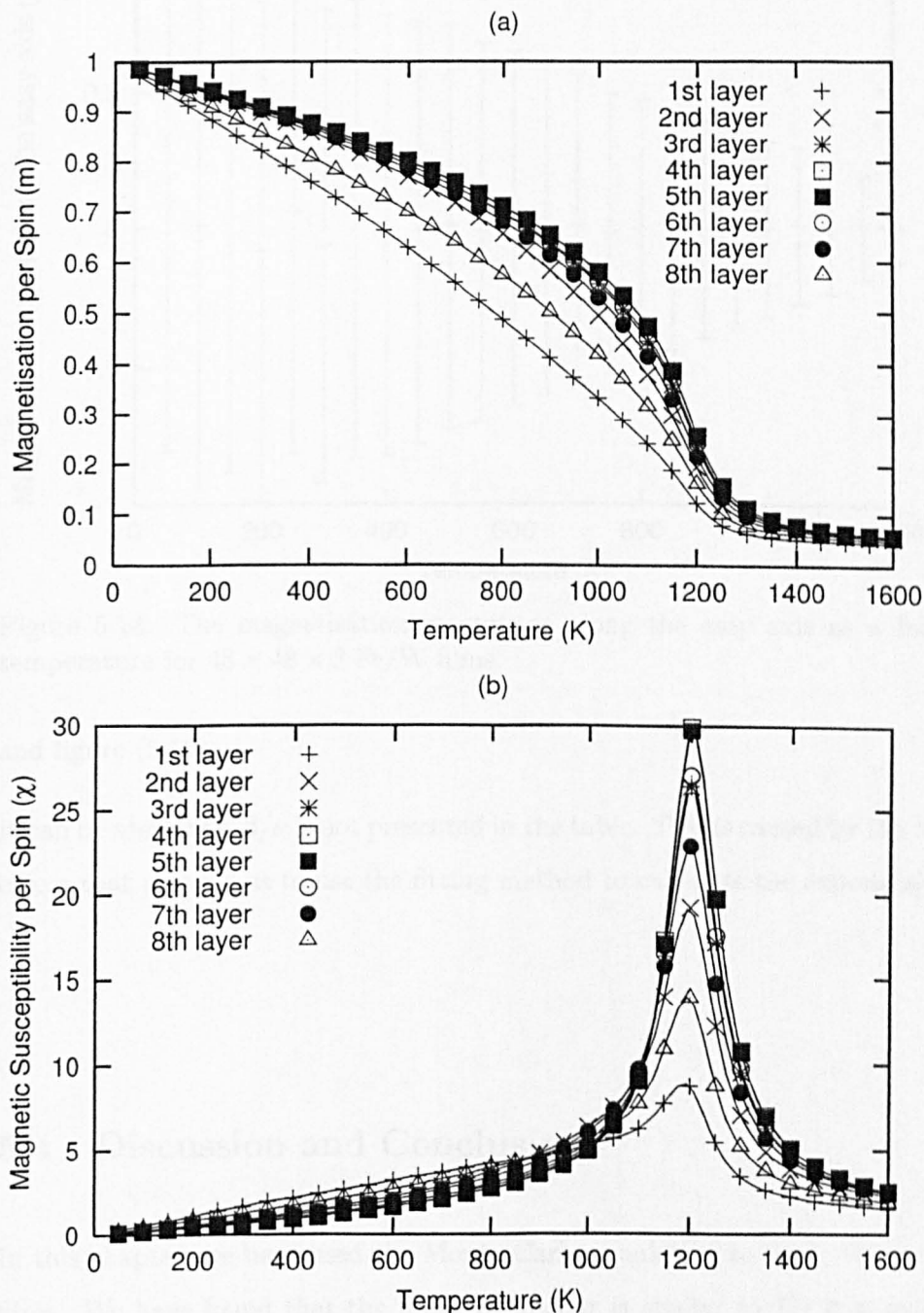
Figure 5.13: Same as figure (5.12) but for 8 layered films.
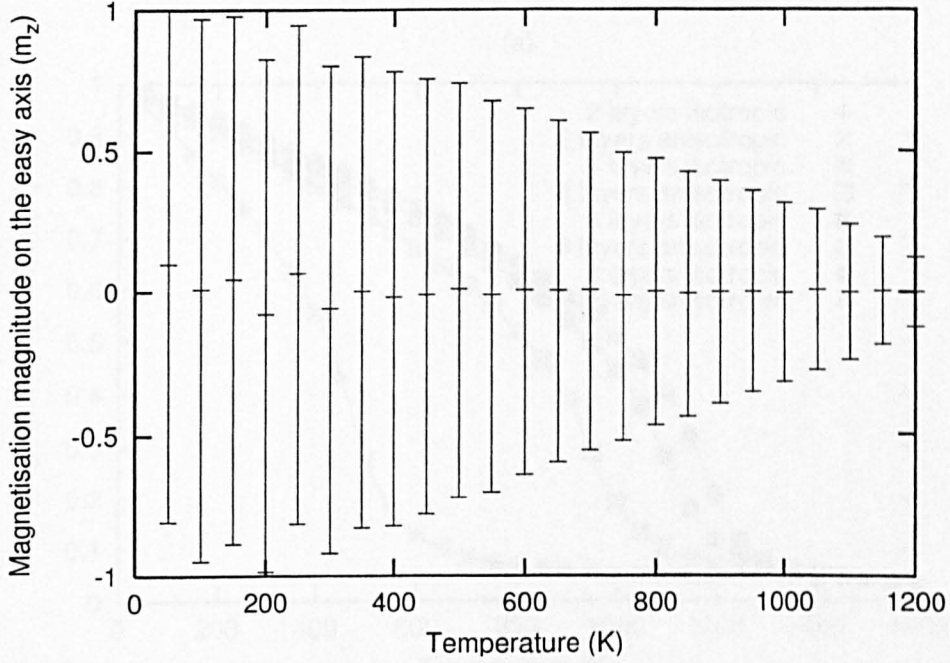
Figure 5.14: The magnetisation magnitude along the easy axis as a function of temperature for $48 \times 48 \times 8$ Fe/W films.

and figure (5.16).

It can be seen that, β/ν is not presented in the table. This is caused by the statistical errors that prevent us to use the fitting method to calculate the exponents.

5.4 Discussion and Conclusion

In this chapter, we have used the Monte Carlo simulation to study the Fe/W(001) films. We have found that the films' behaviour is similar to $2D$ system in a way that the order parameter still exist in finite system and converges very slowly when increasing the system size. This prevent us to using the cumulant analysis to find

Figure 5.15: Comparison of the magnetisation (a) and the susceptibility (b) as a function of temperature (K) in each layer between isotropic and anisotropic model for $L = 48$ Fe/W(001) films. Lines are used to guide the eyes.

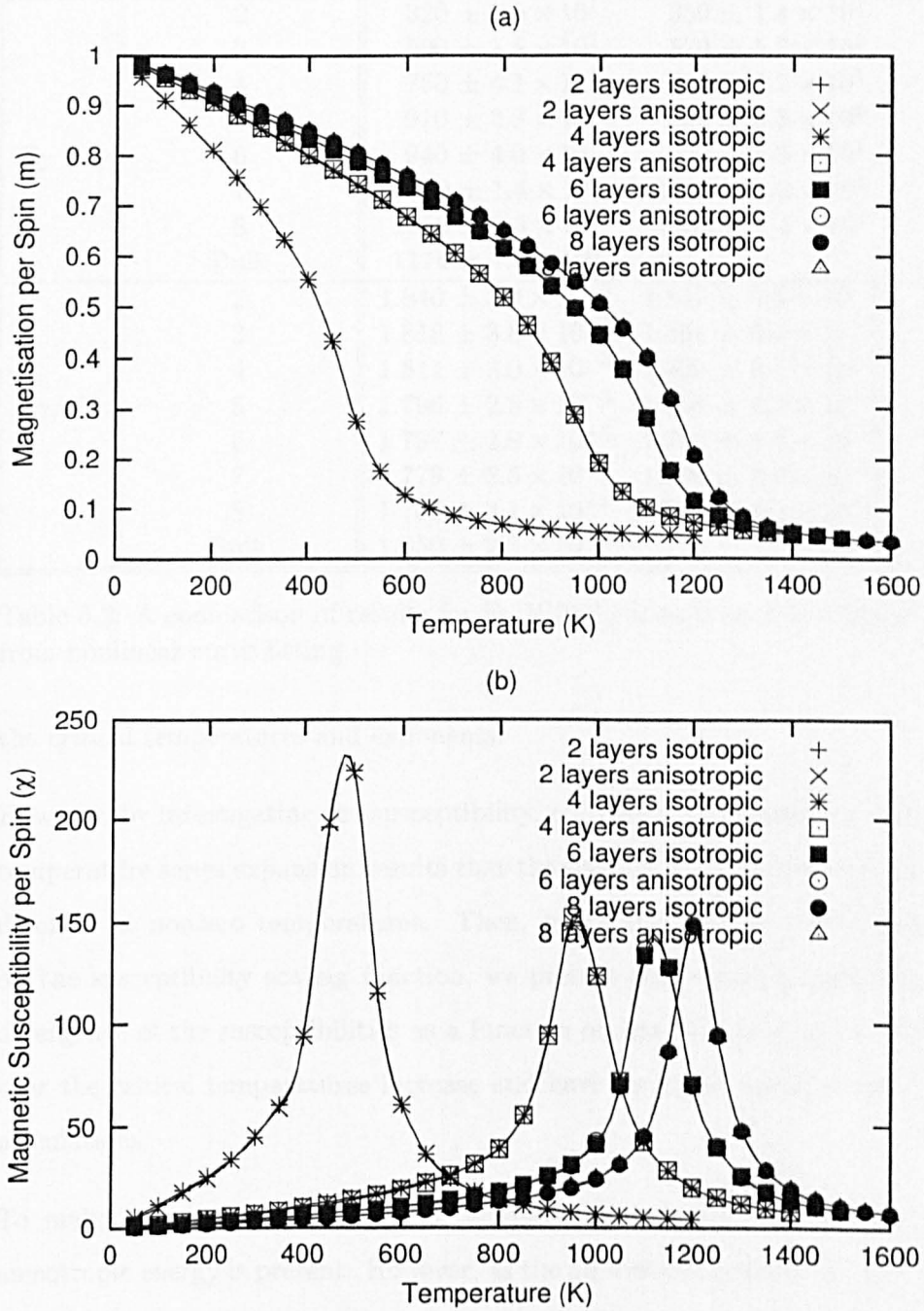|	number of layers	Isotropic	Anisotropic	Meanfield
T_C (K)	2	$320 \pm 1.9 \times 10^1$	$350 \pm 1.4 \times 10^1$	969
	3	$500 \pm 1.5 \times 10^2$	$570 \pm 5.2 \times 10^1$	1363
	4	$750 \pm 4.1 \times 10^1$	$710 \pm 7.7 \times 10^1$	1484
	5	$910 \pm 2.3 \times 10^1$	$830 \pm 6.3 \times 10^1$	1551
	6	$940 \pm 4.0 \times 10^1$	$970 \pm 1.6 \times 10^1$	1595
	7	$1030 \pm 1.4 \times 10^1$	$1030 \pm 1.3 \times 10^1$	1603
	8	$1080 \pm 1.3 \times 10^1$	$1080 \pm 1.4 \times 10^1$	1642
	Bulk	$1174 \pm 7.8 \times 10^0$	-	1687
$(\gamma/\nu)'$	2	$1.840 \pm 3.9 \times 10^{-2}$	$1.847 \pm 3.8 \times 10^{-3}$	-
	3	$1.818 \pm 3.8 \times 10^{-3}$	$1.864 \pm 5.6 \times 10^{-3}$	-
	4	$1.811 \pm 3.0 \times 10^{-3}$	$1.829 \pm 3.7 \times 10^{-3}$	-
	5	$1.796 \pm 2.8 \times 10^{-3}$	$1.808 \pm 4.2 \times 10^{-3}$	-
	6	$1.797 \pm 2.9 \times 10^{-3}$	$1.789 \pm 4.2 \times 10^{-3}$	-
	7	$1.779 \pm 2.5 \times 10^{-3}$	$1.796 \pm 3.8 \times 10^{-3}$	-
	8	$1.780 \pm 3.1 \times 10^{-3}$	$1.782 \pm 4.0 \times 10^{-3}$	-
	Bulk	$1.050 \pm 2.3 \times 10^{-2}$	-	-

Table 5.2: A comparison of results for Fe/W(001) films from 2 to 8 layers obtained from nonlinear curve fitting.

the critical temperatures and exponents.

However, by investigating the susceptibility, our results are consistent with the high temperature series expansion results that the susceptibility at thermodynamic limit diverges at nonzero temperatures. Then, by using nonlinear curve fitting based on the susceptibility scaling function, we present the critical temperatures of the divergence of the susceptibilities as a function of film thickness and we have found that the critical temperatures increase and have the same trend as the mean-field calculations.

To make our study more realistic, we have also studied the systems in which anisotropic energy is present. However, as the anisotropic constant is very small, we have found that it does not have any profound effects on the isotropic systems. Our method has been tested at the $2D$ and $3D$ limit, we have found that our results agree with previous works. To compare with experimental value, it was claimed in [79]
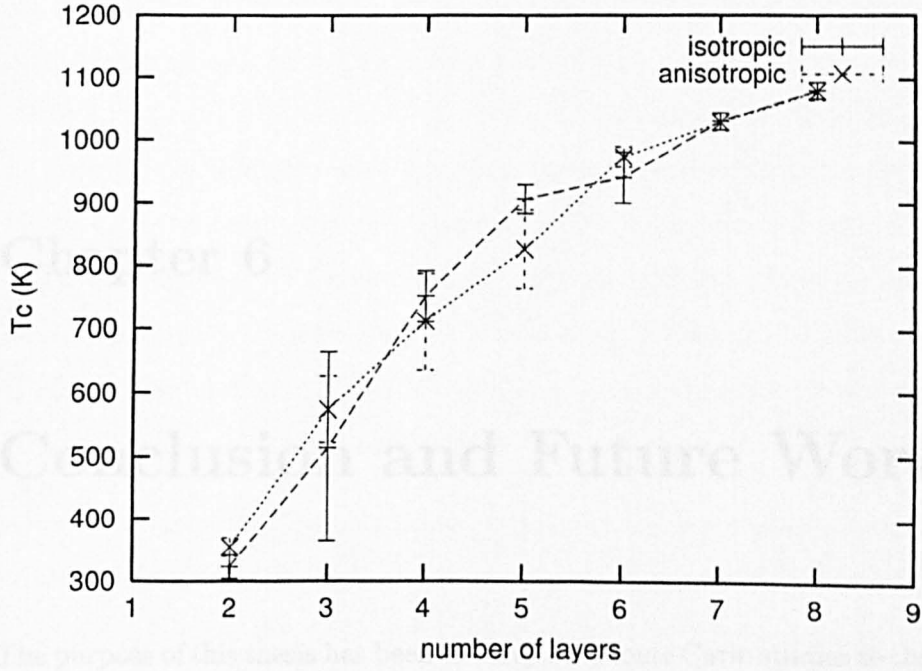
Figure 5.16: Comparison of the critical temperature $T_C(l)$'s as a function of thicknesses l between isotropic and anisotropic model for Fe/W (001) films. Lines are used to guide the eyes. With increasing number of layer, we notice T_C is moving towards bulk value $T_C^{bulk} \approx 1180$ K.

that, for bilayer film, $T_C \sim 320K$. Also, in [84], it was found that $120 \le T_C \le 350$ K for $1.4 \le l \le 2.5$ ML, and $T_C = 220 \pm 5$ K for bilayer film. This shows that our results are in level of agreement with experimental values. Thus, our simulation methods have therefore been shown to be successful in modelling magnetic critical phenomena of thin-films.

97

Chapter 6

Conclusion and Future Works

The purpose of this thesis has been to carry out Monte Carlo studies to the statistical physics problem that is provided by metallic magnetic thin-films. This problem has both technological and fundamental importance. Our studies are based on using Markov processes to cause the magnetic systems to reach equilibrium states which enable us to observe the interesting static critical behaviour where time is used to label the magnetic configurations. After that, the finite size scaling method is taken into account for the analysis to extract the magnetic critical temperatures and exponents.

Our studies began with the derivation of formulae for the magnetic susceptibility in anisotropic shaped structures (thin-films) and we investigated how both the susceptibility and the magnetisation scale with the linear size of the films L. The critical temperatures and exponents can be extracted via scaling functions and the well-known fourth order cumulant method. The derivation was based on an assumption that a single correlation length is required for the study of magnetic critical phenomena in thin-films, and we performed Ising thin-film simulations using cluster flipping algorithm (Wolff algorithm) to test this assumption and found it to be valid. Thus,

98

we were able to extract the critical exponents for the Ising thin-films. Since, the dimension d of each thin-film is unknown, we have presented the critical exponent of the susceptibility in terms of $\gamma/\nu + 2 - d$. To extract the dimension out of this, we note that some more sophisticated methods are needed (e.g. the renormalisation Monte Carlo method [13]). We also found the development of the critical temperatures and exponents as a function of thickness from the $2D$ to the $3D$ limit. For example, the smooth increasing of T_C and slow decreasing of β/ν and $(\gamma/\nu)'$ from $2D$ to $3D$ results. Our $2D$ and $3D$ results agree respectively very well with $2D$ Ising exact solutions and previous $3D$ Monte Carlo works.

Next, we applied our Method Carlo methods to more realistic models. In order to model Fe films on W(001) substrates we use 'exchange interactions' and anisotropic constants extracted from the 'first principle' electronic structure calculations. These were used to set up an anisotropic classical Heisenberg Model which we studied using Monte Carlo simulations. We also performed simulations for an isotropic model for comparison.

For our Heisenberg model simulations, we tested various algorithms in terms of their correlation times, c.p.u. time used to successfully update spins, and their reliability. As a result, we found the Wolff algorithm to be the most useful to study both the isotropic and anisotropic models. We again found our $3D$ results to agree with previous works, and the magnetisation in $2D$ systems vanishes with increasing $L \times L$ size in agreement with Mermin and Wagner's theorem that the magnetisation is absent at finite temperatures in the thermodynamic limit. On the other hand, we found the divergence of magnetic susceptibilities at finite temperatures as predicted by high temperature series expansions. For thin-films, we found that their behaviours are influenced by a $2D$ character which brings a slow convergence to the magnetisation magnitude. This is due to spinwaves with wavelengths longer than the biggest size of the thin-film system for which we performed our simulations $L = 128$. Because

99

of this, the fourth order cumulant failed and left us with only the nonlinear curve fitting method (based on the scaling functions) which required data with very high accuracy. However, we were still able to calculate the critical temperature at which the susceptibility diverges and the 'susceptibility critical exponent'. We again found a development of the magnetic critical behaviour from $2D$ to $3D$ limits. Also, for the critical temperatures, we compared our results with the mean-field critical temperatures which are usually significantly higher than experimental value for thin-films and we found that our results agree well with experiment (where available). We found that including small anisotropic constants in comparison to the 'exchange interactions' gave little change to the results.

To summarise, we have used Monte Carlo methods and finite size scaling techniques to study metallic magnetic thin-films in the critical region. We have shown how their properties change from being $2D$ to $3D$-like and we have tested the appropriateness of using Monte Carlo methods to model metallic magnetic thin-films. We look forward to our approach being used to make realistic studies of other systems. There are some possibilities to extend and improve our Monte Carlo models. For example, the long-ranged dipolar interactions could be included into the studies to investigate spin-reorientation transitions. Perhaps, renormalisation Monte Carlo methods could be used to examine the possibilities of extracting the dimension d of the thin-films. On a separate subject, these same Monte Carlo techniques could be adapted to model compositional effects in alloy films.

Bibliography

[1] P. Boyle, M. Broadie, and P. Glasserman, J. Econ. Dynam. Control **21**, 1267 (1997)

[2] B. Eftekhari, C.S. Pedersen, and S.E. Satchell, Europ. J. Finance **6**, 18 (2000)

[3] A. Chen, H. Yang, and H.K. Lo, Transp. Res.: Part B: Methodological **36**, 225 (2002)

[4] A.J. Cresswell, J.D. Allyson, and D.C.W. Sanderson, J. Environ. Radioact. **53**, 399 (2001)

[5] T. Ohta and H. Yamada, Vac. **51**, 479 (1998)

[6] L.M. Falicov, D.T. Pierce, S.D. Bader, R. Gronsky, K.B. Hathaway, H.J. Hopster, D.N. Lambeth, S.S.P. Parkin, G. Prinz, M. Salamon, I.K. Schuller, and R.H. Victora, J. Mater. Res. **5**, 1299 (1990)

[7] M.T. Johnson, P.J.H. Bloemen, F.J.A. den Broeder, and J.J. de Vries, Rep. Prog. Phys. **59**, 1409 (1996)

[8] J.W. Gibbs, *Elementary Principles in Statistical Mechanics.* (1902 Reprinted 1981) (Ox Bow Press, Woodridge, 1981)

[9] E. Ising, Z. Phys. **31**, 253 (1925)

[10] L. Onsager, Phys. Rev. **65**, 117 (1944)

[11] N. Metropolis, A.W. Rosenbluth, M.N. Rosenbluth, A.H Teller and E. Teller, J. Chem. Phys. **21**, 1087 (1953)

[12] U. Wolff, Phys. Rev. Lett. **62**, 361 (1989)

[13] M.E.J. Newman and G.T. Barkema, *Monte Carlo Methods in Statistical Physics* (Oxford University Press, Oxford, 1999)

[14] B. Efron, SIAM Rev. **21**, 460 (1979)

[15] H. Müller-Krumbhaar and K. Binder, J. Stat. Phys. **8**, 1 (1973)

[16] A.M. Ferrenberg and D.P. Landau, Phys. Rev. B **44**, 5081 (1991)

[17] A.M. Ferrenberg and R.H. Swendsen, Phys. Rev. Lett. **61**, 2635 (1988)

[18] M.E.J. Newman and R.G. Palmer, J. Stat. Phys. **97**, 1011 (1999)

[19] M.E. Fisher, Rev. Mod. Phys. **46**, 597 (1974)

[20] H.E. Stanley, *Introduction to Phase Transitions and Critical Phenomena* (Oxford University Press, New York, 1971)

[21] J.J. Binney, N.J. Dowrick, A.J. Fisher and M.E.J. Newman, *The Theory of Critical Phenomena : An Introduction to The Renormalization Group* (Oxford University Press, Oxford, 1992)

[22] M.E. Fisher, in: *Critical phenomena, Proc. Int. School of Physics, "Enrico Fermi"*, Varenna, Italy, Course LI, ed. M.S. Green (Academic Press, New York, 1971)

[23] V. Privman, in: *Finite size scaling and Numerical Simulation of Statistical Systems*, ed. V. Privman (1990 Reprinted 1998) (World Scientific, Singapore, 1998)

[24] K. Binder, Z. Phys. B **43**, 119 (1981)

[25] B.D. Josephson, Proc. Phys. Soc. **92**, 269 , 276 (1967)

[26] M.E. Fisher, Phys. Rev. **180**, 594 (1969)

[27] K. Binder and J.S. Wang, J. Stat. Phys. **55**, 87 (1989).

[28] L.P. Kadanoff, Phys. **2**, 263 (1966)

[29] K. Binder, in: *Finite size scaling and numbercal simulation of statistical systems*, ed. V. Privman (World Scientific, Singapore, 1990)

[30] S. Oualline, *Practical C programming* (O'Reilly and Associates, Cambridge, 1997)

[31] A.M. Ferrenberg, D.P. Landau, and Y.J. Wong, Phys. Rev. Lett. **69**, 3382 (1992)

[32] P. L'Ecuyer, in: *Handbook of Simulation*, ed. J. Banks (Wiley, 1998)

[33] K. Entacher. *A collection of selected pseudorandom number generators with linear structures*. Technical report, Dept. of Mathematics University of Salzburg, 1997.

[34] P.D. Coddington, Int. J. Mod. Phys. C **5**, 547 (1994)

[35] M.N. Barber, in: *Phase Transitions and Critical Phenomena* vol. 8, ed. C. Domb and J.L. Lebowitz (Academic Press Limited, London, 1973)

[36] J. Hubbard, Phys. Rev. B **20**, 4584 (1979)

[37] H. Hasegawa, J. Phys. Soc. Janpan **46**, 1504 (1979)

[38] D.M. Edwards, J. Phys. F **12**, 1789 (1982)

[39] B.L. Gyorffy, A.J. Pindor, J. Staunton, G.M. Stocks, and H. Winter, J. Phys. F **15**, 1337 (1985)

[40] J. Staunton, B.L. Gyorffy, G.M. Stocks, and J. Wadsworth, J. Phys. F **16**, 1761 (1986)

[41] W. Heisenberg, Z. Phys. **49**, 619 (1928)

[42] N.D. Mermin and H. Wagner, Phys. Rev. Lett. **17**, 1133 (1966)

[43] W. Dürr, M. Taborelli, O. Paul, R. Germar, W. Gudat, D. Pescia, and M. Landolt, Phys. Rev. Lett. **62**, 206 (1989)

[44] C.A. Ballentine, R.L. Fink, J. Araya-Pochet, and J.L. Erskine Phys. Rev. B **41**, 2631 (1990)

[45] L. Szunyogh, B. Újfalussy, and P. Weinberger, Phys. Rev. B **51**, 9552 (1995)

[46] P. Weinberger and L. Szunyogh, Comp. Mat. Sci. **17**, 414 (2000)

[47] L.H. Thomas, Proc. Camb. Phil. Soc. **23**, 524 (1927)

[48] E. Fermi, Rend. Acad. Naz. Lincei **6**, 602 (1927)

[49] P. Hohenberg and W. Kohn, Phys. Rev. B **136**, 864 (1964)

[50] W. Kohn and L.J. Sham, Phys. Rev. A **140**, 1133 (1965)

[51] U. von Barth and L. Hedin, J. Phys. C **5**, 1629 (1972)

[52] O. Gunnarsson, in *Electrons in Disordered Metals and at Metallic Surfaces*, ed. P. Phariseau, B.L. Gyorffy and L. Schiene (Plenum Press, New York, 1979)

[53] W. Kohn W. and P. Vashishta, in *Theory of the Inhomogeneous Electron Gas*, ed. S. Lundqvist and N.H. March (Plenum Press, New York, 1982)

[54] N.D. Mermin, Phys. Rev. A **137**, 1441 (1965)

[55] J. Kübler, *Theory of Itinerant Electron Magnetism* (Oxford, New York, 2000)

[56] R.P. Feynman, Phys. Rev. **97**, 660 (1955)

[57] W. Kohn and N. Rostoker, Phys. Rev. **94**, 1111 (1954)

[58] J.S. Faulkner and G.M. Stocks, Phys. Rev. B **21**, 3222 (1980)

[59] L. Petit, in *Screened Real-Space Korringa-Kohn-Rostoker Description of the Magnetic Properties of Solids*, PhD Thesis, University of Sheffield (1999)

[60] B.L. Gyorffy and G. M. Stocks, in *Electron in Disordered Metals and at Mettallic Surfaces* ed. P. Pharisean, B. L. Gyorffy and L. Schiene (Plenum Press, New York, 1979)

[61] J.B. Staunton, B.L. Gyorffy, D.D. Johnson, F.J. Pinski, and G.M. Stocks, in *Alloy Phase Stability*, ed. G.M. Stocks and A.Gonis (Kluwer Academic Publishers, Netherlands, 1989)

[62] A.J. Pindor, J. Staunton, G.M. Stocks, and H. Winter, J. Phys. F **13**, 979 (1983)

[63] S.S.A. Razee, J.B. Staunton, B. Ginatempo,F.J. Pinski, and E. Bruno Phys. Rev. Lett. **82**, 5369 (1999)

[64] S.S.A. Razee, J.B. Staunton, B. Ginatempo, E. Bruno, and F.J. Pinski, Phys. Rev. B **64**, 014411 (2001)

[65] S.S.A. Razee, J.B. Staunton, L. Szunyogh, and B.L. Gyorffy, *submitted to* Phys. Rev. B

[66] H.J.F. Jansen, Phys. Rev. B **59**, 4699 (1999)

[67] P. C. Hohenberg, Phys. Rev. **158**, 383 (1967)

[68] D. Jansow and M. E. Fisher, Phys. Rev. Lett. **23**, 286 (1969)

[69] J. Fröhlich and C. Pfister, Commun. Math. Phys. **81**, 277 (1981)

[70] H. E. Stanley and T. A. Kaplan, Phys. Rev. Lett. **17**, 913 (1966)

[71] H. E. Stanley, Phys. Rev. Lett. **20**, 150 (1968)

[72] M. A. Moore, Phys. Rev. Lett. **23**, 861 (1969)

[73] P.A.M. Dirac, Proc. Roy. Soc. A **123**, 714 (1929)

[74] D. P. Landau and K. Binder, Phys. Rev. B **24**, 1391 (1981)

[75] K. Binder and D.P. Landau, Phys. Rev. B **13**, 1140 (1976)

[76] P.A. Serena, N. Graía and A. Levanyuk, Phys. Rev. B **37**, 5027 (1993)

[77] R.E. Watson, M. Blume, and G. H. Vineyard, Phys. Rev. B **2**, 684 (1970)

[78] R.L. Fink, G.A. Mulhollan, A.B. Andrews, J.L. Erskine, and G.K. Walters, J. Appl. Phys. **69**, 4986 (1991)

[79] J. Chen and J.L. Erskine, Phys. Rev. Lett. **68**, 1212 (1992)

[80] S.S.A. Razee and J.B. Staunton (*private communication*) (2002)

[81] D.S. Richie and M. E. Fisher, Phys. Rev. B **5**, 2668 (1972)

[82] S. McKenzie, C. Domb, and D.L. Hunter, J. Phys. A **15**, 3899 (1982)

[83] K. Chen, A.M. Ferrenberg, and D.P. Landau, Phys. Rev. B **48**, 3249 (1993)

[84] H.J. Elmers and J. Hauschild, Surf. Sci. **320**, 134 (1994)